DILUTE BISMUTHIDES ON INP PLATFORM: GROWTH, CHARACTERIZATION, MODELING AND APPLICATION

by

Yujun Zhong

A dissertation submitted to the Faculty of the University of Delaware in partial fulfillment of the requirements for the degree of Doctor of Philosophy in Materials Science and Engineering

Winter2014

ProQuest LLC.
789 East Eisenhower Parkway
P.O. Box 1346
Ann Arbor, MI 48106 - 1346

DILUTE BISMUTHIDES ON INP PLATFORM:

GROWTH, CHARACTERIZATION, MODELING

AND APPLICATION

by

Yujun Zhong

Approved: _____
David C. Martin, Ph.D.
Chair of the Department of Materials Science and Engineering

Approved: _____
Babatunde A. Ogunnaike, Ph.D.
Dean of the College of Engineering

Approved: _____
James G. Richards, Ph.D.
Vice Provost for Graduate and Professional Education

I certify that I have read this dissertation and that in my opinion it meets the academic and professional standard required by the University as a dissertation for the degree of Doctor of Philosophy.

Signed: _____

Joshua M. O. Zide, Ph.D.
Professor in charge of dissertation

I certify that I have read this dissertation and that in my opinion it meets the academic and professional standard required by the University as a dissertation for the degree of Doctor of Philosophy.

Signed: _____

Matthew F. Doty, Ph.D.
Member of dissertation committee

I certify that I have read this dissertation and that in my opinion it meets the academic and professional standard required by the University as a dissertation for the degree of Doctor of Philosophy.

Signed: _____

Robert L. Opila, Ph.D.
Member of dissertation committee

I certify that I have read this dissertation and that in my opinion it meets the academic and professional standard required by the University as a dissertation for the degree of Doctor of Philosophy.

Signed: _____

James Kolodzey, Ph.D.
Member of dissertation committee

ACKNOWLEDGMENTS

This is an acknowledgment that I have planned since the very beginning of my Ph.D. study. I can't find enough words to express my deepest appreciation for my advisor: Joshua Zide. I still remember what he said to me when I first joined his group "Choosing the right doctoral advisor is the second most important thing in your life; of course, the most important one is finding the right spouse☺." I believe I made both choices right. Josh is really the best advisor I can ask for. He is truly brilliant and very knowledgeable; more important, he is very genuine and really loves his job as a mentor. I learned numerous things from him and I really enjoyed my Ph.D. life in our group.

I am also very thankful for my committee members: Dr. Doty, Dr. Opila and Dr. Kolodzey, who are all excellent teachers. From them, I learned not only knowledge, but also the angle how they think.I will miss Dr. Doty's sharp comments, Dr. Opila's recondite jokes and Dr. Kolodzey's practical experiences. I also appreciate Dr. Chase's help in many optics related projects. He is an excellent researcher and a very resourceful person who can be turned for help.

I would also like to thank all my group members: Pernell, Cory, Matt, John and Laura. You guys are really the best! It's you guys who make this group so cooperative and friendly. I will definitely miss the time working with you guys and all the games we have played together.

I must thank all my dearest friends in UD. Please forgive me not to list all the names because it really will be too long. We have spent so many happy times together

and also have been through some difficulties. Thank you for sharing my happiness and sadness, always being there to support me and understand me. You are the priceless treasure in my whole life. I would also like to thank everyone in MSEG department. I really enjoyed my Ph.D. life in UD.

Lastly, I will give my deepest appreciation to my family. My Mom and Dad have raised me up and taught me to become a person who I am now. I think all of us are very happy with the result. My husband always supports me with his gentle and firm hands. I am not afraid of anything with you around.

TABLE OF CONTENTS

LIST OF TABLES

LIST OF FIGURES

ABSTRACT

Conventional III-V compounds (GaAs/ InGaAs/ InAlAs) containing a small amount of bismuth are called dilute bismuthides (a.k.a. dilute bismides). They are a relatively new class of materials and have interesting optical and electrical properties that lead to a large number of novel applications in mid-infrared(mid-IR) optoelectronics, IR transparent contact materials, photovoltaics and thermoelectrics. This dissertation focuses on the growth and characterization of dilute bismuthides with potential use in the first three applications.

Incorporating Bi into conventional III-V compounds will cause a unique phenomenon called valence band anticrossing(VBAC). The interaction between the bismuth atom and the matrix material will make the valence band split into two bands: E+ and E-; E+ is closer to the conduction band than the original valence band of the matrix material. Using this effect, we can adjust the band gap and the valence band position of dilute bismuthides by controlling the bismuth concentration.

The growth of bismuth-containing materials using molecular beam epitaxy (MBE) requires low growth temperature and strict stoichiometric III-V ratio. This dissertation will discuss in detail the optimum growth condition of InGaBiAs, the challenge of increasing the bismuth concentration, and the possible solution to produce high bismuth concentration samples. Accordingly, composition, strain and relaxation, surface morphology, optical properties and electrical properties of InGaBiAs thin films are characterized to study these materials.

The first application of InGaBiAs is mid-IR optoelectronic materials. The band gap of InGaBiAs can be tuned within the mid-IR range, and the film can be produced being lattice-matched to the InP substrate. In addition, degenerately doped InGaBiAs:Si is an ideal choice for the transparent contact material in the infrared range due to its high transmittance and conductivity in this wavelength range. We next proposed a new upconversion solar cell design with the incorporation of dilute bismuthides, which is expected to enable very high solar cell efficiency.

Finally, this dissertation discussed some future directions in this field: high bismuth concentration films, a measurement to fully understand the band structure of InGaBiAs and a proposal of temperature-insensitive application. As a conclusion, dilute bismuthides remain promising as optoelectronic materials.

Chapter 1

INP BASED OPTOELECTRONIC DEVICES, HIGHLY MISMATCHEDALLOYS, DILUTE NITRIDES AND DILUTE BISMUTHIDES, AND MOLECULAR BEAM EPITAXY TECHNIQUE

This dissertation will focus on the application of a new class of materials-dilute bismuthides. Chapter 1 will introduce some general concepts as bedrocks for the whole dissertation. It will start with an introduction of InP based optoelectronic devices in Section 1.1. Section 1.2 will explain the physics and some special properties of highly mismatched alloys (HMAs). Section 1.3 will compare two groups of HMAs with many similarities, dilute nitrides and dilute bismuthides. It will first start with the most extensively studied HMAs, dilute nitrides, and will discuss the growth and properties of dilute bismuthides next. Section 1.4 will discuss the growth technique, molecular beam epitaxy (MBE),and other tightly related techniques. Section 1.5 will provide an overview for this dissertation.

1.1 General Overview of InP Based Optoelectronic Devices

Current semiconductor industry is dominated by Si for its matured processing techniques, earth abundance and low price. However, Si has some intrinsic problems such as low electron mobility and an indirect band gap, which almost exclude it from the market of high speed integrated circuits and light emitting devices. The aforementioned markets are governed by III-V compounds due to their extremely high electron mobility and direct band gap. In addition, they possess high radiation hardness and wide operation temperature range (most of them have band gaps above

the band gap of Si, 1.1 eV, which makes them stand higher operation power and temperature than Si), making them of special interest for space and military use.

The mostly used III-V compounds are GaAs, InP, GaP, GaN, InSb, GaSb, InAs and ternary or quaternary alloys which are composed of these binary compounds. Most of them have the zinc-blend crystal structure and could be mixed at any ratio. The majority of III-V devices are either based on GaAs or InP substrates. GaAs based materials are the most extensively studied and produced III-V compounds and are considered as the most important semiconductor materials after Si. They are widely utilized in high speed digital integrated circuits due to their very high electron mobility. They have high optoelectronic conversion efficiency due to their direct band gaps, which makes them widely utilized for light emitting diodes (LED), laser diodes (LD) and lasers. AlAs has a lattice constant close to that of GaAs (a_{GaAs} is 0.56635 nm and a_{AlAs} is 0.56622 nm[1][2]), which makes it convenient to grow AlGaAs with any atomic ratio between Al and Ga and being lattice matched to the GaAs substrate. Therefore, it is straightforward to design many types of devices using GaAs/AlGaAs heterojunctions with barrier height continuously adjustable over a wide range.

InP-based materials have very similar properties as GaAs-based materials like high mobility, direct band gap and high radiation hardness, except the former has better performance in many of these aspects than the latter. InP-based materials have higher saturation velocity of electrons and higher electron mobility under high electric field than GaAs-based materials, which makes them more suitable for the active channel in high-power and high-speed electronic devices[3]. InP substrate has higher thermal conductivity than GaAs substrate, and InP-based materials have higher threshold of optical catastrophic degradation than GaAs-based materials, rendering

them as ideal materials for lasers[4]. InP based materials are first adopted for fiber optical communication systems because InGaAs/InGaAsP lattice matched to InP have wavelengths operating at 1.55 and1.3μm respectively, which are optical fiber low loss windows. InP-based electrical amplifiers offer the advantages of low power consumption, high linearity and low temperature sensitivity, which significantly improve the battery life and the signal reception[5]. In the 1980s, a variety of InP-based transistors, LEDs, lasers, and photodiodes were generated due to the fast development of optical communication technology. Accordingly, the cost of producing InP-based devices has decreased over the years, making InP more competitive for the market.

1.2 **Introduction to Highly Mismatched Alloys**

Over the past several decades, researchers have extensively studied the physics of solid solution, especially the electronic structure of them. Some well-investigated solid solutions include Si_xGe_{1-x} from Group IV, $In_xGa_{1-x}As$, $GaAs_{1-x}P_x$ from III-V and$Zn_{1-x}Cd_xS$, $Hg_{1-x}Cd_xTe$ from II-VI. One of the simplest treatments of such alloys is based on the virtual crystal approximation (VCA), which means that many properties of the new alloy can be given by the linear interpolation between the end-point binary materials[6]. Figure 1.1 shows the lattice constant of some typical III-V compounds as a function of their composition. From this figure, we can see that the lattice constant of these ternary alloys varies linearly with the atomic ratio between the two binary components.

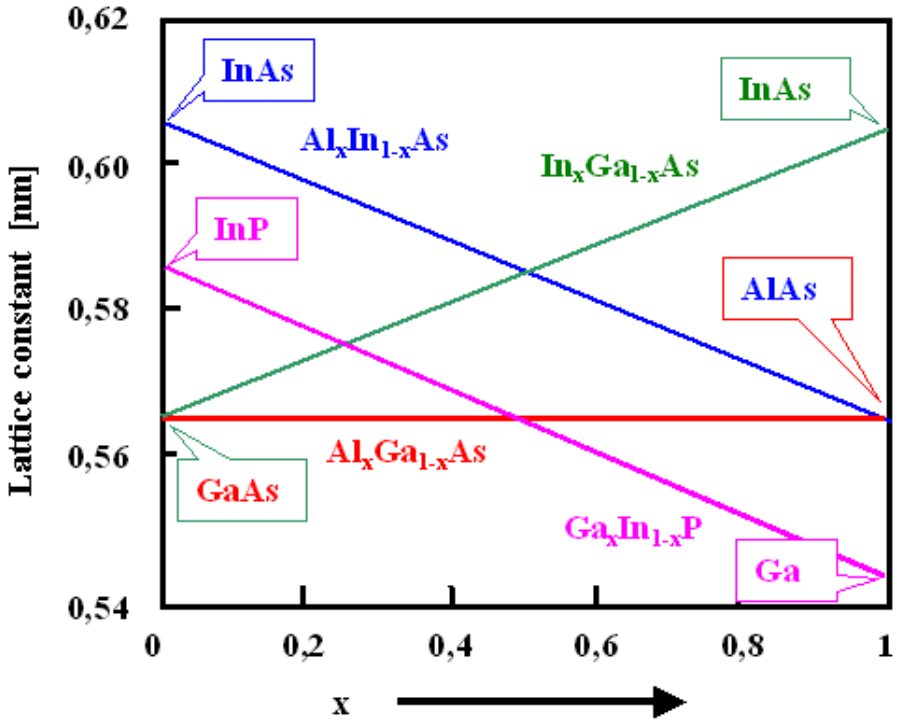

Figure 1.1 Lattice constant of III-V compounds as a function of the composition. The ternary alloys exhibit a linear dependence on the atomic ratio between two components in the alloy. (http://www.tf.uni-kiel.de/matwis/amat/semitech_en/kap_2/backbone/r2_3_1.html)

Therefore, we can predict the lattice constant a of a ternary alloy $A_xB_{1-x}C$ through the lattice constant of the two end-point materials a_{AC} and a_{BC} and the atomic ratio x between two varying elements A and B. This is named as Vegard's law and can be expressed as:

$$a=xa_{AC}+(1-x)a_{BC} \qquad \text{Equation 1.1}$$

Additionally, the band gap E_g of the ternary alloy can also be written as a function of the atomic ratio x:

$$E_g=a+bx+cx^2 \qquad \text{Equation 1.2}$$

where a, b, and c are characteristic constants for different alloys. Specifically, c is defined as bowing parameter. Therefore, researchers have plotted band gaps of alloys as a function of their lattice constants, which is given in Figure 1.2.

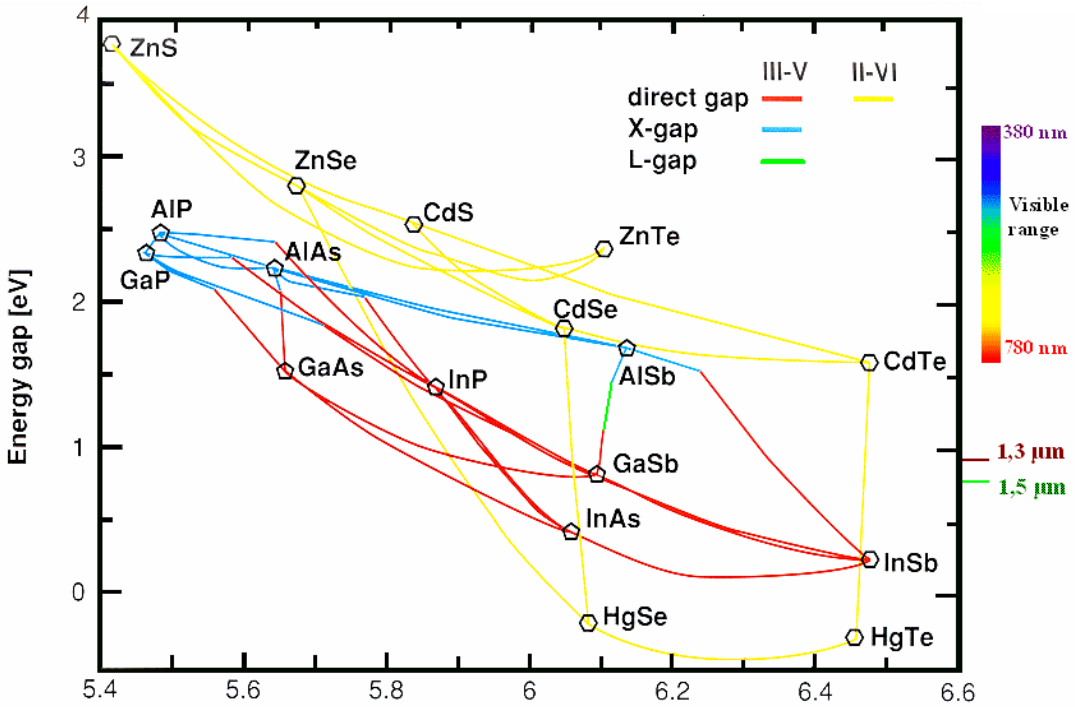

Figure 1.2 The fundamental band gaps of semiconductors as a function of lattice constant. (http://www.tf.uni-kiel.de/matwis/amat/semitech_en/kap_2/backbone/r2_3_1.html)

Recent progress in epitaxial growth techniques has led to the successful synthesis of highly mismatched alloys (HMAs), the properties of which are distinctly different from randomly disordered alloys in a way that they drastically deviate from the linear predictions of the VCA.HMAs are generated by incorporating an isovalent minority component into a matrix material, but the minority component has a large

electronegativity and atomic radius mismatch with the isovalent element in the matrix material. It is widely accepted that the minority will strongly affect the property of the matrix material because its electronegativity and atomic radius difference will result in a large potential perturbation to the Bloch states of the matrix material. The large potential perturbation is a combination effect from the atomic radius and electronegativity difference according to the relationship between the atomic separation and atomic potential as given in Figure 1.3. This will lead to a strong band restructuring due to the hybridization between the localized states of the minority component and the extended energy states of the matrix material, which includes generating peaks in the density of states (DOS) or even anticrossing near conduction band or valence band. Generally, the larger the atomic radius and electronegativity difference is, the stronger the interference is. Novel optical and electrical properties could result from this band restructuring and be applied to IR optoelectronics since it usually causes anomalous band gap narrowing. Currently, HMAs materials have been mostly studied in Group IV, III-V and II-V include $Ge_{1-x}Sn_x$[7], $Ga(In)N_{1-x}As_x$[8], [9], and $ZnTe_{1-x}Se_x$[10].

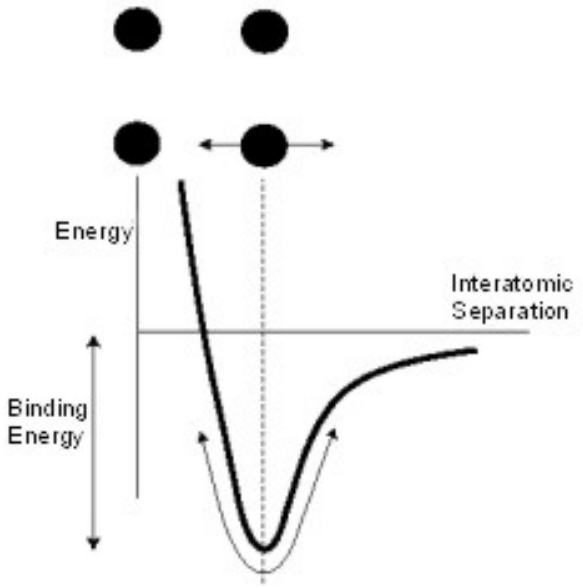

Figure 1.3 The binding energy between two atoms as a function of interatomic separation. (http://www.princeton.edu/~maelabs/mae324/glos324/potential.htm)

1.3 **Dilute Nitrides and Dilute Bismuthides**

Dilutenitrides are the most extensively studied III-V HMAs over the past decades. Normally, substitution of isovalent impurity results in a weak perturbation to the host band structure. But the element N introduces localized states to GaAs/ InGaAs, and behaves more like an isoelectronic acceptor than a true alloying element. This is because the interatomic potential resulting from the atomic radius difference between N and As combined with the high electronegativity of N can produce a localized center that attracts electrons. Table 1 compares the electronic structure, atomic radius and electronegativity of all group V elements. This resonant interaction between the N 2s orbital and the bottom of the matrix material conduction band will lead to an anomalous large band gap reduction and is called conduction band anticrossing (CBAC). Figure 1.4 shows a schematic figure of CBAC.

Table 1.1 Comparison of electronic structure, atomic radius and electronegativity (Pauling scale) of group V elements[11], [12]

Element	Electronic structure	Atomic radius	Electronegativity
N	$[He]2s^2 2p^3$	0.065	3.0
P	$[Ne]2p^6 3s^2 3p^3$	0.1	2.2
As	$[Ar]3d^{10} 4s^2 4p^3$	0.115	2.2
Sb	$[Kr]4d^{10} 5s^2 5p^3$	0.145	2.1
Bi	$[Xe]4f^{14} 5d^{10} 6s^2 6p^3$	0.160	2.02

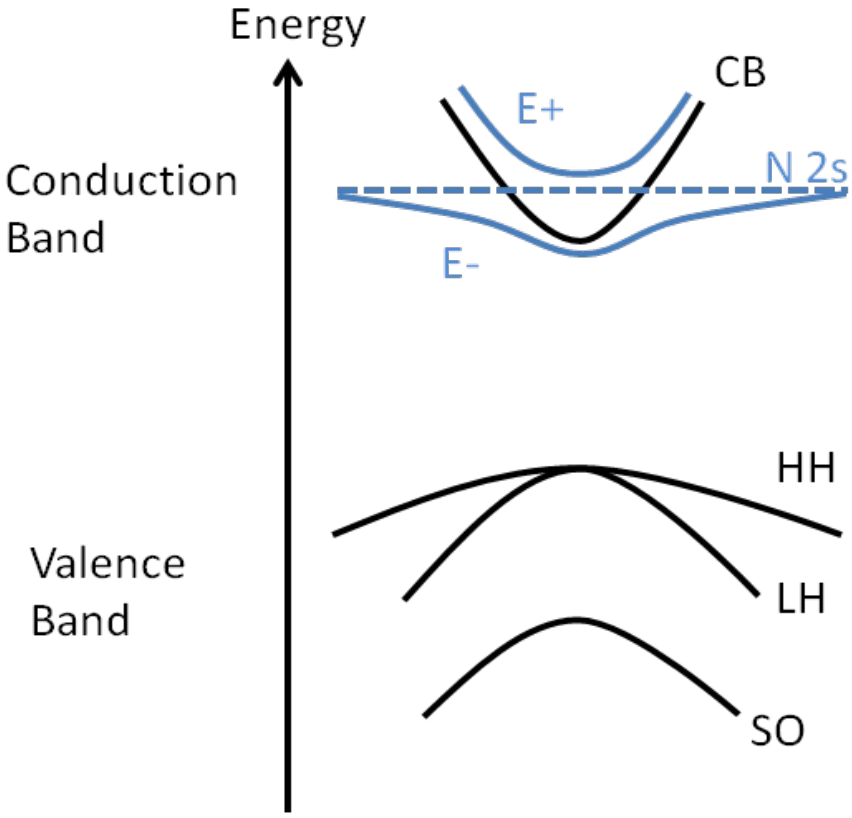

Figure 1.4 Scheme of CBAC in dilute nitrides

An experimental observation has demonstrated a band gap reduction of 180 meV with only 1% N incorporated in GaNAs [13]. As a comparison, adding In to GaAs will bring down the fundamental band gap at a rate about 12 meV/%In [14], which is 1/15 of the rate of adding nitrogen. Due to the large band gap reduction effect resulting from the CBAC of dilute nitrides, GaNAs/InGaNAs are considered as laser materials on GaAs platform operating in the telecom wavelength range between 1.3 and 1.5 μm because the state-of-art strained InGaAs on GaAs quantum well laser can only reach a long wavelength of 980 nm [15]. It has been experimentally demonstrated that Auger recombination and inter-valence band absorption (IVBA) are the two primary reasons that lead to high threshold current and high optical cavity losses at elevated temperature [16]. One effective method to suppress CHSH (Conduction band electron/ Heavy hole/ Spin-orbit split-off band/ Heavy hole) Auger and IVBA is to make the spin-orbit splitting energy Δ_{SO} exceed the fundamental band gap in these materials. However, this is very difficult to achieve in dilute nitride system with a fundamental band gap between 1.3 and 1.5 μm because the band gaps are too big. Fortunately, this is achievable in dilute bismuthides system which I will explain in detail in Section 6.1.

Dilute bismuthides are a relatively new class of HMAs. The work on the dilute GaBixAs1-x alloy was initially motivated by the search for a semiconductor with a temperature-insensitive band gap [17]. It was proposed that by combining a normal material with a negative band coefficient (band gap red shifts at elevated temperature) and an anomalous material with positive band coefficient (the opposite trend), we will be able to create a material with band gap insensitive to the ambient temperature [17]. The positive band coefficient is related to the band inversion model, and a semi-metal

(InBi) is highly likely to possess this property. InGaNBiAs alloys were proposed by Mascarenhas et. al. as a way by strain compensation to minimize the deleterious effects of N on the transport properties and recombination lifetime [18]. It is believed that if the small N atom and the large Bi atom are close enough to each other, the resulting strain and potential perturbation in the lattice would be paired as a dipole rather than a monopole. Therefore, the Bloch wave and the electron transportation will be less affected than in pure dilute nitrides. Previously, bismuth was widely used as a good surfactant to improve the crystalline quality of dilute nitrides as the surface exposed to bismuth flux appears to be very smooth and shows large areas of flatness [19]. In addition, a significant increase in the photoluminescence (PL) emission efficiency has also been observed in experiments [19]. It is believed that the surfactant will reduce the activation energy for surface diffusion, which allows the growth processes to happen at a much lower temperature. Interestingly, Tixier et al. [20] discovered that when the growth temperature is decreased below 400 ˚C and the Group III/V ratio is near stoichiometric, bismuth started to incorporate instead of serving as surfactant. Thereafter, dilute bismuthides have attracted increased scientific interests.

Dilute bismuthides are formed by incorporating a small amount of bismuth into III-V alloys such as GaAs and InGaAs. The incorporation of bismuth will lead to valence band anticrossing (VBAC) because of the overlapping between the Bi 6p energy level and the top of GaAs or InGaAs valence band. According to the Pauli Exclusion Principle, electrons with the same quantum number cannot occupy the same state; the top valence band will therefore be forced to split into two separate bands E+ and E-. The E+ energy band is shifted towards the conduction band, leading to a

reduced band gap. Figure 1.5 shows the scheme of VBAC in dilute bismuthides. Although there have been some skepticisms about CBAC/VBAC[21], its use is justified as a practical description of observed phenomena.

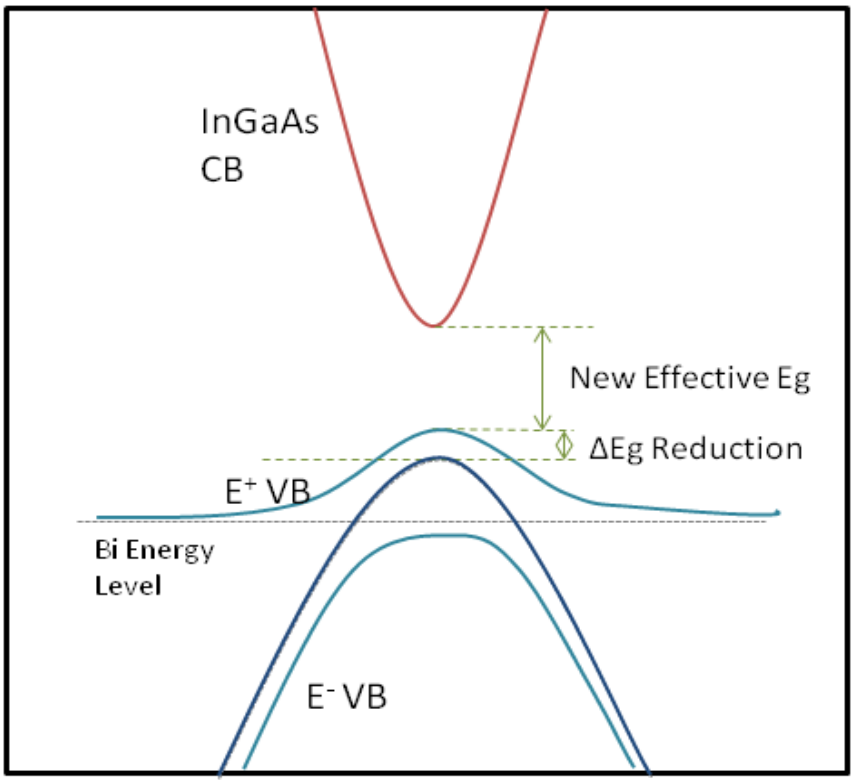

Figure 1.5 Scheme of VBAC in dilute bismuthides.

Researchers compared the electron mobility of GaNAs and GaBiAs as functions of N and Bi concentration respectively. The electron mobility of GaNAs drastically decreased from 1250 $cm^2V^{-1}s^{-1}$ to 100 $cm^2V^{-1}s^{-1}$; while that of GaBiAs still remained high when more than 2.5% Bi got incorporated. It is not a surprise to see that the increase of incorporation of nitrogen leads to a fast degradation of the mobility in

dilute nitrides because the interference is in the conduction band which matters most to electron transportation. It is believed that the increase of nitrogen concentration will make the conduction band structure more complex, and the inter-conduction band scattering will be more severe. For dilute bismuthides, they have VBAC which only interferes with the valence band and hardly affects the conduction band. The relatively high electron mobility gives dilute bismuthides a significant advantage over dilute nitrides.

Previous research was primarily focused on the growths and properties of GaBiAs. GaBiAs were first synthesized by metalorganic vapor phase epitaxy (MOVPE) in 1998 [22]. But the film quality was not ideal because it required higher growth temperature for MOVPE growth than MBE growth. Later, it was reported that GaBiAs were successfully prepared by MBE[23], [24]. Standard GaAs growth condition did not apply to the GaBiAs growth because bismuth is a good surfactant and it has a strong tendency to surface segregate. This surface segregation has also been observed in other heavy group III and V elements such as In, Tl and Sb [25]. The general rule is that it is harder for a heavy element to incorporate than a light element. For example, Sb can still be incorporated under conventional GaAs growth conditions [26], which are inapplicable for dilute bismuthides.

The unique requirements for bismuth to incorporate are low growth temperature (below 400 ˚C) and near 1:1 III/V ratio. Low growth temperature will keep the bismuth from being evaporated from surface as there has been report that bismuth is observed to evaporate when the surface is heated from 300 ˚C to 400 ˚C[27]. The right III/V ratio is the crucial factor to keep the surface smooth and free of droplets. For example, if the As overpressure is too low, Ga droplets will develop

on the surface; while if the As overpressure is too high, Bi droplets will form[28]. Furthermore, the temperature of the bismuth cell to incorporate bismuth, below 400 ˚C, is much lower than using it as a surfactant, usually between 550 ˚C to 650 ˚C. The temperature for bismuth to incorporate will generate Bi flux in the 10^{-8} Torr range[28].Up to now, the majority of GaBiAs are grown on GaAs with (001) oriented direction. But there has been work of GaBiAs grown on GaAs (311) orientation, and the bismuth incorporation is enhanced as compared to (001) orientation [29].

Lu *et. al.* proposed a kinetic model to explain the bismuth incorporation mechanism [30]. This model is used to predict the bismuth concentration and it is in good agreement with the experimental measurements. There are three different processes representing the Bi incorporation mechanism, the forbidden mechanism and the Bi loss mechanism. In the kinetic model, a Ga atom could insert between an As-atom-terminated surface and a Bi atom which is absorbed to the surface. The formation of an As-Ga-Bi bond indicates the successful incorporation of a bismuth atom. The forbidden mechanism has ruled out the possibility that a Ga atom could insert between two Bi atoms. The loss mechanism indicates that an As atom could insert between a Ga-Bi bond and knock the Bi atom out of the film.

Even under the right growth conditions, there is a limit of the amount of bismuth incorporated into the film, and it is difficult to produce a film with a uniform concentration through the whole thickness. There have been studies showing that the strain coming from the atomic radius difference between As and Bi could lead to an increase of the substitution energy and reduce the solubility of the solute atom Bi [28]. Therefore, it becomes more difficult to increase the Bi concentration. This effect will first be revealed as surface reconstruction induced atomic ordering, alloy clustering,

and phase separation. It is reported that $CuPt_B$-type atomic ordering is clearly observed in GaBiAs with a bismuth concentration of 1.2% and above [31].The occurrence of this type of atomic ordering suggests that a surface reconstruction containing [-110] oriented group V surface atom dimers are present during growths[31]. The extended x-ray absorption fine-structure spectroscopy (EXAFS) study has shown the evidence of an evolution from randomly distributed Bi anions to Bi dimers and clusters as the bismuth concentration increases [32]. This will have a significant impact on the optical and electrical properties of the dilute bismuthides.

Bi alloying provides a giant band gap bowing at a rate about 88meV/%Bi in the valence band of GaBiAs [33]. Although this is smaller as compared to 180meV/%N for [N]<1% in GaNAs [27], it is 7 times bigger than 12 meV/%In for InGaAs [34]. The previously reported GaBiAs growths on (311) oriented GaAs substrate have shown the same band gap reduction trend[29]. The PL peak width of GaBiAs broadens as bismuth concentration increases. The broadening could be due to Bi concentration fluctuations in some localized areas or even Bi clusters forming localized states in the band gap [35]. The temperature dependence of the PL emission energy of GaBiAs was found to be similar to that of the GaAs, which shifts to lower energies at elevated temperatures [33]. But researchers claimed that the temperature dependence of PL spectrum of GaNBiAs/GaAs at peak wavelength is as low as 0.09 nm/K, which is much smaller than 0.4 nm/K for GaInAsP/InP [36]. Other than the fundamental band gap, Fluegel *et. al.* also measured the excited state PL from the spin-orbit split-off hole band of GaBiAs [37]. It is reported that the spin orbit splitting energy Δ_{SO} shows a giant bowing effect that matches the change of the fundamental band gap in magnitude but with opposite sign [37]. The electron mobility only

decreases slightly from the introduction of Bi as a contrast to dilute nitrides because VBAC is primarily affecting the valence band rather than the conduction band. The electron mobility for sample with 1% Bi is 2800 $cm^2V^{-1}s^{-1}$ and 0.84% N sample is 920 cm^2/Vs, while that for GaAs is 3300 $cm^2V^{-1}s^{-1}$[38].

A small amount of efforts have been given to InGaBiAs[39]–[41]and there is still much room to explore. Growing quaternary alloy InGaBiAs has an edge over GaBiAs in terms of the possibility of depositing films that are lattice-matched to the InP substrate. Lattice matched samples are expected to have less defects and higher mobility, both of which are desirable for electronic materials. In addition to lattice-match, we choose InP substrate over GaAs because it is the platform of current telecommunication system. Therefore, in our work, we are mainly interested in the growth conditions and properties of InGaBiAs on InP.

1.4 **Molecular Beam Epitaxy Technique**

MBE is a well-established technique to grow epitaxial structures for both scientific research and industry production. It is the growth technique we used to produce the dilute bismuthides samples. The scheme of it is shown in Figure 1.6. The basic operation procedure is to generate molecular beams out of cells, interrupt the beam fluxes by opening and closing shutters and deposit elements from each desired cell on a crystalline substrate at elevated temperatures under ultra high vacuum (UHV). The thickness of the deposition layer could be precisely controlled at atomic scale. The crucial factor distinguishing MBE from LPE or atmospheric pressure VPE lies in its kinetics dominated nature. Rather than growing near thermal equilibrium condition, MBE is highly governed by the interaction between the adatoms and the outermost atomic layer of the substrate. This guarantees the possibility to create some

metastable alloys or structures under thermodynamic immiscible conditions. Besides, due to the high mobility of the surface atoms, growths carried by MBE can happen at a much lower temperature than the bulk melting temperature of the source materials. This will greatly reduce the thermodynamic equilibrium defect density. Finally, the UHV environment provides the compatibility with in situ surface diagnostic analysis tools such as reflection high energy electron diffraction (RHEED), low energy electron diffraction (LEED), laser interferometry (LI) and reflection mass spectrometry (REMS). These powerful measurements offer good control over the growth and eliminate much of the guess work.

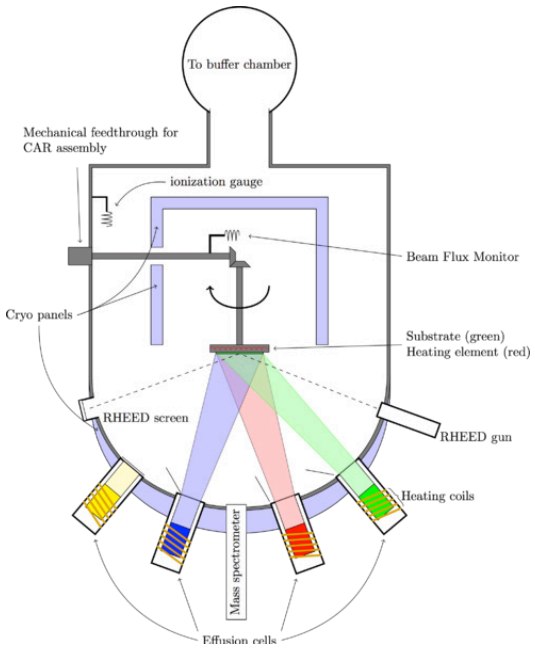

Figure 1.6 Scheme of MBE (http://en.wikipedia.org/wiki/Molecular_beam_epitaxy)

MBE growth is a complicated process and is decided by several mechanisms all together. From a thermodynamic point of view, the driving force for nucleation and film formation for single atom comes from the lower free energy in the solid phase than in gas phase. When several atoms stick together to nucleate an island, the free energy as a whole will first go up then go down with the increase of island radius. This is dependent on the tradeoff between the increased surface free energy and decreased phase transition energy. However, MBE growth is far from thermal equilibrium and it includes a series of complicated process: deposition, evaporation, surface diffusion, nucleation and growth.

There are three basic MBE growth modes regarding thermodynamics: (a) Volmer-Weber (VW: island growth), (b) Frank-van der Merwe (FM: layer by layer) and (c) Stranski-Krastanov (SK: layer plus island) as shown in Figure 1.7.For homogeneous epitaxy, it is energetic favorable for atoms to grow in FM mode because the number of bonds formed in this mode is larger than island growth and the total Gibbs free energy is lower. For heterogeneous epitaxy, other than the number of bonds formed, the bonding energy difference between AA and AB is important (for atom A depositing on substrate B) as well. If AA is larger than AB, island growthis preferable, and if AB is larger than AA, layer growth is preferable. The SK mode includes island growth too, but this is mostly due to strain rather than the bonding energy difference. The FM mode is preferred for thin film growth while the SK mode is a conventional method for quantum dot growth.

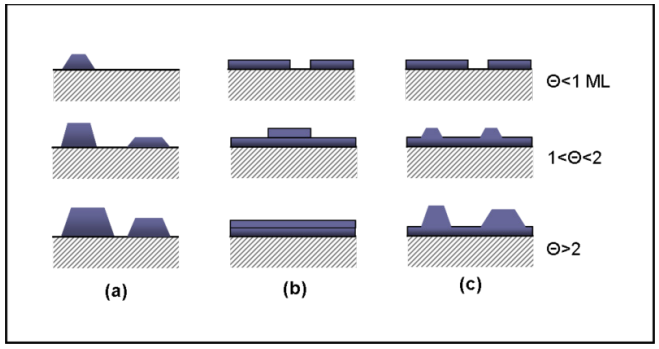

Figure 1.7 Three main growth modes in MBE, (a) VW, (b) FM and (c) SK. (http://en.wikipedia.org/wiki/File:GrowthModes.png)

Two dimensional epitaxial growth modes can also be divided into two types regarding kinetics: (1) layer-by-layer mode and (2) step-flow mode. The major difference between these two modes resides in the separation among islands and the atomic surface diffusion length. The scheme of the two growth modes are shown in Figure 1.8. In layer-by-layer mode, one adatom diffuses on the surface until it meets another adatom and nucleates. The following arrived adatoms will coalesce with the nuclei and grow at the same level. As a contrast, in step-flow mode, the adatoms will diffuse and stick to a step-edge, and steps will grow as opposed to a complete layer. In general, at the growth condition under low growth temperature, high flux and low step density, layer-by-layer growth mode is preferred over step-flow mode; otherwise, step-flow mode is favorable.

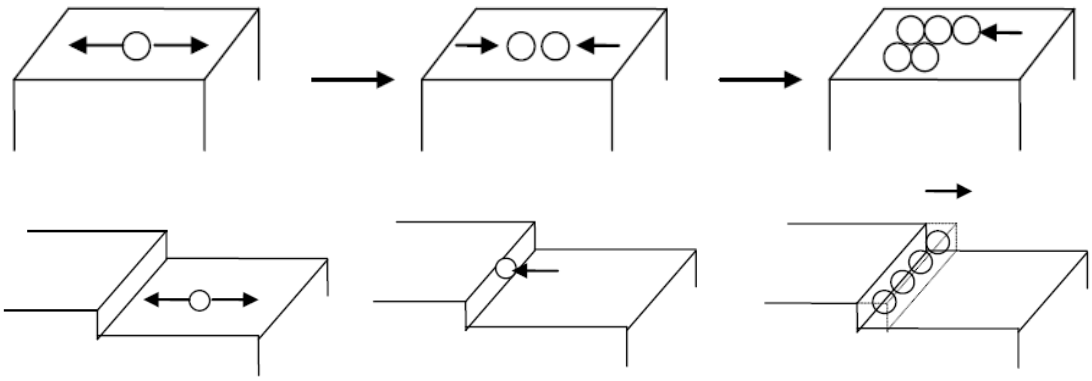

Figure 1.8 Scheme of layer-by-layer mode (up) and step-flow mode (bottom). (http://www.eng.utah.edu/~lzang/images/lecture-33.pdf)

The surface morphology of the epilayer is largely determined by the growth temperature. If the growth temperature is too low, the surface will have statistical roughening due to the low mobility of the adatoms and they tend to follow the Poisson's statistics. When the substrate is heated to high temperatures, the adatoms have more freedom to move around, and they tend to have FM mode growth (if it is preferable). When the temperature is further increased, the layer by layer growth will transform into step flow growth because of the longer diffusion length due to the elevated temperature. In the end, if the temperature keeps going up, thermal roughening will happen when it is energetic favorable for newly arrived adatoms to half-cover the surface.

RHEED is a technique that is extremely useful to monitor the *in-situ* growth situation. A RHEED system is composed of an electron gun and a phosphorus screen as shown in Figure 1.9. The high energy electron emitted from the electron gun under ultra high voltage (usually 10 kV) will strike the surface of the sample at a grazing incident angle θ. The incident electrons will diffract from the surface and form

diffraction pattern on the phosphorus screen (detector/CCD).

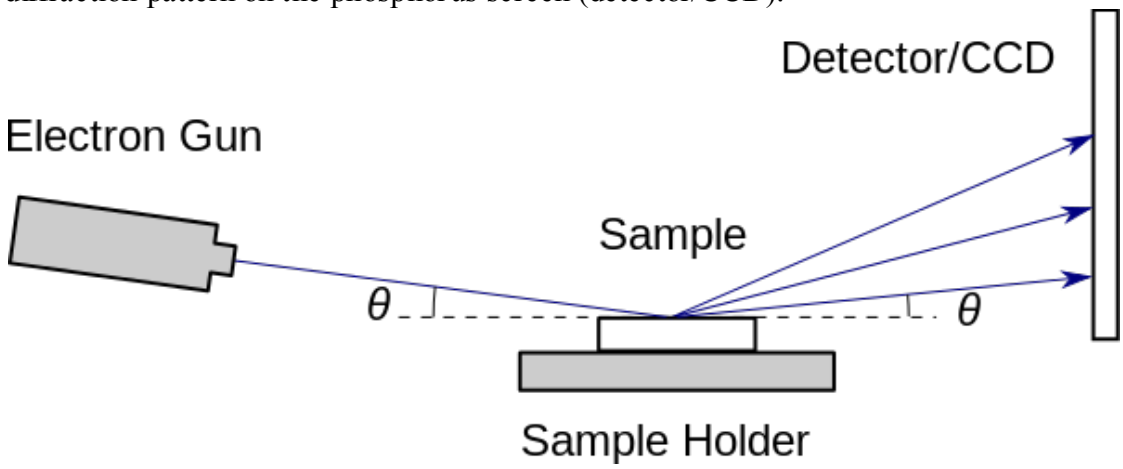

Figure 1.9 Scheme of RHEED (http://en.wikipedia.org/wiki/Reflection_high-energy_electron_diffraction)

According to the variation of the diffraction pattern, we can easily tell the growth rate, growth mode, and the smoothness of the surface. The growth rate can be told from the periods of the RHEED intensity oscillation, which reaches the maximum when the surface is covered by a full layer of atoms and the minimum when the surface is half covered by atoms, as shown in Figure 1.10. A layer by layer growth mode will exhibit clear streaks; while an island growth mode will give spotty patterns. The smoothness of the surface is judged by the brightness of the RHEED signal.

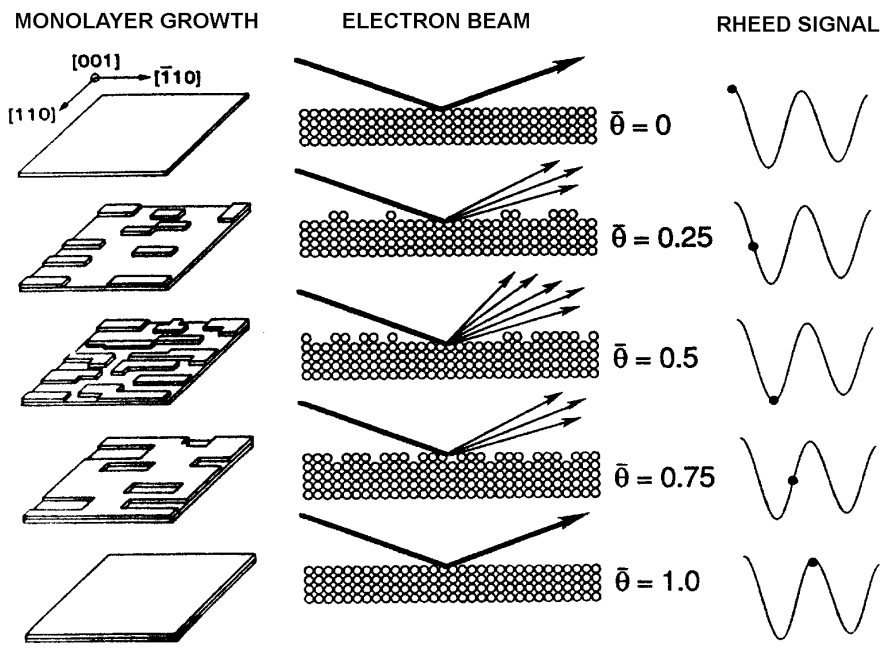

Figure 1.10 RHEED oscillation intensity correspondences to surface smoothness (http://lase.ece.utexas.edu/mbe.php)

Band edge (BE) thermometry is used to monitor the substrate temperature. It has a wide spectrum light source shining on the back of the substrate. The detector records the light intensity transmitted through the wafer over the whole spectrum. From the shape of the transmitted spectrum, we can locate the band edge (where the light starts to get absorbed), which is a function of temperature. Then it converts the band edge signal back to temperature. It is especially important for low temperature growth such as bismuth containing material growths because the efficiency of a conventional pyrometer falls quickly when the temperature is below 400 °C.

1.5 **Dissertation Overview**

This dissertation focuses on the growth, characterization and modeling of InGaBiAs on InP substrate with a focus on optoelectronic applications. More specifically, Chapter 2 describes in detail growth conditions, composition, strain and relaxation and morphology characterization. Chapter 3 discusses theoretical and experimental study of optical properties. Chapter 4 demonstrates that InGaBiAs:Si is an ideal transparent contact material in the IR range. Chapter 5 calculates the efficiency of a solar cell with a new nanostructure composing of dilute bismuthides. Finally, Chapter 6 is extended to the future work in this area, some challenges and possible solutions. It also provides some conclusions based on preceding chapters.

Chapter 2

GROWTH CONDITIONS, COMPOSITION, STRAIN AND RELAXATION, CLUSTTERING STUDY OF INGABIAS

In the previous chapter, we have discussed the motivation and the main synthesis technique to study the class of materials, dilute bismuthides. This Chapter will narrow down the range of dilute bismuthides to a special kind, InGaBiAs. It will discuss the growth, composition, strain and relaxation, and morphology study of InGaBiAs. Section 2.1 discusses the growth conditions of this material using MBE. Section 2.2 compares two measurements to study the composition: high-resolution X-ray diffraction (HR-XRD) and Rutherford backscattering spectroscopy (RBS), and points out the pros and cons in each method. Section 2.3 reports the strain and relaxation results from reciprocal space mapping (RSM). Section 2.4 studies the surface morphology using scanning electron microscopy (SEM) and the composition in the bulk at atomic scale using high angle annular dark field-scanning transmission electron microscope (HAADF-STEM). Section 2.5 summarizes the results presented in the previous sections.

2.1 Overview of the Growth Conditions

In Section 1.4, we mentioned a powerful tool in synthesizing complicated structures or metastable materials, MBE. In this section, we will discuss the detailed growth conditions of $In_xGa_{1-x}Bi_yAs_{1-y}$ on InP:Fe substrates using MBE. $In_xGa_{1-x}Bi_yAs_{1-y}$ samples were grown on (001) oriented InP:Fe substrates in an OSEMI NextGen III-V solid source molecular beam epitaxy (MBE) system, equipped with ten sources. The

gallium and indium cell are dual-heater (base and tip) effusion cells, and the bismuth cell is a single heater effusion cell. All growths use a two-zone valve cracker source for As_2. The beam equivalent pressure (BEP) was measured using an ionization gauge and can be deemed as the flux times a coefficient. The substrate temperature was monitored by the band edge thermometry. The substrate is first elevated to 565 °C to desorb the native oxide on InP substrate under an As overpressure of 1.0×10^{-5} Torr, which is indicated by RHEED pattern transition from hazy random pattern to a streaky 2x4 reconstruction pattern. The substrate temperature is then reduced to a low number ~300 °C, and the As BEP is reduced to 2.0×10^{-6} Torr. A 50-70 nm buffer layer $In_{0.53}Ga_{0.47}As$ lattice matched to the substrate is first deposited onto the substrate, and a 300 nm $In_{0.53}Ga_{0.47}Bi_yAs_{1-y}$ film is deposited on top of the buffer layer. In the experiments, two parameters (growth temperature and Bi BEP) are individually varied to study their effect on the composition. During all growths, the RHEED displays clear streaky 2x4 rotation patterns.

Figure 2.1 shows the effects on Bi concentration from two independently varied growth parameters, growth temperature and Bi BEP. In Figure 2.1 (a), Bi content generally increases as the growth temperature decreases and reaches a plateau when the growth temperature is below 280 °C. Figure 2.1 (b) indicates that at constant growth temperature, Bi concentration gradually increases with increased Bi BEPs. The highest uniform Bi content we obtained so far is 5.8%.One sample grown at 300 °C with Bi BEP at 3.1×10^{-8} Torr has an average Bi concentration around 6.75%.It has a Bi concentration gradient through the thickness, which I will discuss in Section 2.4. Therefore, we can draw a conclusion that low growth temperature and high Bi BEP

are two important factors to increase Bi concentration. But there are limits in these two methods and I will discuss them in detail in Section 2.4.

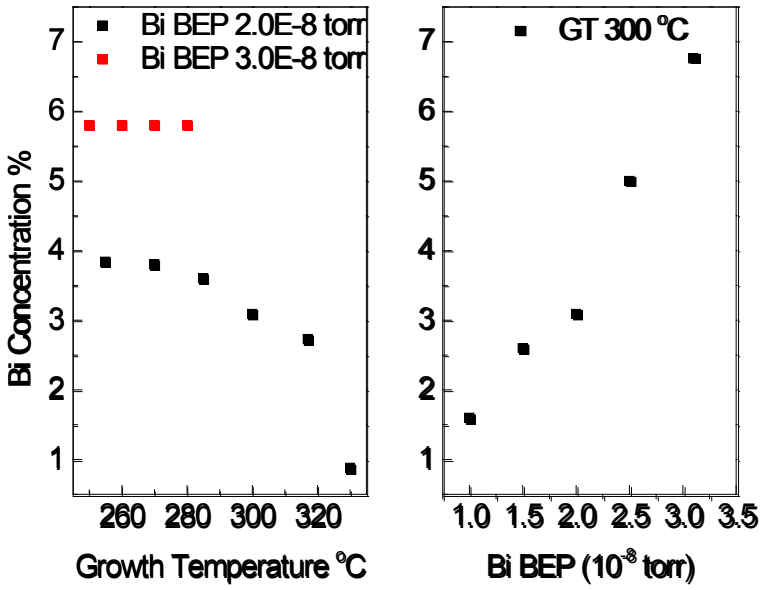

Figure 2.1 Bismuth concentration as a function of different growth conditions: growth temperature and Bi BEP [42]. (Reproduced with permission from [Y. Zhong, P. B. Dongmo, J. P. Petropoulos, and J. M. O. Zide, "Effects of molecular beam epitaxy growth conditions on composition and optical properties of InxGa1-xBiyAs1-y," Appl. Phys. Lett., 100, 112110, 2012]. Copyright [2012], AIP Publishing LLC. http://dx.doi.org/10.1063/1.3695066)

2.2 **Composition Study**

The bismuth concentration and the quaternary compound composition are determined by two methods: HR-XRD and RBS. In both methods, the composition is told by matching the simulation result with the experimental measurement. HR-XRD is good at sensing the small variation of In/Ga ratio but less accurate to tell bismuth concentration due to the fact that the XRD peak position could be easily affected by lattice constant super dilation or uneven bismuth concentration distribution. RBS

isgreat to determine the bismuth concentration due to its high sensitivity to heavy element bismuth but not very effective to detect In/Ga ratio change because the resolution is only good at 1%. The combination of the two methods can be used to reliably determine the composition of each sample.

The HR-XRD measurements are carried out by a high-resolution PANalytical X'Pert PRO materials research diffractometer at University of Delaware. The source is a 1.8kw sealed ceramic copper X-ray tube. A triple crystal X-ray path adopts a three bounce (022) channel cut Ge analyzer in front of the detector to determine the angular acceptance of the detector. In this measurement, the data is collected by using a ω-2θ coupled scan. The sample is rotated about ω degree (the angle between the X-ray source and the sample) per unit time while the detector moves twice the speed, 2θ (the angle between incident beam and the detector), for symmetric scans. We use the X-ray intensity-2θ pattern to calculate the composition of the sample through Bragg's law. According to the peak position, we can calculate the corresponding d spacing along (004) orientation and therefore the lattice constant, given by Equation 2.1 and 2.2. Using Vegard's law and the lattice constant of GaAs (5.653 A and 1.42 eV), InAs (6.058 A and 0.36 eV), InBi (6.686A and -1.63eV), GaBi (6.324 A and -1.45eV) [43], we can get the Bi concentration. The method is simple and fast and it can give quantitative values.

$$2d \sin\theta = n\lambda \qquad \text{Equation 2.1}$$

$$a = \sqrt{h^2 + k^2 + l^2}\, d \qquad \text{Equation 2.2}$$

d is the (004) plane spacing; θ is the incident angle of the X-ray beam; n is an integral number; λ is the wavelength of Cu Kα1, which equals to 1.54056 A; a is the

in-plane lattice constant of InGaBiAs relative to the surface, and (hkl) are the Miller indexes, which equal to (004) in this case.

Figure 2.2 shows ω-2θ HR-XRD scans using Cu Kα1 radiation for three $In_xGa_{1-x}Bi_yAs_{1-y}$ samples grown along the (004) direction. Black curves are experiment measurements and blue lines are corresponding to simulation results. The InP substrate peak is noted at the sharp peak at 31.6682°, and the peak at a smaller angle than the substrate peak corresponds to the $In_xGa_{1-x}Bi_yAs_{1-y}$ film peak. The peak at the small angle indicates a lattice constant increase relative to the substrate. This increase is brought by the incorporation of large bismuth atoms rather than the variation of In/Ga ratio, which can be confirmed by the change of the buffer layer peak position, a broad bump between the substrate peak and the film peak. The small-period oscillations are called thickness fringes, which indicate our samples have very smooth epitaxial interfaces. The large-period oscillations come from the buffer layer $In_{0.53}Ga_{0.47}As$ modulation, which is much thinner than the film. From sample to sample, indium concentration varies by approximately ±2% as can be told from the variation of the position of the buffer layer peak. This is mainly due to the systematic errors and the equipment accuracy, which is unavoidable in our experiments. The samples in this figure are grown at 255°C (3.85%Bi), 285°C (3.60%Bi), 300°C (3.09%Bi) respectively. Generally, we observe Bi concentration increasing when the growth temperature decreases, as shown by the film peak moving to lower angles. Despite this trend, determination of Bi content from ω-2θ scans directly is not accurate due to the In/Ga ratio variation. In addition, the incorporation of large Bi atoms into $In_{1-x}Ga_xAs$ will lead to lattice super dilation, which means the lattice constant of the unit cell around the bismuth atom will increase. This will render the theoretical lattice

constants of InAs, GaAs, InBi and GaBi to be no longer applicable. Therefore, ω-2θ scans alone are not reliable to determine Bi concentration, but its high sensitivity to the In/Ga ratio is still very valuable in determining the quaternary compound composition. Thus, we use RBS which complements HR-XRD ω-2θ scans to determine Bi concentration.

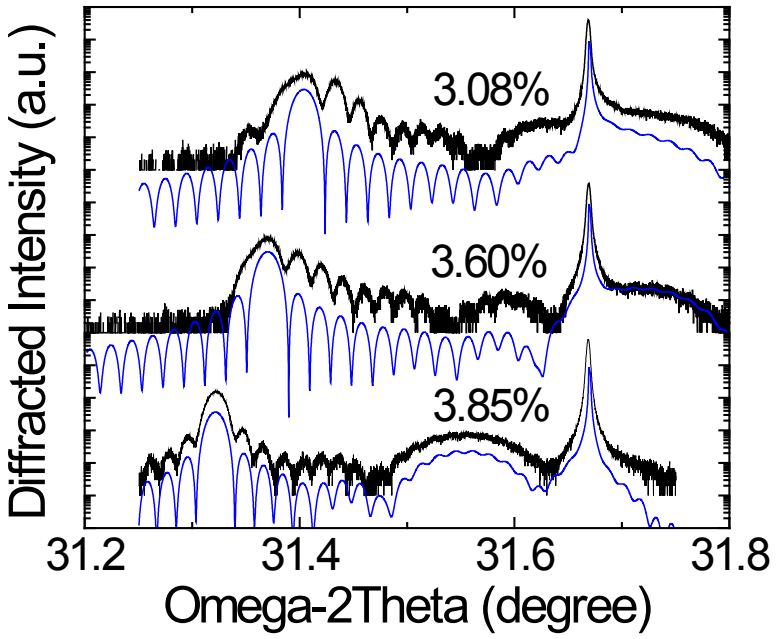

Figure 2.2 HR-XRD (004) ω-2θ scans for $In_xGa_{1-x}Bi_yAs_{1-y}$ epilayers on InP (black lines) with Bi content of 3.08%, 3.60% and 3.85% (determined by RBS). Blue lines are simulations[42]. (Reproduced with permission from [Y. Zhong, P. B. Dongmo, J. P. Petropoulos, and J. M. O. Zide, "Effects of molecular beam epitaxy growth conditions on composition and optical properties of InxGa1-xBiyAs1-y," Appl. Phys. Lett., 100, 112110, 2012]. Copyright [2012], AIP Publishing LLC. http://dx.doi.org/10.1063/1.3695066)

RBS is ideal to quantitatively analyze Bi concentration because of its high sensitivity to heavy elements like bismuth. Figure 2.3 shows the scheme of RBS. The principle of RBS is that a beam of high energy particles (usually α particles, He2+, less commonly, protons, in the MeV range) bombards the sample, and part of projectiles will be backscattered by the sample's atomic nuclei and then be collected by the energy sensitive detector. RBS can be used to quantitatively measure the composition, film thickness and depth profile of individual elements. It has higher sensitivity to detect the signal from heavy elements, which happens to fit our situation. High channeling number corresponds to ions with high backscattered residue energy, which are also ions backscattered by heavy atoms or atoms close to the sample's surface. The composition scan is usually measured at random aligned direction, which means that the direction of the incident beam is at a random angle corresponding to the sample. This geometry provides a large chance for the ion beams to bombard the atoms through the film thickness. In addition to composition measurements, RBS can also be used to study the interstitial defects using channeling alignment. When a sample is channeled, the rows of atoms in the lattice are aligned parallel to the incident ion beam. The bombarding ions will be backscattered by the first few monolayers of the material at the same rate as a non-aligned sample. But backscattering from atoms lying behind the thin surface layer in the lattice will be drastically reduced since these atoms are shielded by the atoms in the surface layers. Therefore, in a perfect crystal with no interstitial defects, the channeling signal should be significantly lower than the randomly aligned spectrum, and there should be no peak in the channeling spectrum. On the other hand, if there are interstitial defects, a direct scatter peak should be observed in the channeling data.

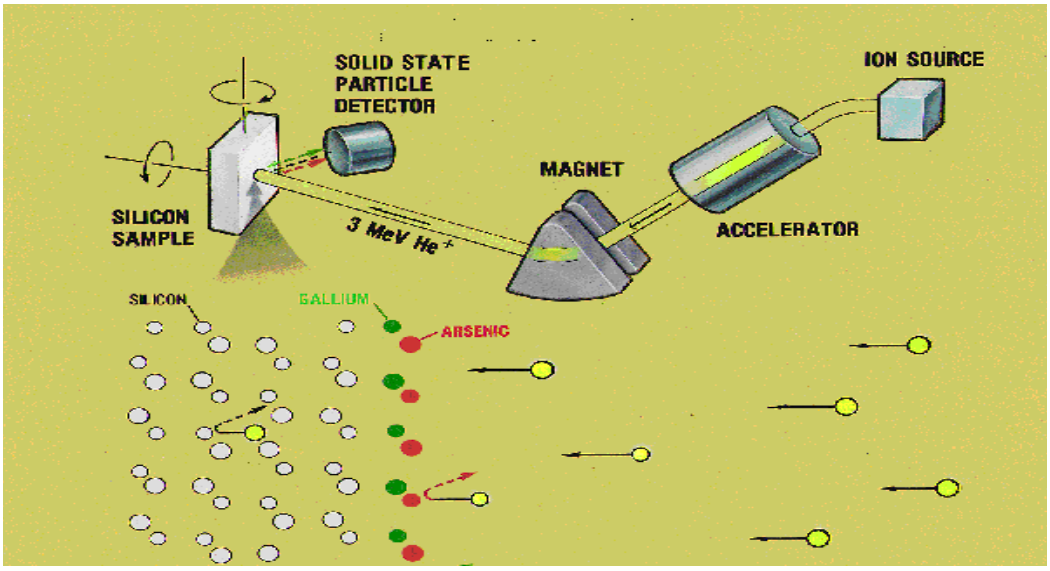

Figure 2.3 Scheme of the working principle of RBS (http://www.mrsec.harvard.edu/cams/RBS.html)

In Figure 2.4, we showed three different RBS spectra of $In_{0.49}Ga_{0.51}Bi_{0.03}As_{0.97}$ directly deposited on an InP substrate. The black squares are experimentally collected from a random-angle alignment; the magenta line is also an experimental measurement, but at an aligned angle; the red line is a simulated spectrum of the random alignment. The simulation line is the sum of signals from each element In, Ga, As, P and Bi, which is indicated individually. Bi, as the heaviest element among the four, shows up in the highest channel number. It is followed by the signal of In, As, and Ga in the order of the decrease of the atomic weight among these elements. P signal shows up in the lowest channel number because it is from the substrate, which is 500 nm below the InGaBiAs layer. The thickness of the layer can be told from the length of the signal stage from each element, and the concentration of each element can be easily determined by the height of the signal. The high crystalline quality of this sample is demonstrated by a much lower yield in the aligned spectrum than the

random spectrum. There is no peak shown up on the aligned spectrum, which indicates that almost all Bi atoms incorporate substitutionally instead of occupying the interstitial sites.

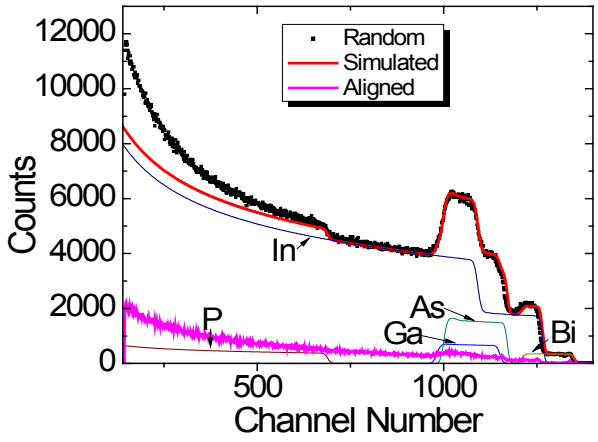

Figure 2.4 Randomly-oriented, simulated, and aligned RBS spectrum for $In_{0.49}Ga_{0.51}Bi_{0.03}As_{0.97}$ epilayers. Components of In, Ga, Bi, As, and P are indicated based on simulation[42]. (Reproduced with permission from [Y. Zhong, P. B. Dongmo, J. P. Petropoulos, and J. M. O. Zide, "Effects of molecular beam epitaxy growth conditions on composition and optical properties of InxGa1-xBiyAs1-y," Appl. Phys. Lett., 100, 112110, 2012]. Copyright [2012], AIP Publishing LLC. http://dx.doi.org/10.1063/1.3695066)

2.3 **Strain and Relaxation Study**

The aforementioned samples are pseudomorphic alloys. The degree of strain and relaxation is a very important concern in optoelectronic materials because it will greatly affect the band gap, which is one of the most important parameters for optoelectronic materials. A scheme of strained and relaxed film is given in Figure 2.5(a)-(c). When the deposited film has a lattice constant larger than the substrate and is forced to epitaxially grow with the same lattice constant as the substrate, the film will be under compressive strain, as shown by Figure 2.5 (a); otherwise it is described

as tensile strain, as shown in Figure 2.5 (b). If the thickness of the deposited film exceeds the critical thickness, the film will relax and grow at its own lattice constant, which will cause the formation of thread dislocations, as shown in Figure 2.5 (c). Dislocations resulting from relaxation can form deep level recombination centers and affect thermal stability and other material properties.

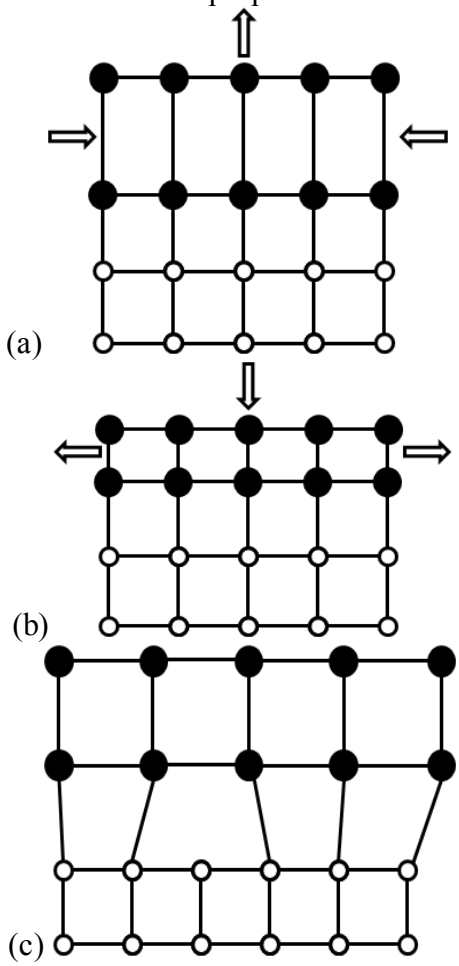

Figure 2.5 (a)-(c) Scheme of compressive, tensile strain and relaxation

Figure 2.6 (a)-(c) shows the relative change of the conduction band and valence band position of SiGe due to compressive strain, relaxation and tensile strain.

The conduction band has a six-fold degenerate bands Δ6, corresponding to the six [001] orientations. When the epilayer is relaxed, the conduction band and the valence band energy level will stay unaffected. As a comparison, the application of strain will break the degeneracy of the conduction band states into a four-fold and two-fold set: Δ4 and Δ2 and split the heavy hole and light hole band in the valence band. The net change of the band gap of the epilayer under strain will be determined by the relative change of both conduction band and valence band. Sometimes, strained materials are adopted in optoelectronic device to effectively tune the band gap. For example, the state of art InGaAs quantum well (QW) laser operating at 1 μm used strained materials to reach the long wavelength [15], and this could not be achieved by materials being lattice matched to the substrate. But generally, strained materials are not as stable as lattice matched materials due to their metastable nature.

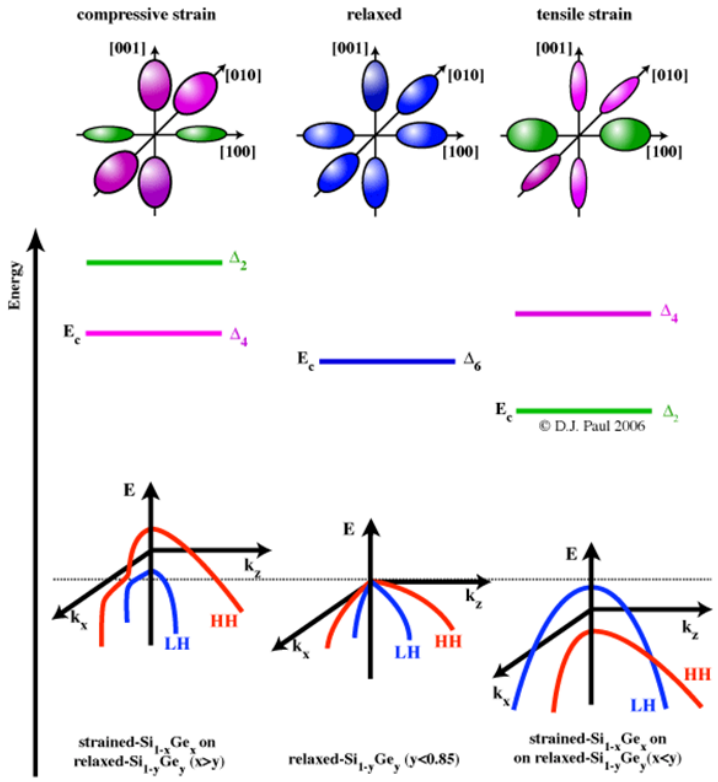

Figure 2.6 (a)-(c) The relative band position change in SiGe under compressive strain, relaxation and tensile strain. (http://www2.warwick.ac.uk/fac/sci/physics/current/postgraduate/regs/mpags/ex5/strainedlayer/introduction/)

RSM, which records the X-ray diffraction intensity at different recombinations of ω and 2θ, is a common tool to study strain and relaxation. The rocking curve mode (ω scan) is an arc centered on the origin as shown in Figure 2.7 (a). The detector scan mode (2θ scan) is an arc along the Ewald sphere circumference as indicated in Figure 2.7 (b). The couple scan mode (ω-2θscan) is a straight line pointing away from the origin as can be observed in Figure 2.7 (c). The squares and dots in Figure 2.7 represent reciprocal lattice points (RELP) of the substrate and the film individually.

The two small semi-spheres on the bottom represent the Laue zones ($\omega<0$ and $2\theta>\omega$) where the diffraction forbidden regions are. The reciprocal space map uses multiple scans in order to observe both the film and substrate peaks.

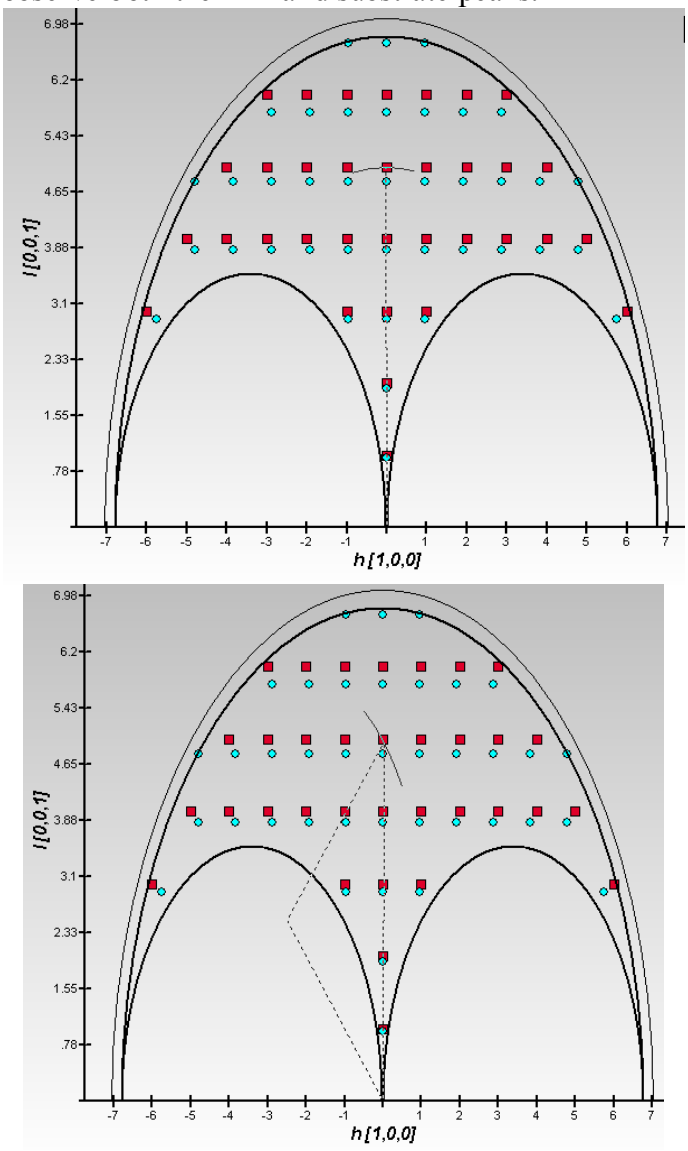

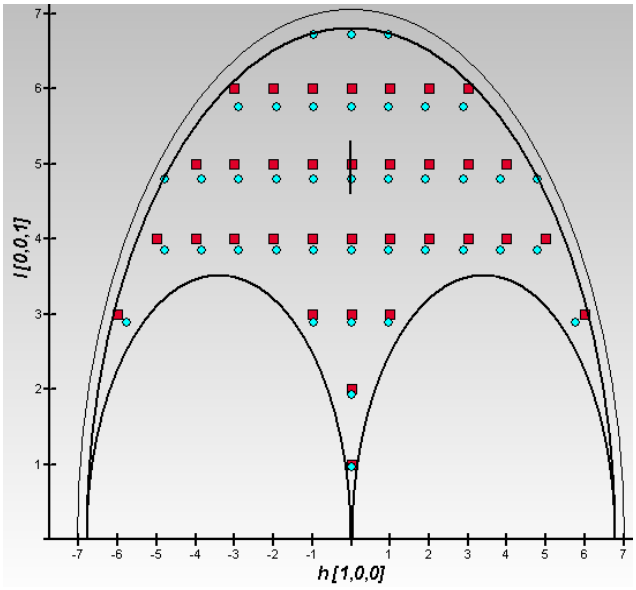

Figure 2.7 (a)-(c) RSM rocking curve, detector and ω-2θ scanning mode [44]

From the RSM results, we can calculate the cross plane and in plane lattice constant $a_{\perp}$ and $a_{||}$ (relative to the surface) for both the substrate and the film from Bragg's law. Based on them, we can get the relative lattice mismatch in both parallel ($f_{||}$) and perpendicular ($f_{\perp}$) directions relative to the surface given by the equations below [45]:

$$f_{||} = \frac{\Delta a_{||}}{a(s)} = \frac{\Delta(\frac{1}{k_{||}})}{1/k(s)} = \frac{k(s)-k_{||}(l)}{k_{||}(l)} \qquad \text{Equation 2.3}$$

$$f_{\perp} = \frac{\Delta a_{\perp}}{a(s)} = \frac{\Delta(\frac{1}{k_{\perp}})}{1/k(s)} = \frac{k(s)-k_{\perp}(l)}{k_{\perp}(l)} \qquad \text{Equation 2.4}$$

where the indices l and s indicate the layer and the substrate, a is the lattice constant and k represents the reciprocal vector. The equivalent lattice mismatch f between the substrate and the film could be estimated based on the bulk elastic theory for homogeneous deformation:

$$f = (f_{\perp} - f_{\parallel})\frac{1-\nu}{1+\nu} + f_{\parallel}$$ Equation 2.5

where ν is Poisson's ratio. The degree of relaxation can be expressed by the ratio between the mismatch at the interface and the mismatch for a completely relaxed layer[46].

$$R = \frac{a_{\parallel} - a(s)}{a_{relaxed} - a(s)} = f_{\parallel}/f$$ Equation 2.6

Figure 2.8 shows the asymmetric RSM scan along (224) direction for $In_{0.520}Ga_{0.480}Bi_{0.036}As_{0.964}$. The x and y axes represent the horizontal (110) and perpendicular (001) directions with respect to the sample's surface. The upper peak corresponds to the InP substrate and the lower peak originates from the $In_{0.520}Ga_{0.480}Bi_{0.036}As_{0.964}$ film. The series of peaks along (001) are thickness fringes, which have been observed in the previous ω-2θ scans. The appearances of thickness fringes confirm a smooth interface between the film and the substrate and the good crystalline quality of the film. As shown in the figure, the two peaks have the same horizontal coordinate, indicating that they have the same in-plane lattice constants and the film is under 100% strain. The film peak has a smaller coordinate in y axis than the substrate, which indicates that the film has a larger cross-plane lattice constant than the substrate and the film is under compressive strain. We also observed a broadening of the film peak along ω scan direction, which is less common than a broadening along the in-plane direction. This kind of broadening is usually caused by wafer curvature or dislocation-induced tilt/twist [47].

One interesting point we learned from the RSM result is that the thickness of this fully strained sample greatly exceeds the critical thickness predicted from a simplified Matthews-Blakeslee model (273 nm opposed to 69 nm) as shown in

Equation 2.7 [48]. This model assumes both the epilayer and substrate are isotropic elastic materials.

$$h = \frac{a(1-\frac{\nu}{4})}{4\sqrt{2}\pi(1+\nu)\epsilon}\left[\ln\left(\frac{\sqrt{2}h}{a}\right) + \theta\right] \qquad \text{Equation 2.7}$$

where h is the critical thickness, a is the substrate lattice constant, ν is Poisson's ratio, $\epsilon = (a_{epilayer} - a_{sub})/a_{epilayer}$, and θ represents the dislocation core energy which approximately equals to 1.

Researchers have reported similar observations in other low-temperature growths that the thickness of the sample has greatly exceeded the critical thickness but the film remains strained [24]. One explanation is that the current growth condition (low growth temperature) cannot provide enough thermal energy to permit dislocation motion and release the strain [31].

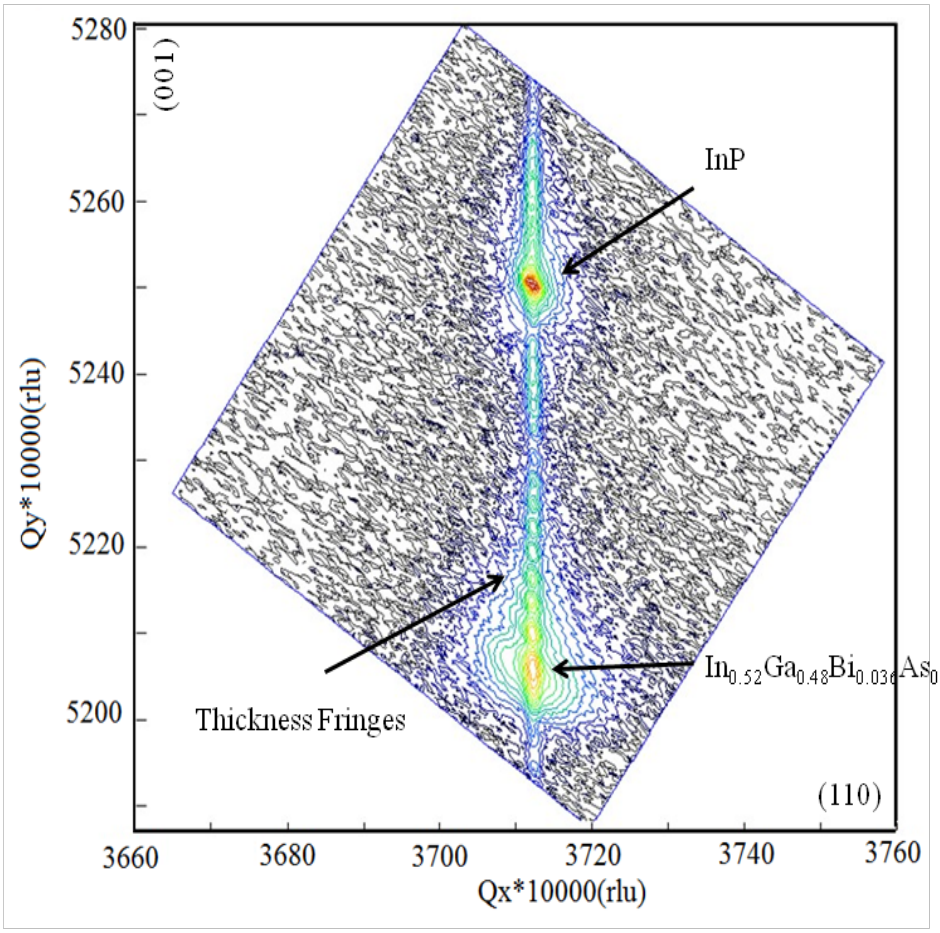

Figure 2.8 (224) RSM scans of pseudomorphic InGaBiAs on InP [42]. (Reproduced with permission from [Y. Zhong, P. B. Dongmo, J. P. Petropoulos, and J. M. O. Zide, "Effects of molecular beam epitaxy growth conditions on composition and optical properties of InxGa1-xBiyAs1-y," Appl. Phys. Lett., 100, 112110, 2012]. Copyright [2012], AIP Publishing LLC. http://dx.doi.org/10.1063/1.3695066)

To grow nominally lattice-matched samples, the In/Ga ratio is decreased to compensate the lattice constant increase brought by the incorporation of bismuth. Three nominally lattice-matched samples were grown at different growth temperatures at 285 °C, 300 °C and 317 °C individually. According to RBS measurements, they have Bi concentration of 3.00%, 2.90% and 2.78% respectively. All films are directly

deposited onto the substrate without a buffer layer to eliminate the lattice mismatch between the buffer layer and the thin film. Figure 2.9 (a) compares the ω-2θ scans of the three samples using HR-XRD. Similar to the previous ω-2θ scans, the tall peak is corresponding to InP substrate peak, and the small peak adjacent to it is from the film $In_xGa_{1-x}Bi_yAs_{1-y}$. The lattice mismatches of the three samples are 0.21% (3.00% Bi), 0.10% (2.90% Bi) and 0.08% (2.78% Bi) respectively. These mismatches are negligible, and our samples are very close to the lattice-matching condition. Figure 2.9 (b) and 2.9 (c) exhibits RSM scans for the sample with 3.00% Bi and the sample with 2.78% Bi in (224) and (004) direction respectively. These RSM scans further confirmed that the degrees of the lattice mismatch in our samples are very small.

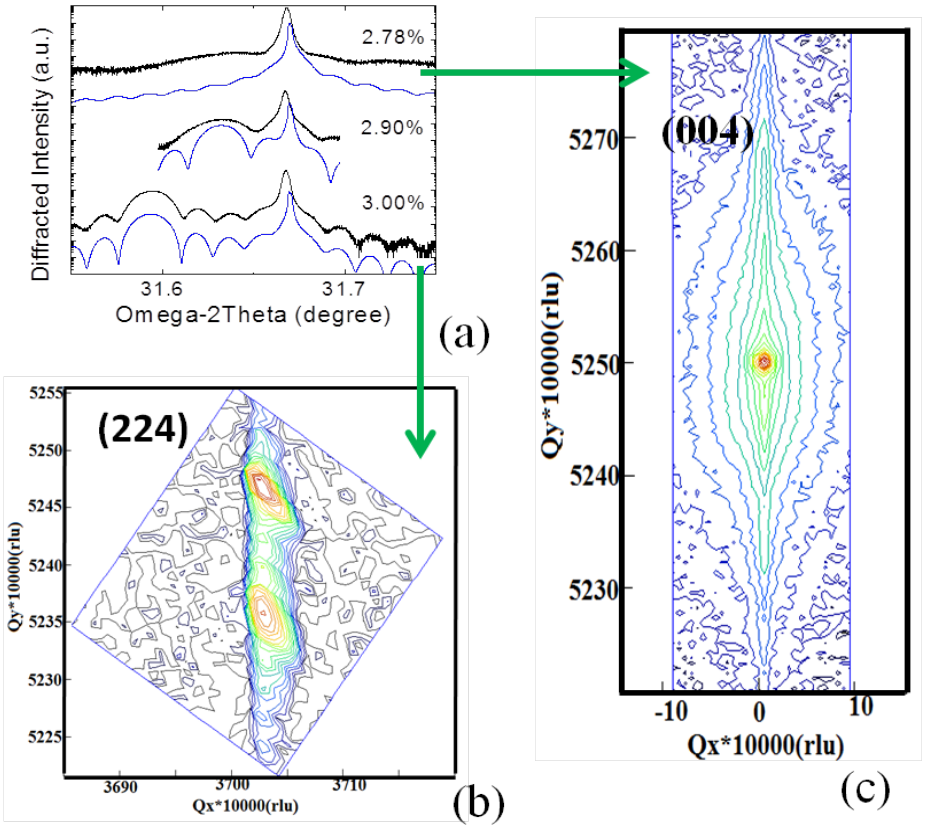

Figure 2.9 (a)-(c) ω-2θ and RSM scans of nominally lattice matched InGaBiAs samples[42]. (Reproduced with permission from [Y. Zhong, P. B. Dongmo, J. P. Petropoulos, and J. M. O. Zide, "Effects of molecular beam epitaxy growth conditions on composition and optical properties of InxGa1-xBiyAs1-y," Appl. Phys. Lett., 100, 112110, 2012]. Copyright [2012], AIP Publishing LLC. http://dx.doi.org/10.1063/1.3695066)

2.4 **Surface Morphology and Composition Study at Atomic Scale**

In Section 2.1, we have demonstrated that Bi concentration increases with increased Bi BEPs or decreased growth temperature, but there are limits on both methods. It has been reported that in the growths of GaBiAs, if the Ga flux is too high, Ga droplets will appear; while if the Bi flux is too high, the droplets will be Bi rich [28]. In the growths of InGaBiAs, droplets begin to appear when the growth temperature is above 285 $^{\circ}$C or Bi BEP is above 2.0 x 10^{-8}Torr. Figure 2.10 (a)-(f) compare optical microscope images of the surfaces of samples under different growth temperatures and Bi BEPs. Comparing Figure 2.10 (a)-(c), the density of the droplets increases as the growth temperature elevates. This is because Bi tends to act as surfactant at high growth temperature. Figure 2.11 (a)-(c)exhibit that the droplet density increases significantly when we raise the Bi BEPs. At the given growth conditions, the epilayer cannot incorporate the increased Bi atoms fast enough. Therefore, droplets will accumulate on the surface. From these figures, we can see that the density of the droplets strongly depends on the growth temperature and the Bi BEP.

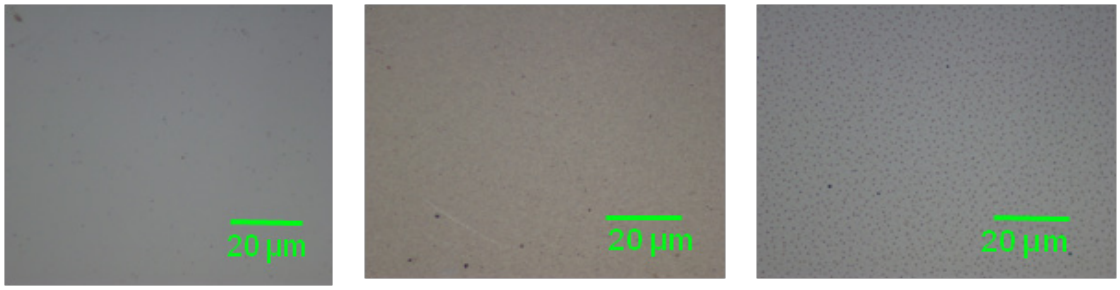

(a) 285 ˚C (b) 300 ˚C (c) 317 ˚C

Figure 2.10 (a)-(c) Droplets density variation as the growth temperature increases

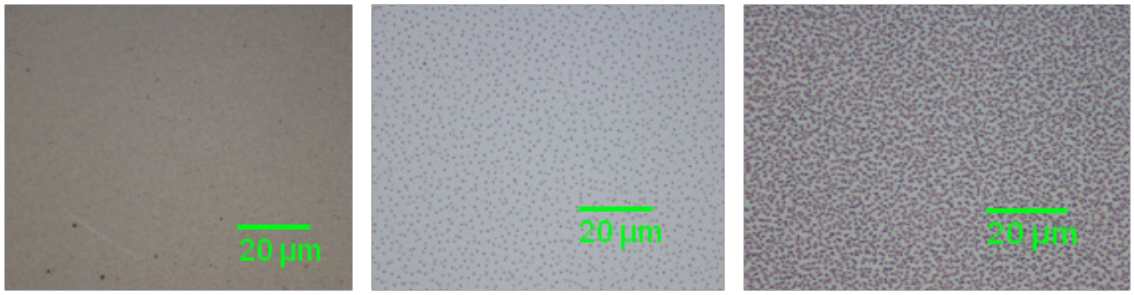

(a) 2.0×10^{-8} Torr (b) 2.5×10^{-8} Torr (c) 3.1×10^{-8} Torr

Figure 2.11 (a)-(c) Droplets density variation as the Bi BEP increases

Figure 2.12 shows a SEM picture of the surface. The brightness contrast of the droplets indicates that they are phase-segregated. The energy-dispersive spectroscopy (EDS) results confirm that the light-color side of the droplets contains much higher Bi content than the dark-color side. This finding agrees with the previous report[49].

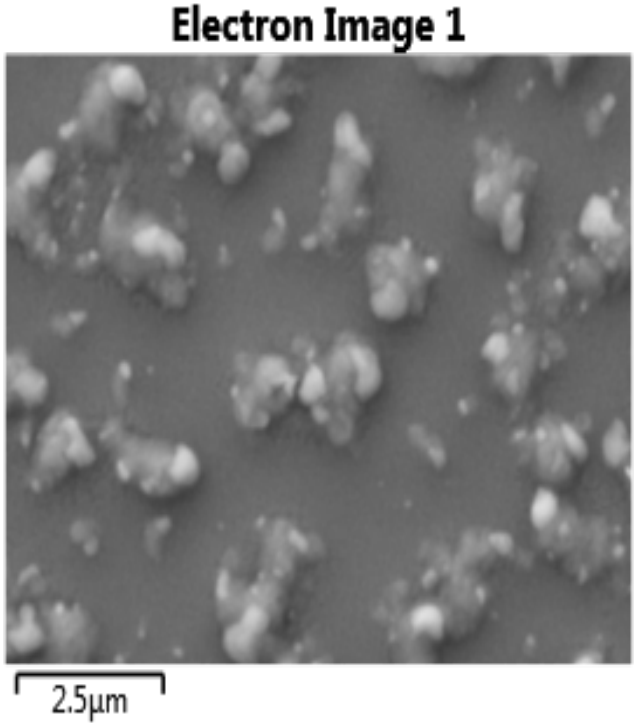

Figure 2.12 SEM picture of InGaBiAs surface

Figure 2.13 shows an enlarged image of the bismuth RBS signal from an InGaBiAs sample with a bismuth concentration gradient. This sample was grown at 300 ˚C when the Bi BEP was 3.1 x 10^{-8} Torr. We have used two fitting lines for the bismuth signal. The blue one is a fitting with a constant bismuth concentration while the red one is a fitting with a linear concentration gradient. It is obvious that the linear concentration fits the experimental data much better than the constant bismuth concentration. As introduced before, a higher channel number in the RBS signal from a single element represents a position that is closer to the surface. We can conclude that there is a Bi concentration gradient increases in the direction from the substrate to the surface, which can be demonstrated by the inclined shape of the Bi signal in the

RBS spectrum. We found that the Bi concentration increased from 1.4% near the buffer layer to 14.4% near the surface. This Bi concentration variation can be fit by a linear Bi concentration increase of 0.0625% Bi/nm pretty well, though it is hard to draw a definite conclusion that the concentration profile is actually linear due to the resolution of RBS measurements. The existence of a Bi concentration gradient suggests that it becomes very difficult to incorporate bismuth into the epilayer since there has been increased bismuth residue sitting on the surface. Consequently, this is close to the highest Bi limit in the given growth conditions. Overall, the Bi incorporation trends of InGaBiAs and that of $GaBi_xAs_{1-x}$ growths agree qualitatively well [24], [50].

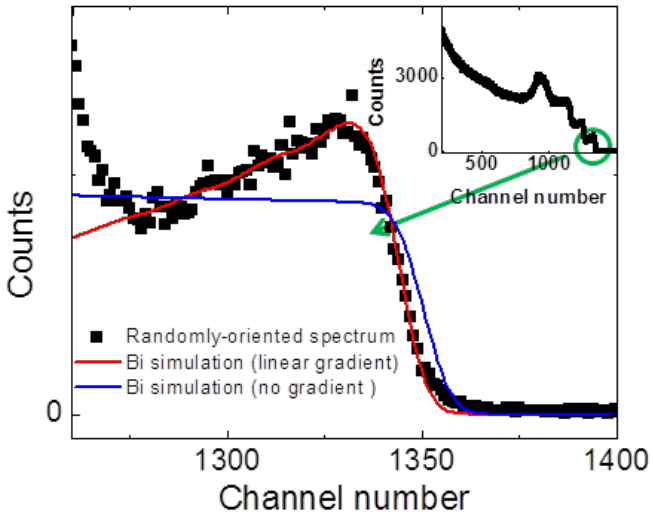

Figure 2.13 The Bi signal in a RBS spectrum of an InGaBiAs sample with linear Bi concentration gradient [42]. (Reproduced with permission from [Y. Zhong, P. B. Dongmo, J. P. Petropoulos, and J. M. O. Zide, "Effects of molecular beam epitaxy growth conditions on composition and optical properties of InxGa1-xBiyAs1-y," Appl. Phys. Lett., 100, 112110, 2012]. Copyright [2012], AIP Publishing LLC. http://dx.doi.org/10.1063/1.3695066)

Other than the surface, we are also interested in the bulk material. It has been reported that Bi clusters will form when the Bi concentration is relatively high [32]. This might be a problem for its optoelectronic applications, but it could be an advantage for its application in thermoelectrics because Bi clusters in the bulk will further bring down the thermal conductivity and improve the figure of merit. Here we studied the composition of InGaBiAs at atomic scale using HAADF-STEM, which is also referred as Z-contrast imaging. It is a special type of STEM equipped with an annular shaped detector. For a conventional detector, when the electron beam hits the sample, the majority of the electron beam will channel along columns of atoms and result in a bright spot in the image. The annular shaped detector will avoid the center beam and just detect the electrons scattered to high angles by the atoms. The number of the scattered electrons to high angles is positively related with the atomic number of the atom, which is the reason why it is called Z-contrast. Like RBS, this technique is particular suitable to detect large elements like bismuth since they will appear much brighter in the image than low atomic number elements. Therefore, through the brightness contrast and software analysis, we can measure the composition at atomic scale.

Figure 2.14 shows a HAADF-STEM image of (110) plane of InGaBiAs. The sample is prepared by thinning it to be around 100-monolayer thick. In this figure, each dot has a dumbbell shape and is composed of two columns of atoms. Each column is about 100-atom thick. Determined by the composition of the substrate InP and the atomic EDS result (indicated in the color inset), the left column is corresponding to Group V elements while the right column is corresponding to Group III elements. The brightness of each dot is the result of the average atomic weight in

each column. The bright region represents the existence of more large elements than the dark region. In the left figure, the brightness variation in the left columns over an area of about 4-5 dots indicates the sign of the existence of bismuth clustering. A definite conclusion needs to be drawn from further atomic EDS analysis on the left column with a thinner sample.

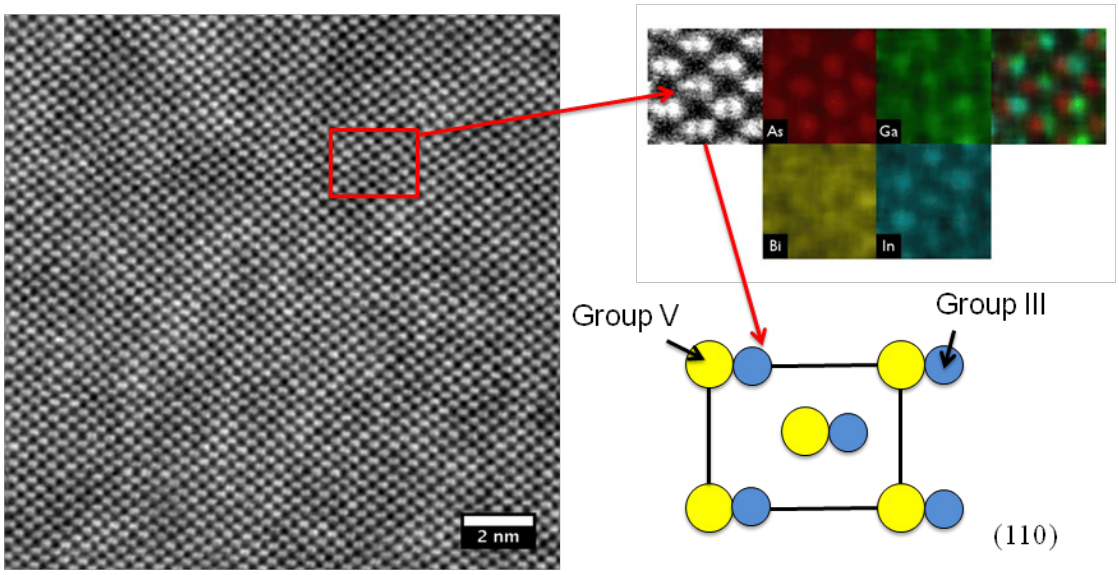

Figure 2.14 HAADF-STEM image of InGaBiAs bulk.

2.5 **Electrical Properties of Unintentionally Doped InGaBiAs**

Electrical properties of unintentionally doped InGaBiAs were characterized using custom-made Hall-effect and four-point probe measurements in the van der Pauw geometry. The samples are prepared by being cut into 1cm x 1cm square. Indium contacts are applied to four corners. A square geometry is chosen over a cloverleaf shape out of convenience.

The mobility and carrier concentration are presented in Figure 2.15. All samples appeared to be n-type with electron concentration ranging from $1x10^{16}$ to

$6x10^{16}$ cm^{-3}, and resistivity varying between 0.02 to 0.3 Ω·cm. InGaBiAs inherits the high mobility from the matrix material, InGaAs, which can be observed by the high mobility of the samples with low bismuth concentration. As a comparison, the mobility of InGaBiAs for 1.5% Bi is around 6000 $cm^2/V/s$, while that of GaBiAs is only at 1370 $cm^2/V/s$ [51]. This contrast is mainly due to the difference between the properties of the matrix materials, InGaAs and GaAs. The mobility of InGaBiAs decreases with the increase of bismuth concentration, as a result of the increased alloy scattering. The carrier concentration increases with bismuth concentration. Both this trend and the n-type conduction can be explained as a result of Bi_{III} antisite defects [52], as opposed to the results from other GaBiAs samples [51]. The scattering in the mobility and the carrier concentration could come from the inconsistency in the material quality.

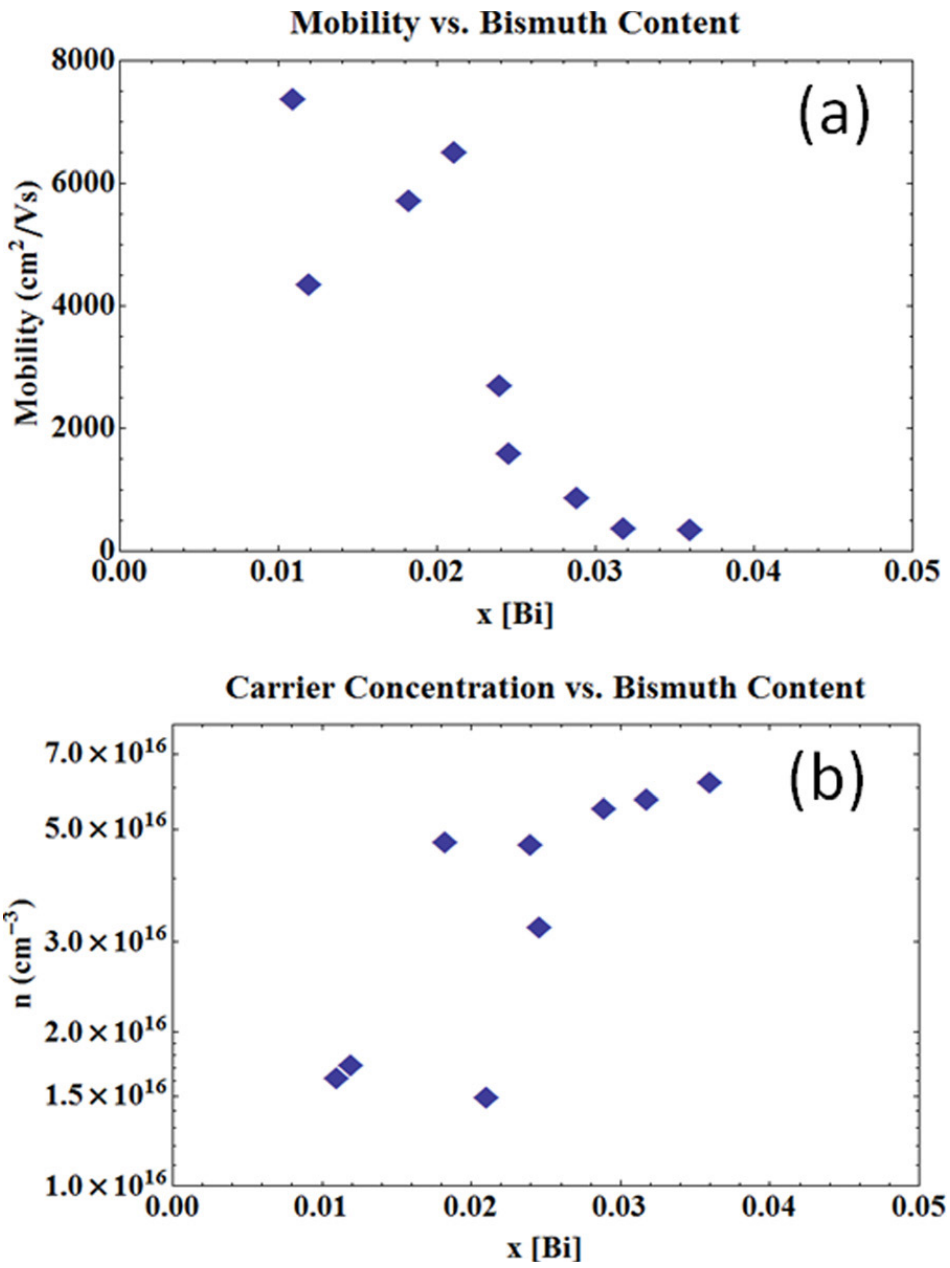

Figure 2.15 Mobility and carrier concentration of unintentionally doped InGaBiAs as a function of bismuth concentration [53]. (Reproduced with permission from [J. P. Petropoulos, Y. Zhong, and J. M. O. Zide, "Optical and electrical characterization of InGaBiAs for use as a mid-infrared optoelectronic material," Appl. Phys. Lett., 99, 031110, 2011]. Copyright [2011], AIP Publishing LLC. http://dx.doi.org/10.1088/0957-4484/22/24/245704)

2.6 **Summary**

In summary, both lattice-mismatched and lattice-matched InGaBiAs on InP substrate have been produced by MBE. It has been demonstrated that low growth temperature and high Bi flux are two keys to increase the Bi concentration. The composition has been studied using HR-XRD and RBS. Each technique has its own advantage in determining the composition. The RSM results have confirmed that all of the InGaBiAs are under compressive strain. In addition, the film has greatly exceeded the theoretical critical thickness without relaxation. The morphology study from optical microscope and SEM indicates that Bi droplets are forming on the surface when the growth temperature or Bi BEP is high. The HAADF-STEM result shows the sign of bismuth clusters in the bulk, but a definite conclusion needs to be drawn from further investigations. The electrical properties of unintentionally doped InGaBiAs revealed that they inherit the high mobility from the matrix material InGaAs, which is another advantage over GaBiAs. Now we understand the key parameters to produce InGaBiAs with high crystalline quality. Chapter 3 will move onto the optical properties of InGaBiAs and its application in optoelectronic devices.

Chapter 3

BAND ANTICROSSING MODEL AND APPLICATION IN MID-INFRARED OPTOELECTRONICS

$In_{0.53}Ga_{0.47}As$ on InP platform is the basis of the current optical communication system due to its 1.55 μm wavelength falling right into the optical fiber low-loss window and its perfect lattice constant that is same as the substrate. Numerous optoelectronic applications such as lasers, LEDs and detectors are produced based on this material system. Currently, some typical near-IR optoelectronic materials based on III-V compounds similar to InGaBiAs include strained InGaAs, GaNAs, and GaBiAs. The state of art strained InGaAs has a cut-off wavelength of 2.5 μm[53]; while GaNAs and GaBiAs have cut-off wavelengths of 1.7 and 1.4 μm, respectively [54][55]. But ideally, we want a material with band gaps covering the wavelength range from 2 to 5 μm because there are a large amount of applications in this range such as environmental air monitoring, plastic and polymer processing and non-invasive diagnosis. InGaBiAs is theoretically predicted to have a cut-off wavelength up to 9 μm while being lattice matched to the InP substrate. Lattice matched material systems are more desirable than strained material systems in optoelectronic devices since they offer better thermal stability, fewer defects and better electrical properties. In addition, InGaBiAs inherits the superior electrical performance of InGaAs, the extremely high electron mobility. This gives it another obvious advantage to make it the material of choice for mid-IR optoelectronic devices.

Section 3.1 provides an introduction to the band anticrossing model (BAC). Section 3.2 discusses the theoretical calculation and experimental measurement of band gaps of InGaBiAs. Sections 3.3 introduces the band structure study (including both the fundamental band gap and the split off band energy Δ_{SO}) of dilute bismuthides. Section 3.4 is the summary of this chapter.

3.1 **Overview of Band Anticrossing Model**

There are many approximations and numerical solutions in calculating the band structures. For example, the k·p theory calculates the energy bands near the fundamental band gap. There has been a simulation considering a 12 band k·p model for dilute bismuthides to predict the band structures[56]. This dissertation will focus on a tight-binding model, which is based on bringing isolated atoms together to form bands, and bands will originate from the bonding happened on atomic levels.

In HMAs, such as dilute nitrides and dilute bismuthides, a widely observed phenomenon is the anomalous fundamental band gap reduction due to the incorporation of the isovalent minority which has large atomic radius and electronegativity differences than the substitution. This band gap decrease originates from the interaction between the extended band of the matrix material and the localized impurity state of the minority. A widely accepted theory is the BAC model, which is predicted within the tight binding approximation framework.

In this BAC model, we assume that impurity atoms are randomly distributed over the group V sites, and the density of impurity atoms is not large enough for them to interact with each other. In addition, the impurity atoms are only weakly coupled to the extended states of the host semiconductor matrix. The eigenvalue problem for impurity atoms interfering with the matrix can then be written as below

$$\begin{vmatrix} E - E_M & V_{MI} \\ V_{MI} & E - E_I \end{vmatrix} = 0 \qquad \text{Equation 3.1}$$

where E_M and E_I are the energies of the conduction/valence band of the matrix material and the impurity level. V_{MI} is the matrix element describing the interaction strength between the extended conduction/valence band and the impurity energy level, which indicates there is a mixing and anticrossing of these states.

The BAC model can be applied to both the conduction band and the valence band depending on whether the impurity level is close to the bottom of the conduction band or the top of the valence band. They are defined as conduction band anticrossing (CBAC) or valence band anticrossing (VBAC) respectively. These two phenomena are widely observed in HMAs. For example, dilute nitrides are well-known for CBAC and dilute bismuthides are a typical material that has VBAC. The key result of the VBAC model is that it predicts a splitting of the conduction/valence band into two subbands E+ and E-, where E+ has a higher energy than E-. The newly generated conduction/valence band will cause an effective reduction of the band gap and produce many interesting new properties.

3.2 Theoretical Calculation and Experimental Measurement of the Fundamental Band Gap of InGaBiAs

Both the experimental results and the theoretical calculations demonstrate an obvious band gap reduction due to the incorporation of bismuth. The fundamental band gaps of InGaBiAs are measured using a PerkinElmer Lambda 750 UV/VIS/NIR spectrophotometer. When a beam of light radiates on the sample, part of the light is absorbed by the sample, part of it is reflected, and the rest is transmitted. Spectrophotometry is a quantitative measurement of the reflection and transmission intensity by continuously adjusting the wavelength of the incidence light and

recording the intensity of the transmitted light. The wavelength range of this spectrometer could be adjusted between 190 nm and 3300 nm because it has duel optical sources and detectors in the visible light range and IR range respectively. Transmission intensity will significantly change once the wavelength of the incident beam matches the band gap of the sample, and the transmission curve will show an edge, which corresponds to an abrupt change in the absorption coefficient.

By measuring the intensity of the transmitted light, we could relate the absorption coefficient and the transmission intensity by Beer's law:

$$\alpha = -\left(\frac{1}{d}\right) \ln\left(I_{norm}\right) \qquad \text{Equation 3.2}$$

where α is the absorption coefficient, I_{norm} is the normalized transmission intensity and d is the thickness of the film. The absorption coefficient depends on the incident wavelength,

$$\alpha = 4\pi n/\lambda \qquad \text{Equation3.3}$$

where n is the imaginary refractive index and λ is the wavelength of the incidence light corresponding to the band gap. In addition,

$$\lambda = 1.24/E_g \qquad \text{Equation3.4}$$

for λ in μm and Eg in eV. As shown by the equations above, the absorption coefficient is directly related with the band gap energies. For a direct band gap material, the absorption coefficient α is related to the light frequency according to the following formula:

$$\alpha = A^*\sqrt{h\nu - E_g}, \text{ with } A^* = \frac{q^2 x_{vc}^2 (2m_r)^{\frac{3}{2}}(2\pi)^3}{\lambda_0 \epsilon_0 \hbar^3 n} \qquad \text{Equation 3.5}$$

Where A^* is a material related constant, h is Plank's constant, Eg is the band gap energy and ν is the incident photon's frequency. In the equation of constant A^*,

$m_r = \frac{m_h^* m_e^*}{m_h^* + m_e^*}$, m_h^* and m_e^* are corresponding to the effective masses of the hole and electron respectively, q is the electron charge, n is the real index of refraction, ϵ_0 is the vacuum permittivity, and x_{vc} is a "matrix element" with units of length and typical value the same order of magnitude as the lattice constant.

From the measured transmission intensity, we can calculate the absorption coefficient α. Then we can plot the absorption coefficient α^2 as a function of the incident light energy, as shown in Figure 3.1. The abrupt edge in α is corresponding to the band gap energy of the material. By extending the linearly raising region of α^2curve down to the x-axis, we can get the band gap information from the intercept.

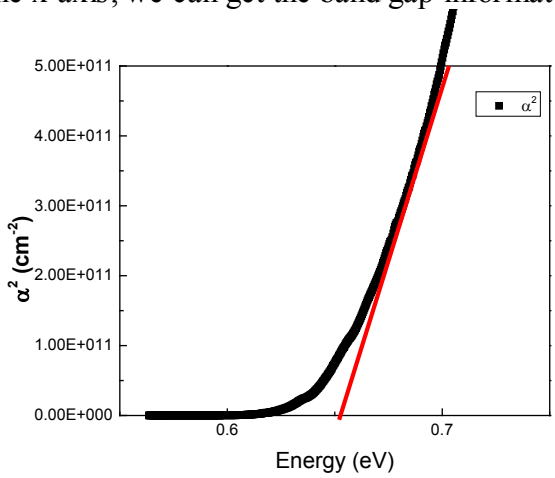

Figure 3.1 Example of determining the band gap energy from the square of the absorption coefficient

The theoretical values are calculated using a BAC modelas described in Section 3.1[53]. In our case, the impurity level is bismuth and the matrix energy is the valence band of InGaAs. The two solutions for Equation 3.1 can be given as

$$E_{\pm} = (E_B + E_M \pm \sqrt{(E_B - E_M)^2 + 4V_{MB}^2})/2 \qquad \text{Equation 3.6}$$

E_M is the valence band energy of InGaAs as a function of the composition, which is given by

$$E_M = 0.356 + 0.7x + 0.4x^2 \qquad \text{Equation 3.7}$$

where x is the gallium concentration [57]. E_B is assumed to stay 0.4 eV [58] below the top of the valence band of InGaAs and will not be affected by the composition variation. The V_{MB} is acquired from the fitting of the experimental data.

Figure 3.2 shows the experimental measurements (dot, square and triangle marks) as well as the simulation results (solid, dash and dot lines) of the lattice mismatched InGaBiAs with different In/Ga ratios in varied colors. As is shown in the HR-XRD and RBS measurements, there are small variations in the In/Ga ratio which will affect the actual band gap. We exclude this effect by differentiating them into three groups based on their different In/Ga ratio, and samples with the same In/Ga ratio are drawn in the same color. As expected, the incorporation of Bi leads to a reduction in band gap. At low bismuth concentration, the band gap decreases approximately linearly at a rate of ~56meV/Bi%, which is a moderate rate compared to 88meV/Bi% for GaBiAs [33] and 12 meV/In% for InGaAs [34]. The long wavelength limit of InGaBiAs from experiments thus far is 2755 nm, corresponding to an average bismuth concentration of 6.75%. This is the longest wavelength achieved in this material system up to date. The inset shows the simulation (purple line and red dots) and experimental results (purple diamonds) of the nominally lattice-matched samples. The purple line is a calculation with compositions that are perfectly lattice-matched to the substrate, and the red dots represent the calculation with the actual composition of our nominally lattice-matched samples. The red dots fit the purple diamonds better than the purple line which indicates that the errors mainly come from

the composition variation. We have not yet taken the strain effect into account due to the shortage of information on the effects of strain in these materials, though the effect is clearly important given the strain and relaxation results from RSM. By comparing the experimental results and simulations, we can see that they agree reasonably well with each other; the scatter in the data could result from the presence of bismuth clusters which will affect the effective band gap in an anomalous way[59], [60]. In related work, it has been shown that the band gap narrowing occurs mainly in the valence band [28]. This will give us some new advantages in band engineering and device design because now we can tune the conduction band and the valence band individually.

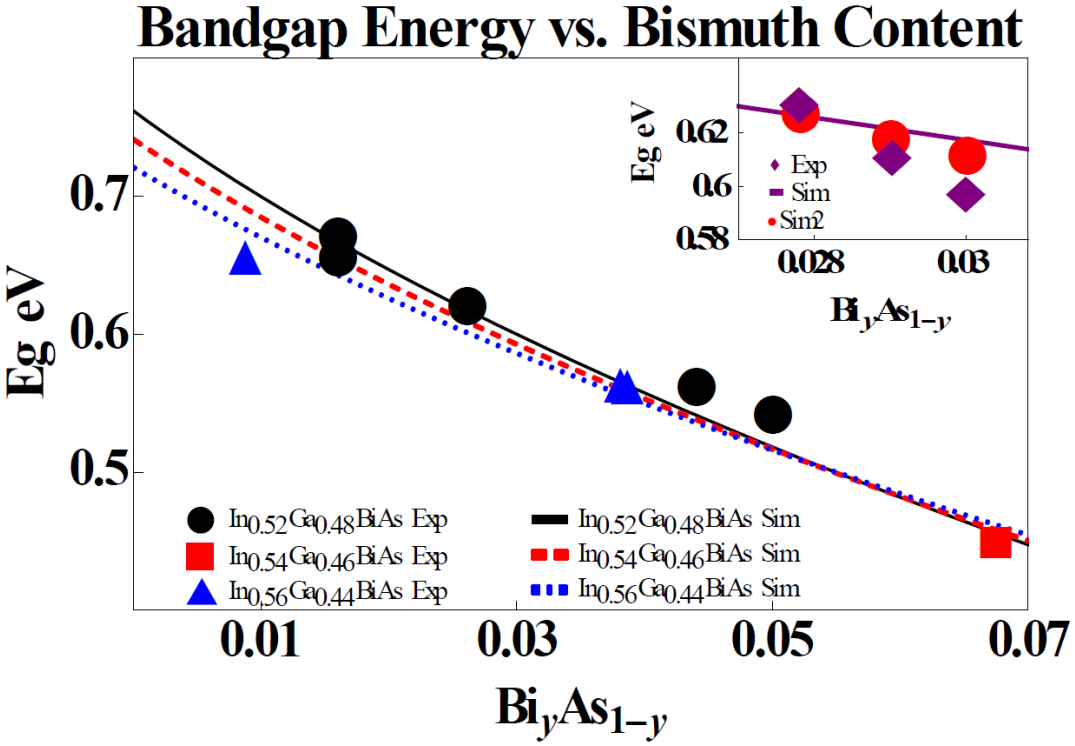

Figure 3.2 Band gap energies of both lattice mismatched (main area) and nominally lattice matched InGaBiAs (inset) as a function of the bismuth concentration based on various In/Ga ratio [42]. (Reproduced with permission from [Y. Zhong, P. B. Dongmo, J. P. Petropoulos, and J. M. O. Zide, "Effects of molecular beam epitaxy growth conditions on composition and optical properties of InxGa1-xBiyAs1-y," Appl. Phys. Lett., 100, 112110, 2012]. Copyright [2012], AIP Publishing LLC. http://dx.doi.org/10.1063/1.3695066)

Figure 3.3 is a contour plot of the fundamental band gap of InGaBiAs based on all the possible compositions. The x axis represents the Bi concentration changes from 0% to 100%; accordingly, As concentration varies from 100% to 0%. Similarly, y axis shows the In concentration changes from 0% to 100% from bottom to top. It is worth pointing out that GaBi does not exist in nature, and there are still debates about the existence of InBi. The limits of VBAC model can be observed in this contour plot in samples with high Bi concentration. As mentioned previously, the interaction strength is only valid in the VBAC model when Bi concentration is low and wavefunctions of two Bi atoms are not overlapping with each other. If we fix the bismuth concentration and gradually increase the indium concentration, we will find the band gaps of InGaBiAs first decrease and then increase when the Bi concentration is above 8%. This is because the experimentally extracted interaction strength is only valid for low bismuth concentration samples, and it needs correction from advanced levels for high bismuth concentration samples. In addition, the fundamental band gap of high Bi concentration samples starts to deviate from the prediction of the VBAC model because they start to form Bi clusters. So this VBAC model is only valid to predict the fundamental band gap of InGaBiAs with low Bi concentration. Setting the real boundaries of the validity of this model will require further empirical supports.

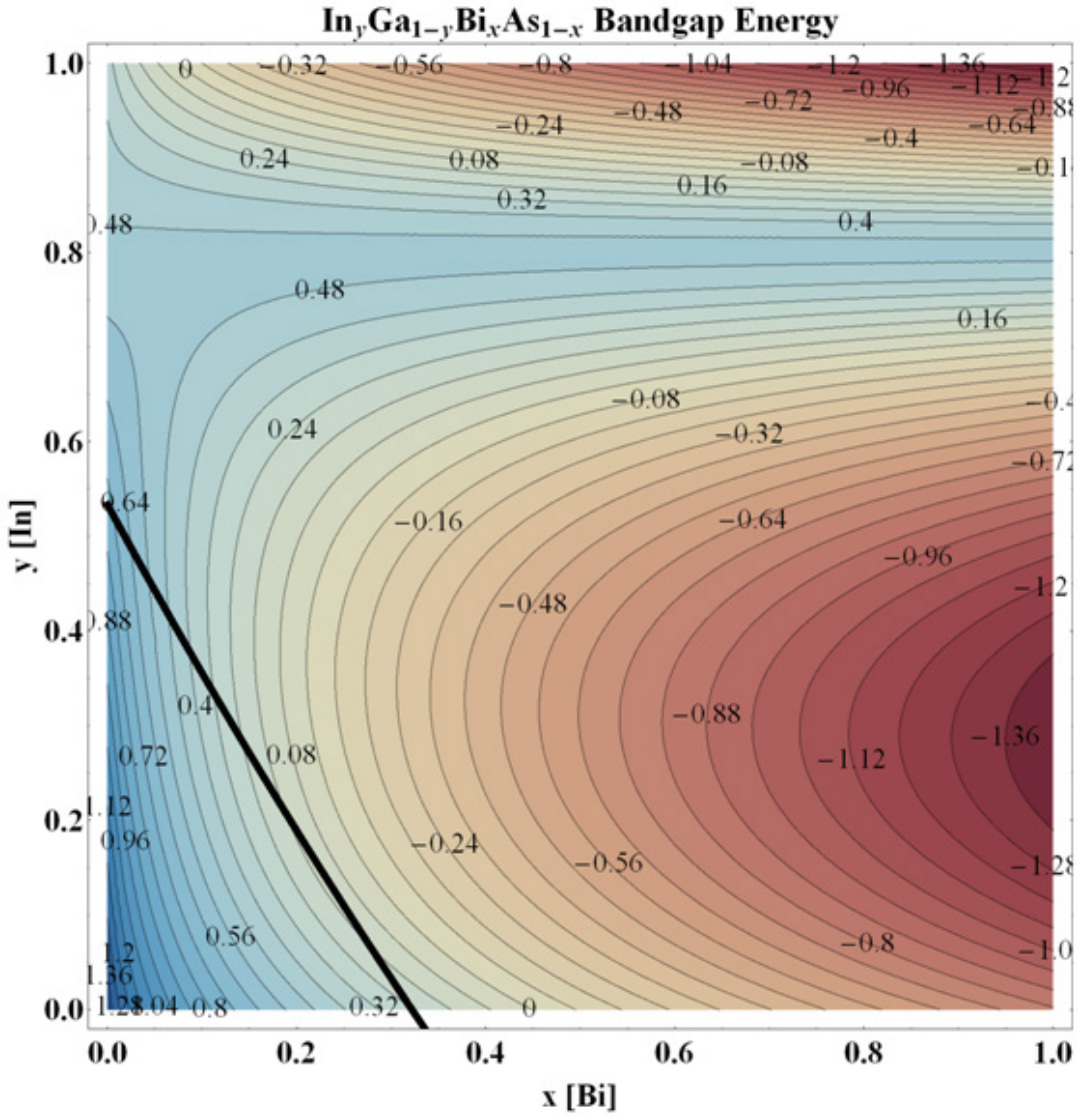

Figure 3.3 Contour plot of the calculated band gap energies of InGaBiAs versus composition. The numbers marked on the curve represent the band gap energy. X axis and y axis are corresponding to bismuth and indium concentration respectively. The black line in the center represents the band gap of InGaBiAs when it is lattice matched to the InP substrate.

Figure 3.4 shows the cut-off wavelength (converted from the fundamental band gap) of InGaBiAs as a function of Bi concentration when InGaBiAs is lattice-matched

to the InP substrate. This indicates that we could produce InGaBiAs with a cut-off wavelength up to 9 μm with around 22% Bi with zero strain. The longest cut-off wavelength of our strained InGaBiAs achieved so far is 2.7 μm and that of our lattice-matched InGaBiAs is 2.1 μm. Furthermore, there is still room to achieve higher Bi concentration and push the cut-off wavelength into longer wavelength range. Therefore, we can conclude that InGaBiAs is a promising new candidate for mid-IR optoelectronic materials.

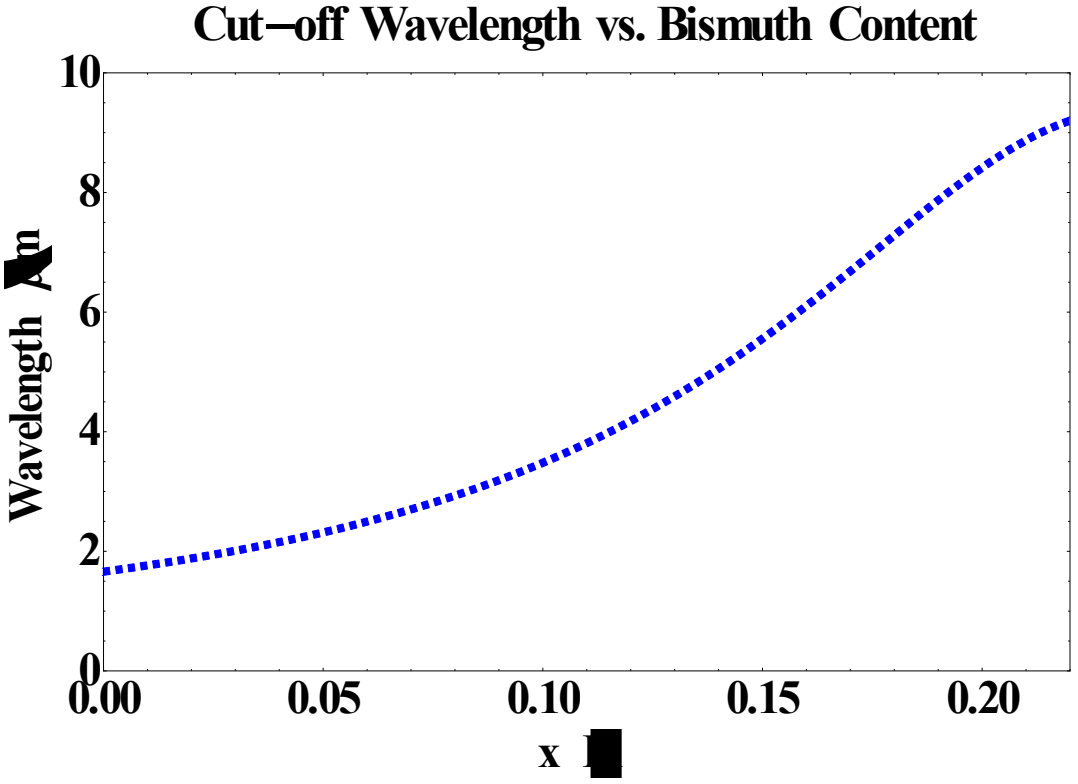

Figure 3.4 Cut-off wavelength of nominally lattice-matched InGaBiAs as a function of bismuth concentration

3.3 Band Structure Study of Dilute Bismuthides

In Section 3.1, we have asked this question that whether VBAC generates a full continuous band or a large amount of localized states? Here we will introduce

onepowerful tool to study the band structure of dilute bismuthides: contactless electroreflectance (CER). This part of dissertation will be largely based on Kudrawiec's work[61].

Dilute bismuthides are potentially good candidates for near IR and mid IR light emitting devices because the incorporation of bismuth can result in a large reduction of the fundamental band gap and an increase of the spin-orbit splitting energy Δ_{SO}. When we keep increasing the bismuth concentration, the spin-orbit splitting energy Δ_{SO}will become larger than the fundamental band gap, and CHSH (Conduction band electron/ Heavy hole/ Spin-orbit split-off band/ Heavy hole) Auger will be suppressed. Figure 3.5 listed two common Auger processes-CHCC (Conduction band/ Heavy hole band/Conduction band/ Conduction band)Auger and CHSH Auger. When an electron in the conduction band recombines with a hole in the heavy hole band, it will give off its energy and momentum. If the energy and momentum are given to an electron in the conduction band which is lifted to a higher conduction band state, this process is defined as CHCC Auger; while if the energy and momentum are used to promote a hole in the split-off band to an empty heavy hole state, it is defined as CHSH Auger .

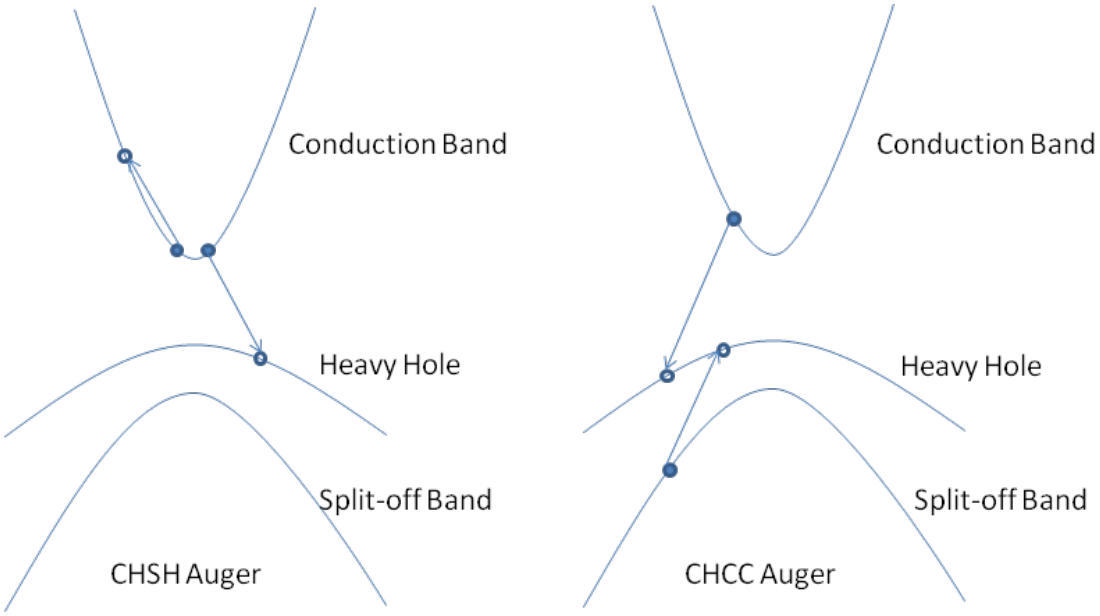

Figure 3.5 Schematic diagram of CHSH and CHCC Auger recombination processes. The electrons and holes are represented by black circles and white circles respectively.

It has been experimentally demonstrated that Auger recombination and inter-valence band absorption (IVBA) are the two primary reasons that lead to high threshold current and high optical cavity losses at elevated temperatures in IR lasers[16]. One effective method to suppress CHSH Auger and IVBA is to make the spin-orbit splitting energy Δ_{SO} exceed the fundamental band gap in these materials. The suppression of CHSH Auger process is very important in infrared optoelectronic devices because it can greatly improve the optical-electrical signal conversion efficiency for small band gap materials. It has already been predicted that the fundamental band gap will become smaller while the spin-orbit splitting energy Δ_{SO}will increase due to the increase of bismuth concentration in GaBiAs [62].Very

similar effects are expected for InGaBiAs as well. Therefore, we need to study the band structures of InGaBiAs.

One powerful tool to study the interband transitions is named CER. It is a noninvasive technique to study the optical transitions in semiconductor thin films, low dimensional structures and real devices. The principle of this technique is that it measures the derivative of the reflectance spectrum with respect to the modulated electrical field. There are two modes to add the modulated electrical fields: contact mode and noncontact mode. Contact mode will involve the deposition of either a Schottky barrier or a semiconductor/electrolyte junction which is complicated and destructive. The contactless mode is realized by using a capacitor system with one electrode semi−transparent for light [63]. The reflectivity of the sample will be periodically modulated by the built-in electric field from the capacitor system. The measured reflectivity will produce sharp derivative-like spectral features at photon energies which correspond to interband transitions. Figure 3.6 compares the experimental setups of different kinds of electroreflectance (ER) and photoreflectance (PR). Using line-shape fitting will allow direct analysis of the fundamental band gap, the band gap between conduction band and the spin-orbit split-off band, and some broadening parameters, even at room temperature.

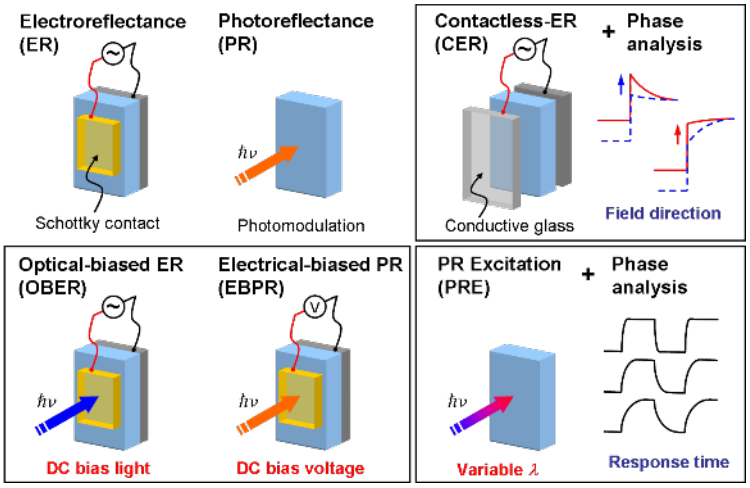

Figure 3.6 Experimental setups of different kinds of electroreflectance (ER) and photoreflectance (PR).(http://www.matsuoka-lab.imr.tohoku.ac.jp/?katayama%2Fresearch%2Fmodspec%2F02_experiment)

Kudrawiec et al. first report their experimental measurements of the E_0 and Δ_{SO} transitions for InGaBiAs by CER [61]. Similar to the results of GaBiAs, the CER results have unambiguously confirmed the red-shift of the fundamental band gap Eg due to the bismuth concentration increase. But the $E_0+\Delta_{SO}$ transitions remain unchanged in spite of the variation of bismuth concentration within the experimental error, which means that the Δ_{SO} transition energy increases at the same rate as theE_0 transition reduces. The extraction result from CER measurements is shown in Figure 3.7. The fact that the fundamental band gap and the spin-orbit splitting energy Δ_{SO} changes at the same magnitude indicates a shift of only the heavy/light hole band towards the conduction band without any change of the conduction band or spin-orbit splitting band position.

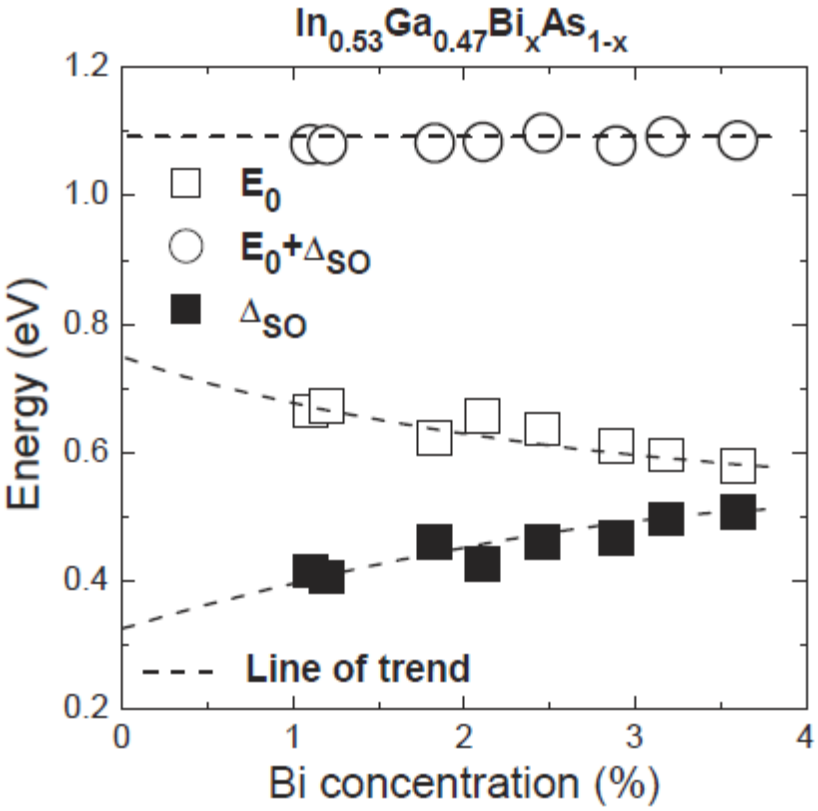

Figure 3.7 Interband transition energy of InGaBiAs as a function of bismuth concentration extracted from CER measurements [61]. (Reproduced with permission from [R. Kudrawiec, J. Kopaczek, J. Misiewicz, J. P. Petropoulos, Y. Zhong, and J. M. O. Zide, "Contactless electroreflectance study of E_0 and $E_0 + \Delta_{SO}$ transitions in $In_{0.53}Ga_{0.47}Bi_xAs_{1-x}$ alloys," Appl. Phys. Lett., 99, 251906, 2011]. Copyright [2011], AIP Publishing LLC. http://dx.doi.org/10.1063/1.3669703)

3.4 **Summary**

In this chapter, we first introduced the BAC model and exhibited the experimental demonstrations of the validity of BAC theory. Then we showed how to apply this BAC model to InGaBiAs to calculate the fundamental band gap. We compared the calculation results with the experimental measurements, which are in good agreement. Finally, we showed some band structure studies from CER results

which indicate that the increase of bismuth incorporation purely raises the valence band up without affecting the positions of the conduction band and spin-orbit splitting band. In summary, BAC is an empirical correct model to explain the anomalous band gap narrowing in dilute bismuthides and is useful for band engineering simulation and future device design.

Chapter 4

DEGENERATELY DOPED INGABIAS:SI AS A NEW INFRARED TRANSPARENT CONTACT MATERIAL

In the previous chapter, we discussed using InGaBiAs as a mid-IR optoelectronic material. In this chapter, we will move onto its next application, a transparent contact material. This is an application we did not expect in the first place and discovered along the way. First, we noticed that our InGaBiAs:Si samples could be doped to very high levels before showing the sign of doping saturation, which means dopants will become electrically inactive either by sitting at interstitial sites or switching to opposite sites to cancel the previous doping effect. Some of the degenerately doped InGaBiAs:Si samples exhibit very high conductivity due to their very high doping levels and fairly high mobility at these high doping levels. The highest conductivity among these samples reaches 4850 $S \cdot cm^{-1}$, which is one half of the conductivity of mercury and one third of stainless steel, both are good conductors. It occurs to us that they could be used as contact materials [64]. Additionally, their effective band gaps will be greatly increased since they are degenerately doped and the bottom states of the conduction band are filled, which make them transparent above certain wavelength. Therefore, degenerately doped InGaBiAs:Si could be utilized as a new transparent contact material.

Section 4.1 will provide a brief introduction of transparent contact materials. Section 4.2 will introduce the background information of InGaBiAs:Si. Section 4.3 will describe the experimental measurements in detail. Section 4.4 will discuss the

transmittance results and compare InGaBiAs:Si and ITO in terms of transparency and conductivity. Section 4.5 is the summary of this chapter.

4.1 Overview of Transparent Contact Materials

Nowadays, there have been increased desires for transparent contact materials from solar cells, touch screens, LCDs and detectors. Take solar cells for example, a transparent contact will allow high portion of the incident light be absorbed by the p-n junction and get converted to electrical energy, which will greatly improve the overall solar cell efficiency.

Transparent conductive oxides (TCOs) are the most extensively investigated transparent electrode (TE) materials. They are usually heavily doped wide band gap semiconductors. The discovery of TCOs as contact materials was made by accident in 1930s at Corning laboratories (US Patent # 2118795). Indium tin oxide (ITO), as the most widely used TCO, was discovered in the 1940s as the extension of the previous TCO work (US Patent # 2564704). ITO has high optical transparency within the visible light range and the near IR range and is highly conductive[65], which makes it the dominant material in transparent contact materials market. However, ITO becomes highly reflective for incident light with wavelength above 1.5 μm due to its plasma frequency in the near IR [66] (similar to other TCOs), which makes it impractical for a transparent contact material in the IR range. In addition, the deposition of ITO films can be complicated and usually requires post deposition treatment such as annealing [67].

Mid-IR optoelectronic devices operating in the 1.5-10 μm range offer a broad range of functionality for a variety of applications. When molecules change their dipole moments, they will emit or absorb light signals in the IR range, which are

commonly used for environmental air monitoring. The atmospheric transmission window at 3 to 5 μm is widely used for guided missiles by homing onto the infrared signature of the target engine exhaust. There are many other applications in this wavelength range such as polymer and plastic processing, noninvasive medical diagnosis, remote sensing and free space communication. However, the most widely used transparent contact material for IR optoelectronic devices is still ITO, which is highly reflective in this wavelength range and severely hinders the optoelectronic signal conversion efficiency.

Alternative options for IR TE materials include carbon nanotube (CNT) films [68], [69], ultrathin metal films [67], graphene films [70], metal nanostructures in the form of metal nanogrids/ nanowires/ nanofibers [71], [72], and highly conductive polymers [73]. The IR transparent window (transmittance over 80%) for CNT films is very long (1-22μm). However, the resistivity of CNT is relatively high, at around 200 Ω/□ [69] due to the loose overlap between single CNTs. Ultrathin metal films have attracted much attention recently because metal at ordinary thickness are naturally very good conductors. However, the performance of ultrathin metal films as transparent contact materials is extremely sensitive to thickness. A very thin metal film will have a good transmittance, but the resistance will be consequently high. When the thickness is increased, the resistance will be greatly reduced, but the transmittance will be severely decreased as well. For example, a 2 nm Ni film has a mean transmittance above 80% in the IR range from 2.5 to 25 μm but a resistance of around 1000 Ω/□; while the resistance of a 10 nm Ni film is immediately reduced to 30 Ω/□ at the price that the mean transmittance falls to 40% [67]. According to the growth stages of thin metal films, irregular metal islands will first form, but they will

not touch each other until the thickness is above 10 nm; a continuous metal film will not form until the thickness is above 20 nm[74]. Accordingly, it seems to be a big challenge to make ultrathin metal film with thickness below 10 nm while maintaining high conductivity. Metal nanostructures could achieve high transparency as well as good electrical properties. However, the process of building metal grids or meshes will involve lithography, which remains complicated, expensive and impractical for large scale production[71], [72]. Graphene and conductive polymers offer ideal mechanical properties for flexible electronics, but both the transparency and conductivity of these TEs are inferior to most of the aforementioned technologies [70], [72]. Figure 4.1 lists the transparent contact materials discussed above; the length of the color bar represents the transparent window of each material, and the transparent window is defined as the transmittance over 80%. The y axis compares the sheet resistance of each material. A good transparent contact material should have a long transparent window and a low sheet resistance.

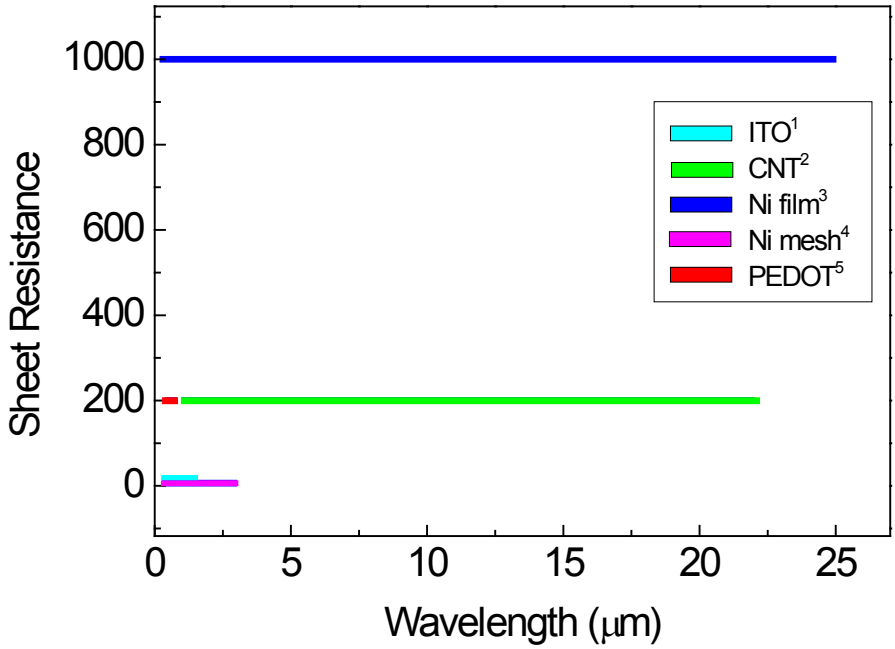

Figure 4.1 Comparison of some current popular IR transparent contact materials in terms of transparent window and sheet resistance.

4.2 **Background of Degenerately Doped InGaBiAs:Si**

In the semiconductor industry, researchers always intentionally introduce impurities into intrinsic semiconductor to generate extra free carriers and modify their electrical properties. There are two types of doping: n type (if the dopants are donating extra electrons to the bulk) and p type (if the dopants are donating extra holes to the bulk). For example, doping silicon into III-V compounds will generally produce n-type doping. Lightly and moderately doped semiconductors are referred to as extrinsic semiconductors, while degenerately doped semiconductors are doped to a high level when the Fermi level is above the bottom of the conduction band. Usually, degenerately doped semiconductors act like conductors.

There has been significant interest in the use of highly doped semiconductors for mid-IR optoelectronic applications recently. It has been proven that at mid-IR frequencies, a flat layer of heavily doped InAsSb has a vanishingly small dielectric permittivity, also known as epsilon-near-zero, and can couple light to subwavelength objects without complicated structures such as gratings [75]. Recent work has also shown that highly doped InAs disc arrays are able to support localized surface plasmon modes which can be integrated into sensing system to increase the resonance between the incident radiation and molecular absorption [75],[76].

In the previous section, we have demonstrated InGaBiAs as a new material for mid-IR optoelectronics due to its adjustable band gap fitting in the mid-IR range [42],[53]. Here we report degenerately doped InGaBiAs:Si as a novel TE candidate in the same range. As mentioned in the previous section, InGaBiAs:Si is able to achieve very high doping concentration without showing the sign of doping saturation. Figure 4.2 shows the carrier concentration of InGaBiAs:Si as a function of Si cell temperature. Before doping saturation, there is a linear doping regime which means the carrier concentration exponentially increases with Si cell temperatures and the doping coefficient is 1. The line in the middle is a typical doping saturation line for Si doped III-V compounds. From the figure, we can see that the linear doping regime for InGaBiAs extends further into the high carrier concentration range after the typical saturation line. The reason that InGaBiAs:Si can be doped to such a high level is mainly due to special growth condition, a low growth temperature. The sticking coefficient of Si atoms is higher at low growth temperature, which indicates that more Si atoms will stay on the surface to get incorporated. Therefore, high carrier concentrations are observed in samples grown at low-temperatures is well-established

in epitaxial growths[78].The second reason that InGaBiAs:Si could be doped at such a high level is because bismuth can provide a large density of step edges at a micro scale, which could provide more sticking sites for Si atoms [79].

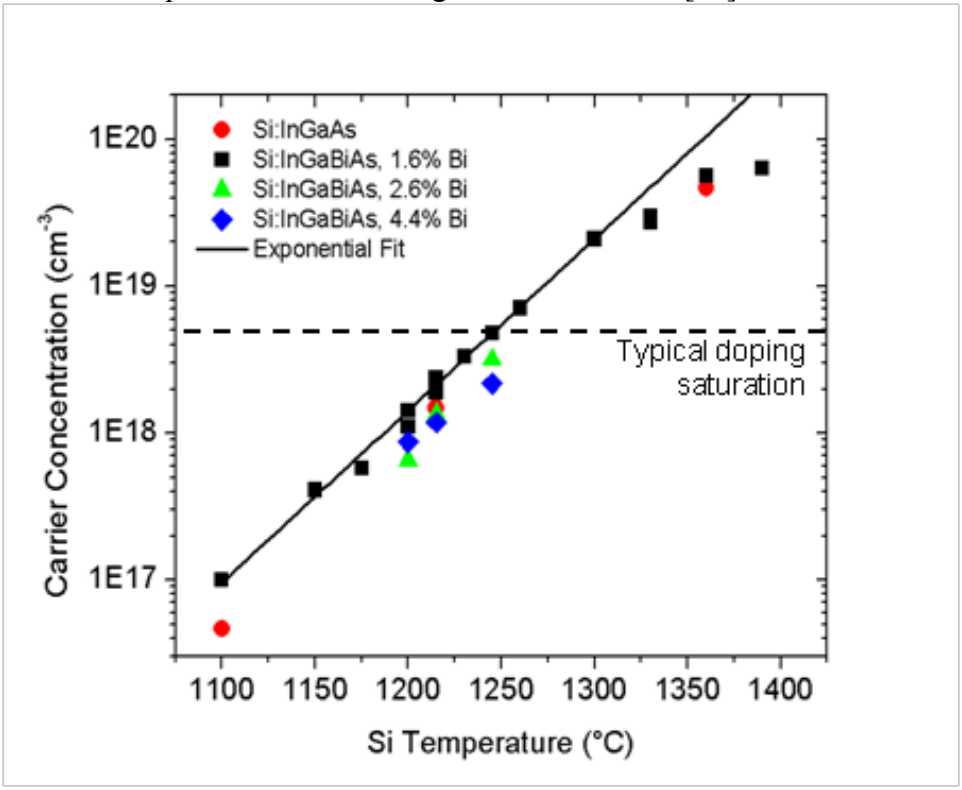

Figure 4.2 Carrier concentration of InGaBiAs:Si samples as a function of Si cell temperatures. The black line in the middle represent the typical saturation doping line of Si doped III-V compounds [79]. (Reproduced with permission from [P. Dongmo, Y. Zhong, P. Attia, C. Bomberger, R. Cheaito, J. F. Ihlefeld, P. E. Hopkins, and J. Zide, "Enhanced room temperature electronic and thermoelectric properties of the dilute bismuthide InGaBiAs," J. Appl. Phys., 112, 093710, 2012.]. Copyright [2012], AIP Publishing LLC. http://dx.doi.org/10.1063/1.4761996)

The mobility of InGaBiAs:Si samples is relatively high mainly due to the nature of the matrix material InGaAs. Generally, the mobility of doped samples will decrease when the carrier concentration increases. This is because the addition of

impurities will lead to enhanced scatterings as shown in Figure 4.3. By comparing InGaAs:Si and InGaBiAs:Si, we will notice that at the same doping level, the latter has slightly better mobility. This is because a small amount of bismuth can behave as a surfactant, improving the crystalline quality of the film, which keeps the mobility relatively high even at a low growth temperature.

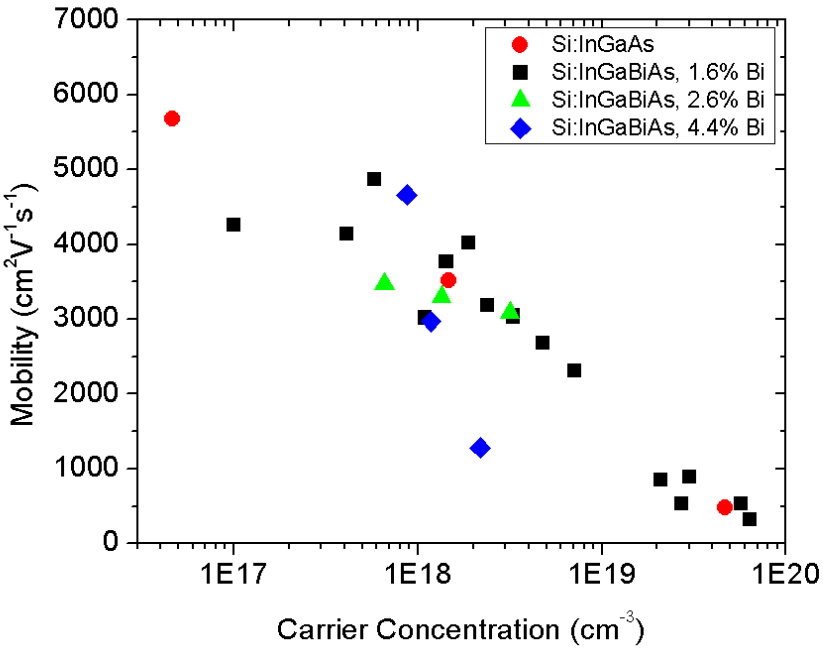

Figure 4.3 Mobility of InGaBiAs:Si as a function of carrier concentration [79]. (Reproduced with permission from [P. Dongmo, Y. Zhong, P. Attia, C. Bomberger, R. Cheaito, J. F. Ihlefeld, P. E. Hopkins, and J. Zide, "Enhanced room temperature electronic and thermoelectric properties of the dilute bismuthide InGaBiAs," J. Appl. Phys., 112, 093710, 2012.]. Copyright [2012], AIP Publishing LLC. http://dx.doi.org/10.1063/1.4761996)

As a result, InGaBiAs:Si has very high electrical conductivity as shown in Figure 4.4. The highest conductivity reaches 4850 $S \cdot cm^{-1}$ [79], which is 1/2 of mercury

and 1/3 of stainless steel [64]; both being good conductors. Similar materials include heavily-doped InGaAs:Si and InP:Si. Although electrical properties of them have been reported before, optical properties were not included[78], [80]. In our own work, InGaAs cannot be doped as high as InGaBiAs, and the mobility of it is lower [79].

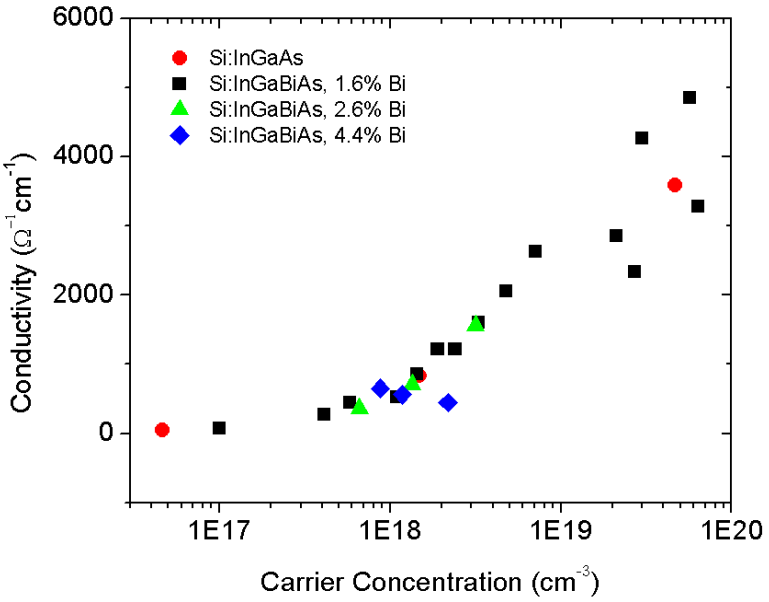

Figure 4.4 Conductivity of InGaBiAs:Si as a function of carrier concentration [79]. (Reproduced with permission from [P. Dongmo, Y. Zhong, P. Attia, C. Bomberger, R. Cheaito, J. F. Ihlefeld, P. E. Hopkins, and J. Zide, "Enhanced room temperature electronic and thermoelectric properties of the dilute bismuthide InGaBiAs," J. Appl. Phys., 112, 093710, 2012.]. Copyright [2012], AIP Publishing LLC. http://dx.doi.org/10.1063/1.4761996)

Degenerately doped InGaBiAs:Si exhibits high transparency in the IR region (1.3 to 12.5 µm), with the exact transparent windows determined by the carrier concentration. The carrier concentrations will determine the starting point of the transparent window in the short wavelength end due to the effective band gap which is

related with the doping level. They will also determine the end point of the transparent window in the long wavelength end due to the plasma frequency. InGaBiAs can be produced as a single crystal and grown under ultra high vacuum conditions with few impurities. Meanwhile, it could be grown lattice-matched to the underlying InP based optoelectronic device. The combination of large electrical conductivity and high transparency in the mid-IR region makes InGaBiAs:Si a promising new IR TE material.

4.3 Sample Preparation and Transmission Measurement

InGaBiAs:Si samples were grown on double side polished InP:Fe substrates by MBE. After the desorption of the native oxide on the substrate surface, a 90 nm $In_{0.52}Ga_{0.48}As$ buffer layer was first deposited to provide a clean epitaxial surface. Then a 500 nm $In_{0.52}Ga_{0.48}Bi_{0.016}As_{0.984}$:Si film is deposited onto the buffer layer. Both the buffer layer and the film are grown at relatively low growth temperature of approximately 300 °C. Varying the temperature of the Si cell can control the carrier concentrations, while the fluxes of the other cells were kept constant. More detailed descriptions of growth conditions have been reported previously [42], [53], [79]. As a comparison, a 300 nm ITO film was deposited onto double side polished Si substrates and glass substrates respectively by sputtering a commercially available ITO target. The purpose of two different substrates is for the transmission measurement in the visible light and in the mid IR region. During the production of ITO, the carrier concentration can be tuned by adjusting the oxygen flow, but the mobility will not be affected and remains relatively constant for carrier concentrations between 10^{18} and 10^{20} cm^{-3}. The ITO sample we chose has superior electrical performance compared to other ITOs in terms of conductivity[81]. While the range of the transparent window of

ITO might be enlarged by reducing the carrier concentration, the electrical conductivity would suffer as a consequence.

Transmission spectra from 2 to 12 μm were measured at room temperature using a Thermo-Nicolet Nexus 670 Fourier transform infrared (FTIR) at a resolution of 4cm^{-1} per line with 128 average scans. In the experimental transmission settings, we used a deuterated triglycine sulfate (DTGS) detector. Transmission measurements of the thin films were all normalized to the InP substrate. The transmission spectra from 1 to 2 μm were measured using a Perkin-Elmer Lambda-750 UV-visible-IR spectrophotometer equipped with a Peltier-cooled PbS detector because of the poor sensitivity of the DTGS detector in this wavelength range. Due to the design of the aforementioned equipments, which lacks the ability to measure the reflectivity, reflection spectra were collected using a Bruker IRII infrared microscope coupled to a V80V FTIR spectrometery and normalized to the reflection from a flat gold surface. The electrical measurements were carried at room temperature using a custom-built Hall effect system in the van der Pauw configuration.

4.4 **Transmission Spectrum and Burstein-Moss Model**

The transmission and reflection spectra of InGaBiAs:Si films and ITO film over the wavelength 1 to 12 μm are shown in Figure 4.5 (a) and (b) respectively. The different color represents different carrier concentrations. Figure 4.5 (a) includes many different types of transmission spectra due to the limit of each equipment. In Figure 4.5 (a), transmission spectra in the wavelength range from 1 to 2 μm were measured by spectrophotometer (dashed lines), above 2 μm were measured by FTIR (solid lines). These spectra are not directly measured results and have already been subtracted the effect from the substrate. The calculations for the transmittance are

indicated in dashed dot lines. In Figure 4.5 (b), the measured reflectance spectra normalized to a gold surface are indicated by solid lines, and the transmittance spectra calculated from an experimentally extracted complex dielectric constant are noted by dashed lines. The details about the calculation of transmittance spectra are included in Section 4.5.

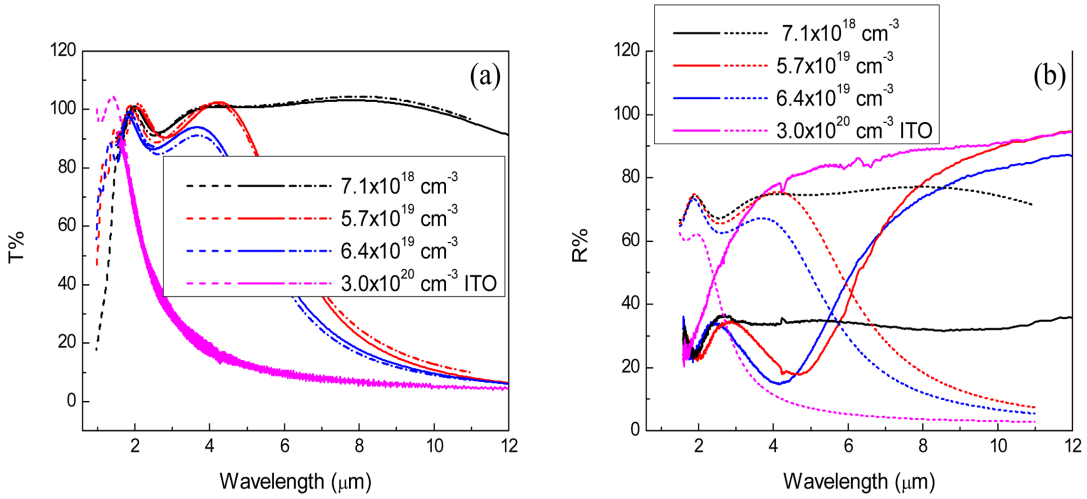

Figure 4.5 (a) and (b) show transmittance and reflectance spectra of InGaBiAs:Si films and the ITO film as a function of wavelength. The inset indicates the carrier concentration of each film [82].

As clearly shown in Figure 4.5 (a), the transmittance of the ITO film quickly falls at wavelengths longer than 1.5 μm; while InGaBiAs:Si remain highly transparent in the mid-IR or even the long-IR range. Figure4.5 (b) confirms that ITO becomes highly reflective above 1.5 μm while InGaBiAs:Si have constant reflectance around 30% for a wide range of mid-IR wavelengths. The transmission and reflection spectra confirm that our samples are not only highly transmitted but also have low losses. Therefore, in terms of transparency, InGaBiAs:Si films are better candidates for mid-IR contact materials than ITO. In Figure 4.5 (a), at some wavelengths, transmission

spectra (dashed and solid lines) are slightly over 100%. This is an expected result when we normalize the transmittance to the substrate. The physics behind it is that at certain wavelengths, the InGaBiAs:Si layers are acting like anti-reflective coatings, improving transmission over the bare InP wafer.

In Figure 4.5 (a), we can see there are distinct transparent windows for each material. The starting and the end point of the transparent window at the short wavelength and long wavelength end are determined by the effective band gap and the plasma frequency respectively. At the long wavelength end, the cutoff wavelength of the high transmittance region blue shifts with the carrier concentration increase. This cut-off wavelength is determined by the plasma frequency, which is a parameter of the material depending on the free carrier concentration. Generally speaking, light with frequencies below the plasma frequency of the material will be reflected while above the plasma frequency will be transmitted. In more detailed descriptions, for light with frequencies below the plasma frequency, the phase difference between the vibration of the electrons in the materials and the oscillation of the electric field in the light wave is 1/4 of the period, and the light will be reflected. For light with frequencies above plasma frequency, the free electrons in the material cannot follow the vibration of the electrical field in the light wave; therefore the material becomes transparent at this wavelength. Figure4.5 (a) also indicates that at the short wavelength end, the transition point where samples start to become highly transparent blue shifts with the increase of the carrier concentration as well. This is mainly due to the increase in the effective band gap caused by the degenerate doping. As the doping level increases to degenerate level, the conduction band will be filled with electrons, preventing transitions from the

valence band to these filled states [83], [84]; therefore, transitions can only happened at higher energy states in the conduction band. This is defined as Burstein-Moss shift.

In Figure 4.6, we plot experimentally measured band gaps (purple dots and colored squares) as well as calculated band gaps for two values of effective mass m*(black solid line and blue dash line) as a function of the carrier concentration. The fitting curve with an effective mass 0.062 clearly fits experimental results better than an effective mass of 0.041 (pure InGaAs). The indication of this increased effective mass could either be due to the modification of the conduction band from the incorporation of bismuth or the degenerate doping. As one can see, at low doping concentrations, the fitting with a smaller effective mass matches the experimental data much better than at high doping concentrations. As doping increases, electrons fill high-energy states in the conduction band, and an increase in the electron effective mass is expected when we take the non-parobolicity of the conduction band into account.

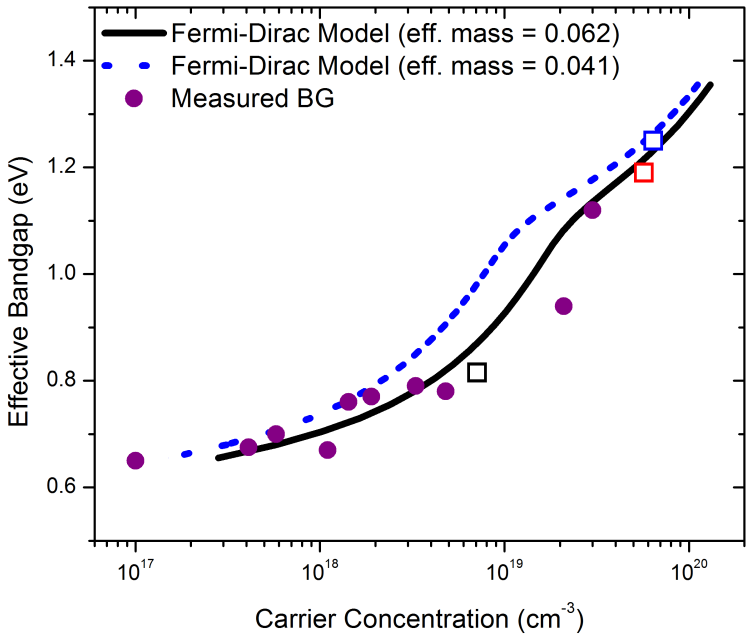

Figure 4.6 A plot of measured band gaps as well as two fitting curves with different effective mass m* from 0.041 to 0.062versus carrier concentration. The purple dots are from previous reported samples [79] and colored squares are corresponding to the three samples adopted in the previous discussion.

4.5 **Drude Model and Calculation of Transmittance**

We calculated the transmission spectra using the Drude model formalism. The complex dielectric constant can be expressed as:

$$\varepsilon(\omega) = \varepsilon_s\left(1 - \frac{\omega_p^2}{\omega^2 + i\omega\Gamma}\right) = \varepsilon_r + i\varepsilon_i = (n + ik)^2 \qquad \text{Equation 4.1}$$

where $\varepsilon(\omega)$ is the complex dielectric constant; ε_s is the relative permittivity; ω_p is the plasma frequency; Γ is the electron scattering rate; ε_r and ε_i are the real and imaginary parts of $\varepsilon(\omega)$;n and k are the real and imaginary parts of the complex

refractive index. In our simulations, we use the plasma frequency ω_p and scattering rate Γ as input parameters. The theoretical ω_p and Γ are given as:

$$\omega_p^2 = \frac{Ne^2}{\varepsilon_s \varepsilon_0 m^*} \qquad \text{Equation 4.2}$$

$$\Gamma = \frac{e}{\mu m^*} \qquad \text{Equation 4.3}$$

where N is the carrier concentration; e is the electron charge; ε_s (11.6 for $In_{0.48}Ga_{0.52}As$ and 4.0 for ITO [85]) is the relative permittivity; ε_0 is the vacuum permittivity; m*(0.062 for $In_{0.48}Ga_{0.52}As$ and 0.35 for ITO [85]) is the electron effective mass; μ is the electron mobility. Although the effective mass is dependent on the doping level due to non-parabolicity of the InGaAs conduction band, here we use a constant m* for the sake of simplicity.

Table 4.1 lists the free electron carrier concentration, mobility, theoretical ω_p and Γ calculated using Equation 4.2, 4.3, and the fitting ω_p and Γ.

Table 4.1 Experimental and fitting parameters for the transmission spectra

Sample	Carrier Concentration (cm^{-3})	Mobility ($cm^2V^{-1}s^{-1}$)	Theoretical ω_p (10^{14} s^{-1})	Fitting ω_p (10^{14} s^{-1})	Theoretical Γ (10^{13} s^{-1})	Fitting Γ (10^{13} s^{-1})
111103C	$7.1x10^{18}$	2311	1.77	1.5	1.23	1.1
120112C	$5.7x10^{19}$	532	5.02	3.1	5.32	5
120125A	$6.4x10^{19}$	320	5.32	3.32	8.85	8.5
ITO	$3.0x10^{20}$	44	8.28	6.5	11.39	15

Now that we know the plasma frequency ω_p and scattering rate Γ, we can calculate ε_r and ε_i from Equation 4.1. Figure4.7 (a) and (b) plot the ε_r and ε_i as a function of the wavelength. ε_r is related with the stored energy within the medium. As shown in Figure 4.7 (a), the transition point where the InGaBiAs:Si film becomes highly transparent due to the limit from the plasma frequency is corresponding to the position when ε_r turns to negative. The transition point of the films blue shifts as the carrier concentration increases. This exhibits the wavelength-flexibility of these materials through the control of the carrier concentration to adjust the highly transparent spectral region. ε_i is related with the energy dissipation within the medium. A small ε_i indicates a small power absorption skin depth. Therefore, an ideal transparent contact material should have a ε_r transition point sitting in the long IR range and a small ε_i corresponding to low loss. Comparing the three samples, the black one has the best property as a transparent contact material. The error bar of ε_r and ε_i comes from the fitting process of the transmission data. Because the fitting process is an indirect measurement of permittivity, there is some room in adjusting the scattering rate to get the best fitting.

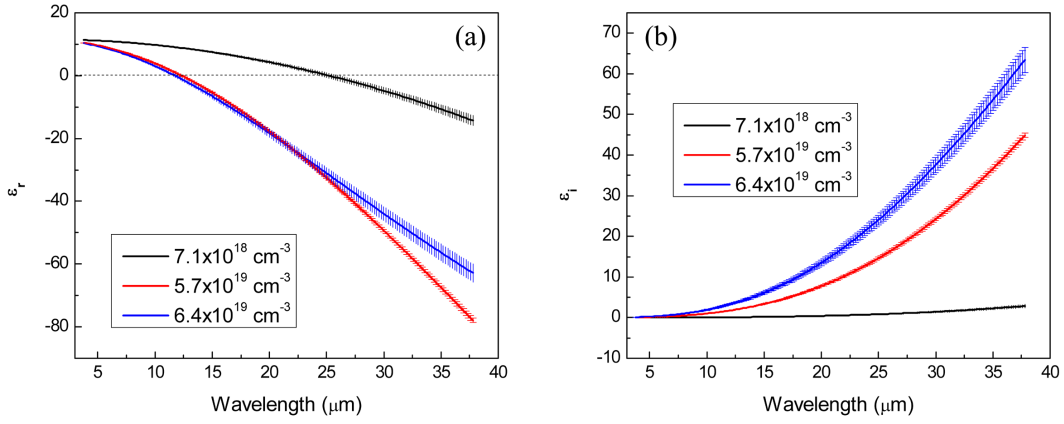

Figure 4.7 (a) and (b) exhibit the calculated ε_r and ε_i of the extracted dielectric constants $\varepsilon(\omega)$[82]. The error bars of ε_r and ε_i come from the uncertainty in the fitted scattering rate Γ.

The direct way to measure the transmission of InGaBiAs:Si films is to physically separate the film from the substrate which is impractical to achieve in the experiment. Generally, transmission spectra are normalized to the substrate by setting the light intensity transmitted through a single substrate as unity. This method is widely adopted for transparent contacts [67], [68], [71], but it intrinsically neglects the front surface reflection, which leads to an overestimated transmittance. This is acceptable if the front surface reflection is small. But in our case, the directly measured reflectance is around 30% which is clearly not negligible. Therefore, we choose to utilize the experimentally-extracted complex dielectric constant ε and calculate the amount of light that is transmitted into the InP substrate using a transfer matrix method based on Fresnel equation. The detailed calculation method is described here [76]. This value (dashed line in Figure4.5 (b)) is the truest representation of the transparency of the contact for the purposes of an optoelectronic device, and is therefore the transmittance we use for the Figure of Merit (FOM) calculations shown in Table 4.2 and Figure 4.8.

4.6 Comparison of InGaBiAs:Si and ITO as Transparent Contact Materials in the Infrared Range

There are many different standards for transparent contact materials. Ideally, we want the material to be transparent over a wide range of wavelengths and as conductive as possible. However, the transparency and conductivity are usually negatively correlated. So researchers have defined an empirically instructive figure of merit (FOM) to compare contact materials [86], which is believed to have a reasonable balance between the weight of the transmittance and conductivity. The FOM is defined as T^{10}/Rs, where T is either the average transmittance between two

wavelengths or the transmittance at the exact wavelength of interest, and Rs is the sheet resistance of the thin film. Figure4.8 compares the high transmittance window of InGaBiAs:Si films with the ITO film in the x axis and the FOM in the y axis. Here we used the calculation results that are closest to the real transmittance as we mentioned before. The length of the color bar represents the high transmittance region (T% > 65%) with units in wavelength. From Figure 4.8, we could conclude that each InGaBiAs:Si sample shown here has a transparent window extending farther into the IR range than ITO. In addition, the FOM of InGaBiAs:Si films is several orders of magnitude higher than that of ITO. Table 4.2 lists and compares the sheet resistance, the average transmission and the FOM for both InGaBiAs:Si and ITO directly. It is worth pointing out that the thickness of the thin films we studied here are larger than typical contact layers, which indicates the FOM can be even improved more by optimizing the thickness. In practice, contact layers could be optimized based on the requirements from a particular device and avoid potential interference effects.

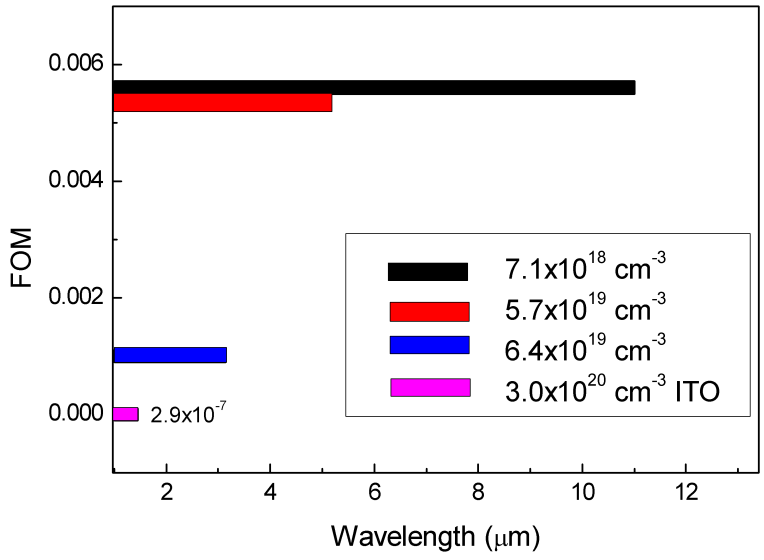

Figure 4.8 Comparison of the transparent windows (transmittance> 65%) of InGaBiAs:Si films and the ITO film as well as FOM in the wavelength range from 1 to 13 μm. An ideal transparent contact material should have long transparent window and high FOM in the desired wavelength range. The FOM of ITO is 2.9×10^{-7} □/ Ω, very close to zero. The inset shows the carrier concentration of each sample [82].

Table 4.2 Comparison of figure of merit for InGaBiAs:Si and ITO

Sample	Carrier Concentration (cm^{-3})	Rs (Ω/□)	Average Transmittance (λ=1 μm-6 μm)	FOM T^{10}/Rs (Ω^{-1})
111103C	7.1×10^{18}	7.05	0.72	0.0056
120112C	5.7×10^{19}	3.82	0.68	0.0054
120125A	6.4×10^{19}	5.65	0.60	0.0010
ITO	3.0×10^{20}	15.6	0.29	2.9×10^{-7}

4.7 **Summary**

In this chapter, we first introduced the background information about some current popular transparent contact materials and their disadvantages of being utilized as IR transparent contact materials. Then we introduced the electrical properties of InGaBiAs:Si samples and analyzed the reason why InGaBiAs:Si could have such high conductivity. Next, we showed the transmittance spectra of InGaBiAs:Si samples as well as that of ITO and described the origins of the threshold of the highly transparent region in both short wavelength and long wavelength end. Then we showed a Burstein-Moss shift model and discussed the effective mass of this material. Finally, we introduced an empirical FOM to compare transparent contact materials in terms of transparency and conductivity and conclude that degenerately doped InGaBiAs:Si are better candidates than ITO in the infrared range.

Chapter 5

DILUTE BISMUTHIDES APPLIED IN PHOTOVOLTAICS

In Chapter 3, we have discussed that the incorporation of Bi into III-V compounds can decrease the band gap and raise the valence band position. Therefore, we can utilize dilute bismuthides in band engineering to create some interesting structures. The upconversion solar cell is composed of a single junction solar cell and an upconverter. The efficiency of the upconverter is the key factor affecting the overall solar cell efficiency. Currently, the efficiency of the upconverter is limited by the undesired recombinations, but a new design of the upconverter including dilute bismuthides can effectively eliminate the undesirable recombinations and is expected to achieve a very high upconversion efficiency. Consequently, the overall solar cell efficiency will be greatly enhanced. Section 5.1 will introduce the development of solar cells in the past decades and compare some popular third generation solar cells. Section 5.2 will analyze the limiting parameters in the overall solar cell efficiency for an upconversion solar cell and discuss the most important one. Section 5.3 will describe in detail the new nanostructure of the upconverter and the physics why can it enable high upconversion efficiency. Section 5.4 will introduce the theoretical calculation of the dilute bismuthides component and selection rules. Section 5.5 is the summary.

5.1 **Overview of the Development of Solar Cells**

Photovoltaic (PV) allows the generation of power at very large scale and is promising to substitute for fossil fuel power. At present, the main stream PV cells are made out of single crystalline silicon with thickness between 180 to 300 μm due to its low price, earth abundance and mature processing techniques. In order to compete with current fossil-fuel technologies, the price of solar cells still needs to be significantly reduced.

Researchers have moved onto second generation solar cells, thin film solar cells, including polycrystalline and amorphous Si, GaAs, CuInGaSe and CdTe, due to decreased material costs saving from reduced amount of materials used. However, the efficiency of the second generation solar cell is limited by the near band gap absorption. The light absorption is poor due to the reduced layer thickness, and it is impractical to etch pyramidal texture structure to increase the light trapping as in the first generation solar cell[87], [88]. Therefore researchers have sought ways to increase light trapping by adding metallic nanostructures into the cell to support surface plasmons [89]–[92]. Light trapping has been improved through either light back-scattering or excitation of the surface plasmons. However, these methods are only effective for near or above band gap light absorption, and there is still a large amount of light with energies below the band gap got converted into heat.

Both first and second generation solar cells are based on single junction solar cells. There is a theoretical optimum band gap for all single junction solar cells. If the band gap is in the high energy end, the solar cell will output high voltage, but the majority of the photons with energies below the band gap will be wasted; if the band gap is in the low energy end, the solar cell will supply a high current, but the operating voltage will necessarily suffer. Thus there is a trade-off between the current and the

voltage. The theoretical maximum efficiency of a single junction solar cell has been proven to be 33% for an optimum energy band gap at 1.3eV by Shockley and Queisser in 1961[93]. This maximum efficiency indicates that no matter how well the light is absorbed by the single junction solar cells, it will not pass the 33% efficiency limit. This is defined as Shockley-Queisser(SQ) limit.

The third generation solar cells focus on improving the overall conversion efficiency by channeling excess photon energy normally lost to heat into usable free energy. One strategy is to make good utilization of the sub-band gap energy. Triple-junction solar cells, which utilize three materials with different band gaps to absorb the sun light over the whole spectrum (usually with a small band gap below 1 eV, a mid-band gap around 1.4 eV and a large band gap around 2 eV), could achieve efficiency in excess of 40% based on III-V semiconductors[94], [95]. However, the material cost and the complicated deposition process make the price of the triple-junction solar cells less competitive. Additionally, in order to achieve best performance, the cell structure design is subjected to the current match condition (the current operating at the maximum power of each junction should be the same), which is hard to satisfy at the same time with the other conditions like being lattice matched to the substrate or the optimum band gap distribution.

Multiple exciton generation(MEG) is to utilize the photons with energies at least twice larger than the band gap and down convert them into two photons, which could generate two electron-hole pairs and double the photon current. This gives a theoretical maximum efficiency at 39% for a 6000K blackbody spectrum with a luminescence converter with one intermediate level [96]. The first successful observation for MEG came in 2004 from PbSe nanocrystals [97]. But there are some

lingering questions about how to make use of it in a solar cell since getting charge carriers out of a nanocrystal-based solar cell will require making good contacts to each individual nanocrystal [98].

Intermediate band solar cell (IBSC) introduces an intermediate band in the middle of the band gap, which is proposed to allow absorption of photons across different energy thresholds[99], [100]. This approach has been realized through quantum dots [101], band anticrossing [102] and impurity level [103]. However, there are no efficient pathways to quickly draw free electrons and holes apart, and the intermediate band will act as recombination centers which will limit the practical improvement with such a design [104].

Apart from aforementioned methods, an alternative choice to utilize more of the solar spectrum and improve overall solar cell conversion efficiency is to attach an upconverter to a single junction solar cell [96], [105]. The upconverter could convert sub-band gap photons to above band gap photons, which could be reabsorbed by the single junction solar cell to increase the overall efficiency. Unlike multijunction or intermediate band solar cell, this upconverter is electrically isolated from the solar cell, which avoids the complication to satisfy the current match condition or the introduction of mid-band gap recombination centers. Upconversion has already been observed in lanthanide and transition-metal-ion systems,[106]–[109] quantum structures,[110], [111]and sensitized triplet-triplet-annihilation(TTA) molecules[112]–[114]. However, the highest upconversion efficiency obtained in these systems is around50%[115], [116] and a significant sacrifice of photon energy is required to achieve even this limited efficiency.

5.2 Analysis of Limiting Parameters in the Overall Solar Cell Efficiency for an Upconversion Solar Cell

In this section, we will first show the scheme of an upconversion solar cell and explain the basic working principle of it. Then we will analyze the two essential limiting factors to achieve high upconversion efficiency in a typical three energy level upconverter. In an upconversion process, usually two low-energy photons will be sequentially absorbed by the material and a third high-energy photon will be emitted.

Figure 5.1 shows the schematic plot of an upconversion solar cell. The high-energy photon will be absorbed by the host solar cell while the low-energy photons will pass through. An upconverter attached to the solar cell will absorb the low-energy photons transmitted through the back of the solar cell and convert the low-energy photons to high-energy photons. These high-energy photons can be reabsorbed by the host solar cell and get converted to photocurrent. The upconverter is electrically isolated from the host solar cell, so there will be no concerns about introducing a new recombination center or complicated current match conditions.

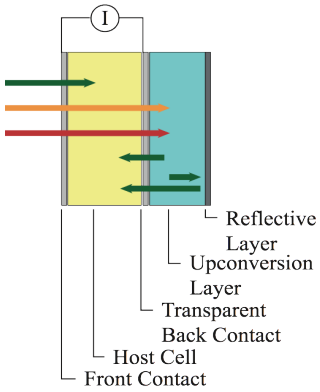

Figure 5.1 Schematic diagram of a single-junction solar cell equipped with an upconverter. Green arrows represent high-energy photons, which are absorbed by the solar cell and converted to photocurrent. Orange and red arrows are low-energy photons, which will pass through the solar cell, be transmitted to the upconverter and converted to high-energy photons. The high-energy photons will then be returned to the host solar cell and converted to extra photocurrent [117].

The energy band diagram of a simplified three energy level upconverter is shown in Figure 5.2. There are two important concepts in an upconversion process that need to be defined first: 1) upconversion quantum efficiency (UQE), which is defined as the fraction of the number of a pair of low energy photons get upconverted to a high-energy photon over the total incident photons and 2) photon energy sacrifice (PES), which is defined as the energy difference between the sum of the pair of low-energy photons and the emitted high-energy photons. The UQE is limited by both radiative and non-radiative recombination. The radiative recombination pathways are indicated in Figure5.2 by dashed lines. It is difficult to suppress the radiative recombination process across the low energy levels because the optical dipoles for absorption and emission of low-energy photons are equal.

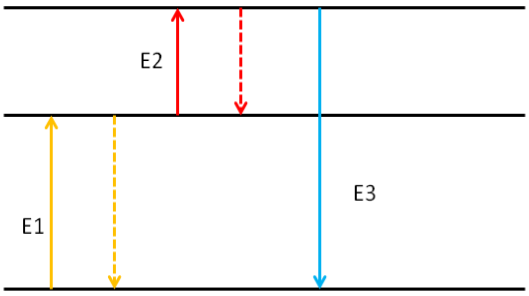

Figure 5.2 Scheme of a conventional three energy-level upconverter. The orange and the red solid arrow represent the absorption of small energy photons; while the dashed arrows indicate the radiative recombination. The blue arrow is the emitted high energy photon [117].

Two possible ways to suppress the radiative recombinations are 1) an efficient spatial separation of electron-hole pairs and a barrier to prevent them from recombining; 2)introducing some non-radiative relaxations to make the excited electrons fall into trap states in the band gap where further relaxation is forbidden.

Either of these processes requires some PES, as schematically depicted in Figure 5.3. However, the PES will decrease the maximum overall solar energy conversion as the reemitted photon energy is decreased, which limits the solar cell operation voltage. Ideally, we want a high UQE and a small PES to achieve high solar cell efficiency, but there is a trade-off between UQE and PES. Which one is more important in deciding the overall solar cell efficiency? The answer will be given in Section 5.3.

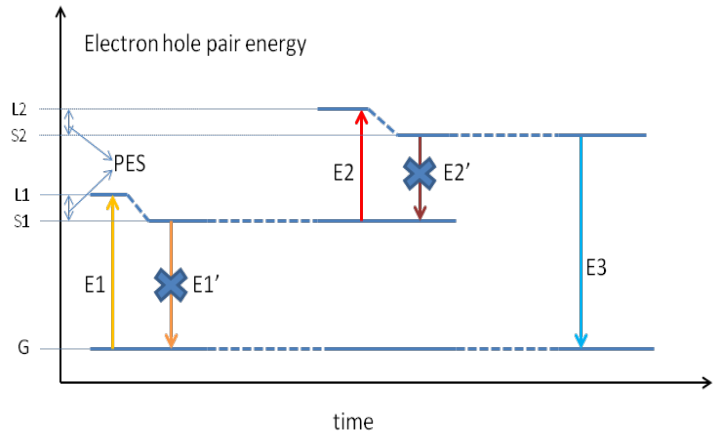

Figure 5.3 Schematic depiction of an efficient upconversion process. In this new process, the radiative recombinations are suppressed as indicated from the cross marks due to the introduction of PES between energy state L1, S1 and L2, S2 [117].

5.3 Calculation of Solar Cell Efficiency and Comparison of the Effect on the Overall Solar Cell Efficiency from Varied UQEs and PESs

The single junction solar cell efficiency is calculated based on an ideal diode model [118], and the upconversion solar cell efficiency is modified by the newly harvested photocurrent from the upconverter. As shown in Figure 5.4, a single-junction solar cell can be viewed as a diode working under illumination and reverse bias. The top curve will be the situation of a solar cell in dark which does not generate

any current; while the bottom curve represents the I-V curve of a working solar cell under illumination. V_{oc} and I_{sc} represent open circuit voltage and short circuit current respectively. The area of the square noted by the dashed lines equals to the output power of the solar cell.

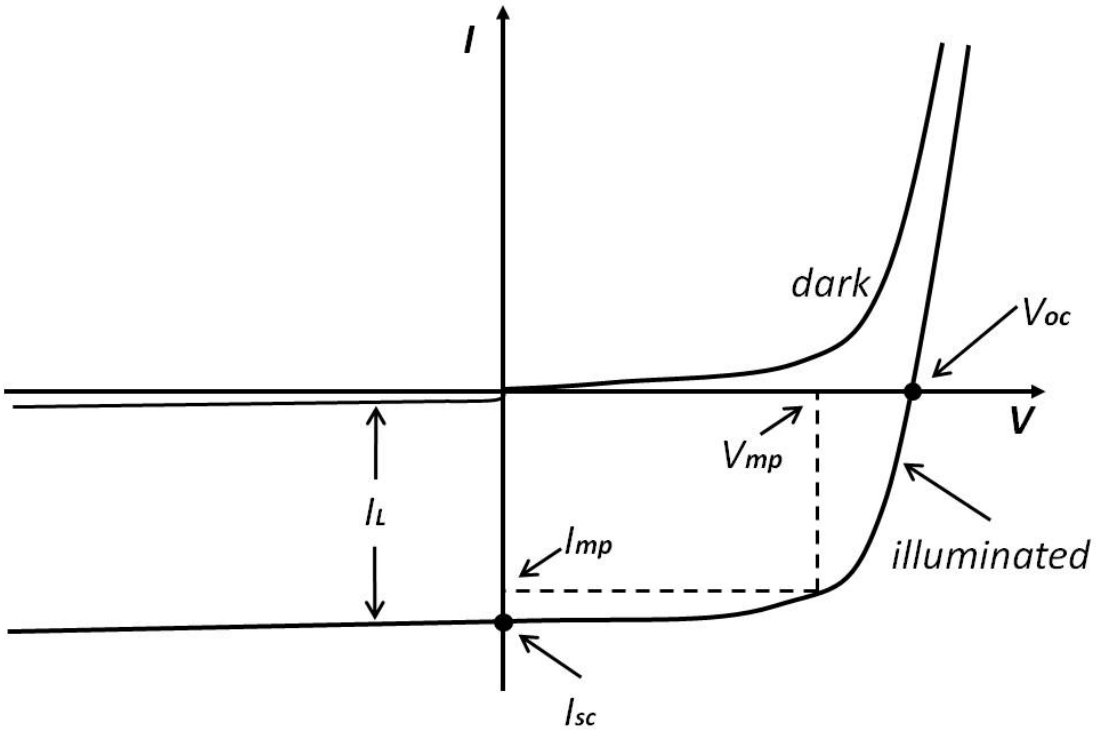

Figure 5.4 I-V curve of an ideal diode working in the dark and under illumination (http://www.intechopen.com/books/solar-cells-research-and-application-perspectives/electric-energy-management-and-engineering-in-solar-cell-system)

We used the AM1.5 solar spectrum to estimate the incident photon flux. Solar spectrum is very close to a black body radiation at 5800 k. AM1.5 is the modified solar spectrum at mid-latitudes when the sun light pass through the atmosphere and

light at certain wavelengths are get absorbed. It is widely adopted in solar cell efficiency calculation because it is the truest estimation of the incident solar energy radiated on the region where the majority of the population resides. The AM1.5 spectrum as a function of photon energy is given in Figure 5.5.

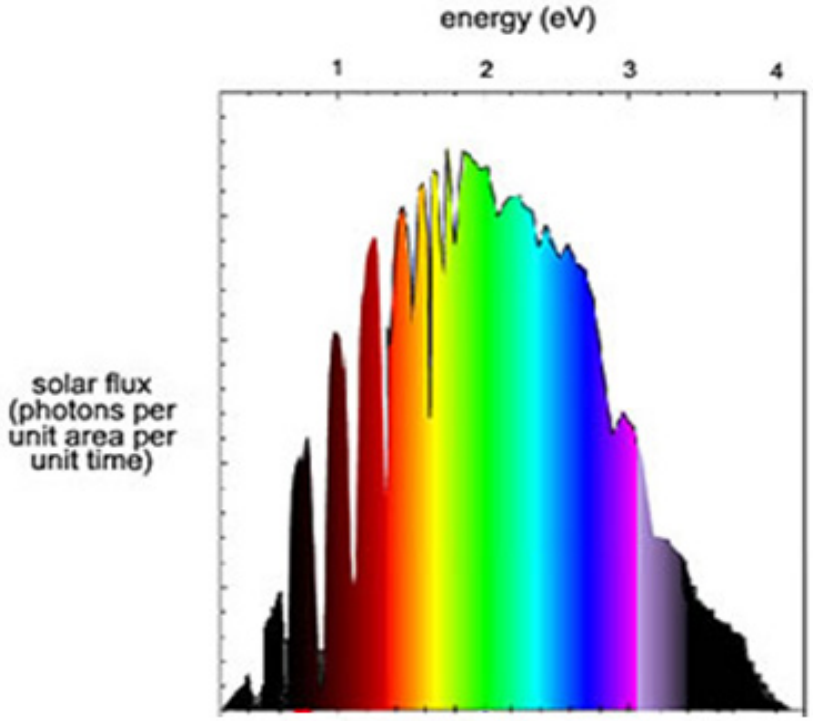

Figure 5.5 The AM1.5 spectrum as a function of the incident photon energy. (http://www.lbl.gov/Science-Articles/Archive/MSD-full-spectrum-solar-cell.html)

In a single junction solar cell, we assume only the photons with energies above the band gap will be absorbed and the only loss mechanism considered is radiative electron-hole pair recombination. Equation 5.1 gives the number of radiatively recombined electron-hole pairs of a single junction solar cell when it is at zero bias in the dark. We can see it is dependent on the band gap of the solar cell.

$$N_{rr0} = \frac{2\pi}{c^2 h^3} \int_{E_g}^{E_{max}} \frac{E^2}{Exp\left(\frac{E}{kT}\right) - 1} dE \qquad \text{Equation5.1}$$

where N_{rr0} is the number of radiatively recombined electron-hole pairs per unit area per unit time, c is the light speed, h is the Plank's constant, $E_g$is the band gap energy, E_{max} is the maximum photon energy in the AM1.5 spectrum, k is the Boltzmann's constant and T is the ambient temperature.

The cell is assumed to be thick enough to absorb all above-band-gap photons and each absorbed photon will contribute one electron-hole pair to the photocurrent. The total current output by the solar cell is equal to the photocurrent minus the current under reverse bias, which is an exponential function of the operation voltage. The ideal diode equation is given in Equation 5.2.

$$I = e[N_{phcu} - N_{rr0} Exp\left(\frac{eV}{kT}\right)] \qquad \text{Equation5.2}$$

Where I is the total current through the solar cell, N_{phcu} is the total number of photons absorbed above band gap energy E_g (calculated by an integral over the AM1.5 solar spectrum from E_g to E_{max}), V is the device operating voltage, and e is the electron charge.

The output power of a single junction solar cell is calculated by maximizing the product of its operating voltage V and the total current I, which is equivalent to maximize the area of the square inside the bottom curve in Figure 5.4. The solar cell efficiency is the ratio of the maximum solar cell output power over the total solar energy received from the sun. The result of this calculation is shown in Figure 5.6, which is also referred as SQ limit as we introduced before. The peak efficiency is around 33% when the band gap of the single junction solar cell is at ~1.3 eV.

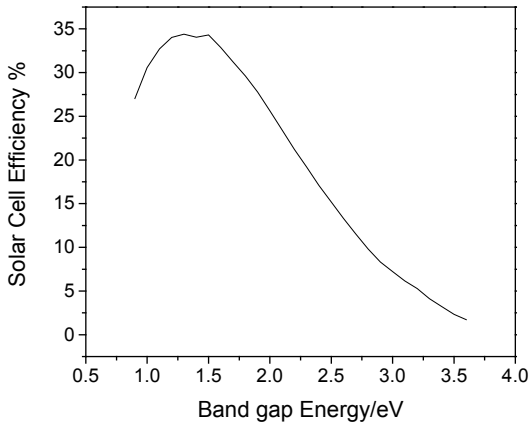

Figure 5.6 SQ limit of a single junction solar cell.

Now the efficiency of an upconversion solar cell can also be calculated using the same method aforementioned with the modified photocurrent including the newly harvested part. In this model, the host solar cell has a band gap E_g and the upconverter has three different energy transitions E1, E2 and E3 as shown in Figure 5.3. There are some general assumptions for this model. We first assume that photons will only be absorbed by the band gap that is closest but smaller than the photon energy. For example, photons with energies between E1 and E2 will only be absorbed by E2. We also assume that all the absorbed low-energy photons will be fully converted to high-energy photons. There are some other constraints on the relationship among E1, E2, E3, Eg and PES, which are listed in the following equations. These constraints will guarantee energy conservation:

$$E3 \leq E1+E2- PES \qquad \text{Equation5.3}$$

$$E2<E1<E3 \qquad \text{Equation5.4}$$

$$E3+PES< 2E1 \qquad \text{Equation5.5}$$

Equation 5.3 requires that the sum of E1 and E2 minus the PES is still larger than E3. Equation 5.4 decides the magnitude relationship among the three band gaps. Equation 5.5 is a deduction based on Equation 5.3 and 5.4 since the sum of E1 and E2 should be larger than the sum of E3 and PES, and E1 should be greater than E2.

To calculate the extra photons generated by the upconverter, we first set a value of E_g and numerically consider all possible combinations for E1 and E2 under the aforementioned constraints. The number of photons absorbed in each transition is calculated by integrating from the band gap to the high energy end of the AM1.5 spectrum. The maximum number of emitted high-energy photons is obtained when the number of photons absorbed by E1 and E2 are equal. This is similar to the current match condition in a multijunction solar cell. But it only requires two current matching, and there is no need for current matching with the solar cell. The band gaps that satisfy the current matching condition are shown in Figure 5.7. The value of E1 and E2 will change with the host cell band gap E3. Based on these values, we can calculate the maximum number of additional photons that can be added to the photon flux and repeat the ideal diode calculations to calculate the efficiency of the single junction solar cell with an upconverter.

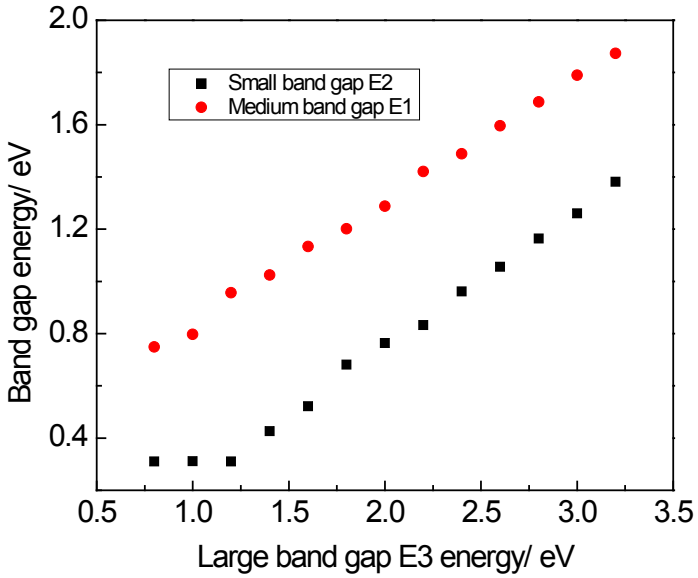

Figure 5.7 Combinations of E1, E2 and E3 when they satisfy the current matching condition [117].

After we understand the way to calculate the solar cell efficiencies, now we need to consider the aforementioned two parameters UQE and PES in an upconversion process. As we mentioned before, there is a trade-off between these two parameters. Here we first consider the consequences of imperfect UQE with a constant PES of 50 meV. Imperfect UQE is modeled by adding different percentage of the maximum number of additional high-energy photons at a given band gap. Figure 5.8shows the overall upconversion solar cell efficiency as a function of host cell band gap with different UQE values. We first observe that the solar cell efficiency varies in a large range with distinct UQEs. At zero UQE (black line), the solar cell efficiency shows the SQ limit which agrees with the result shown in Figure 5.6. However, when the

UQE is increased to 100% (purple curve), the peak solar cell efficiency reaches nearly 60%.Even if upconversion is only 50%efficient (blue curve), the peak solar cell efficiency can still exceed 40%. This indicates that the upconversion solar cell efficiency depends significantly on the UQE. In other words, a high UQE is crucial to achieve high solar cell efficiency in an upconversion solar cell.

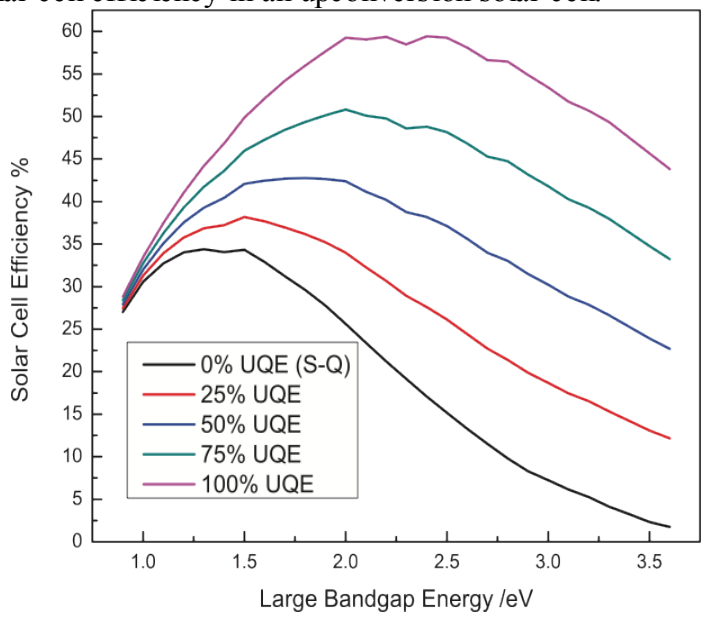

Figure 5.8 Upconversion solar cell efficiency based on different UQEs [117].

As mentioned previously, it requires a PES to increase UQE through the suppression of radiative loss pathways. Figure 5.9shows the effect from varied PES values, where the UQE is assumed to be 100% all the time. The first thing we will notice is that the solar cell efficiency does not depend strongly on the PES as it does on UQE. With a 0 meV PES, the peak solar cell efficiency exceeds 60%; even with a PES of 300 meV, which is much more than we need, the peak solar cell efficiency is still near 55%. Therefore, we can conclude that the overall solar cell efficiency will

benefit much more from a high UQE than a small PES. If an increased PES will lead to an increase in UQE, it would be a desirable solution to significantly improve the solar cell efficiency.

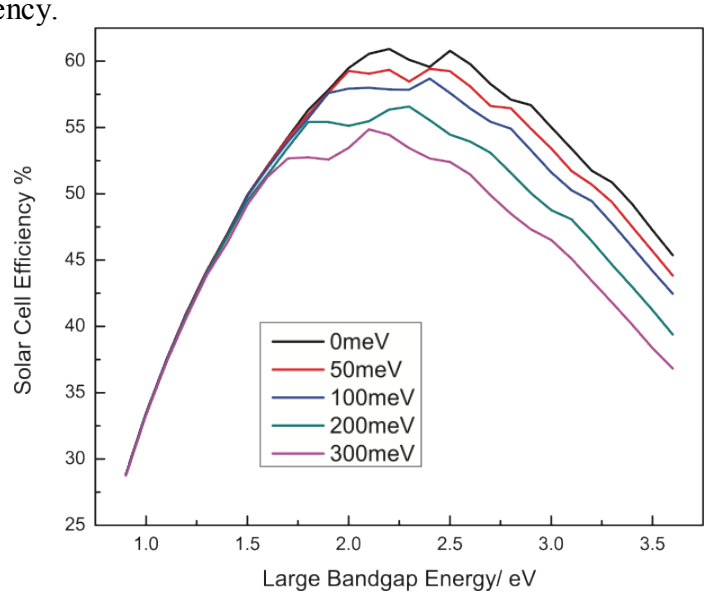

Figure 5.9 Upconversion solar cell efficiency based on varied PES [117].

There have been other work considering similar model of the upconversion solar cell [105], [119]. But the difference between the previous models and our model is that they treat the upconversion process as a series of two small band gap solar cells driving a LED. The way they chose to suppress the radiative recombination in the upconversion process is to apply a voltage to the small band gap cells[105], [119].This applied voltage is in the reverse direction as opposed to the operating voltage of the solar cell, which will necessarily lead to an operation voltage smaller than the material band gap and waste some photon energy to heat. It can be deemed as an enforced enlargement of PES. In these models, a PES around 300 meV was required to improve the overall solar energy conversion efficiency[105].

5.4 The New Upconverter with Nanostructure

In the previous section, we have stated the importance to have a high UQE in order to achieve high solar cell efficiency. The two main limiting factors in an efficient upconverter are radiative and non-radiative loss pathways. We have mentioned about introducing a PES to achieve a high UQE, which has been confirmed in Trupke and Atre's model. In their model, a reverse bias is introduced to separate the electron-hole pair generated by the upconverter, and a PES around 300 meV is estimated in such system.

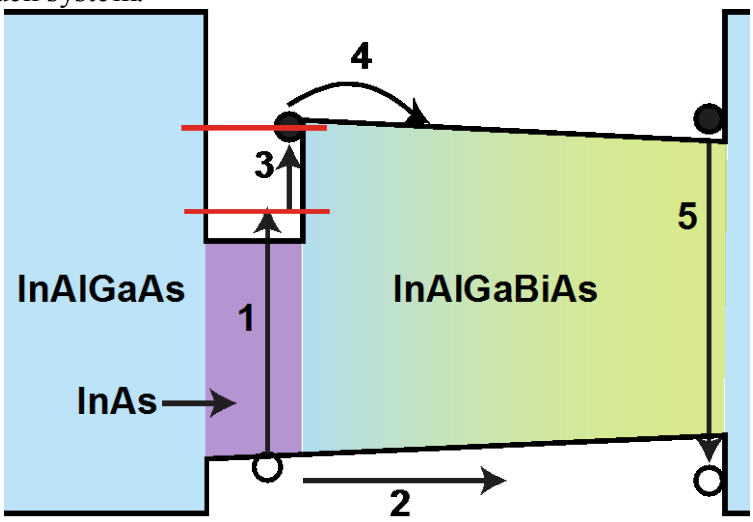

Figure 5.10 Schematic plot of the new upconverter [117].

Here, we will develop a new design which does not require any external applied voltage to maximize UQE with a PES as small as 50 meV. Figure 5.10 shows a schematic band diagram for this new design. This new upconverter is composed of an InAs quantum dot (QD) buried between an AlGaAs and an InAlBiAs barrier. InAs QD is supposed to absorb the low-energy photons, and the energy of the discrete states can be controlled by the size of the QD. The low-energy photons with energies larger

than transition 1 will be absorbed, and electron-hole pairs will be generated. Electrons will be promoted from the valence band to the lowest-energy confined level of the QD (process 1); while holes will be attracted to right edge of the InAlBiAs barrier layer where the desired recombination region is (process 2). This electron-hole pair separation is achieved due to the zero valence band offset between the InAs QD and InAlBiAs barrier layer as well as the built-in electric field resulting from the graded InAlBiAs barrier layer. Therefore, radiative recombination of the electron-hole pair within the QD is suppressed by the rapid spatial separation of the electron-hole pair. The concentration gradient in the InAlBiAs layer will provide approximately 25 meV built-in potential to prevent phonons from exciting the hole back to the valence band of the QD and recombine with the trapped electron. This is the first intentional PES, which approximately equals to 1kTat room temperature. When the second low-energy photon got absorbed, it will promote the previous confined electron staying on the first energy level to the second energy level within the QD (process 3).

Previously we have mentioned that radiative and non-radiative recombinations are the two main loss path ways that limit high UQE, and we just discussed how to suppress the radiative recombination. Now we point out that non-radiative relaxation of the excited electron on the second energy level can be suppressed as long as the rate of tunneling through the thin triangular barrier as the left edge of the InAlBiAs barrier layer (process 4) is faster than the fastest loss pathway. It has been demonstrated that non-radiative relaxation in a QD happens on 10s of picoseconds timescale due to the phonon bottleneck created by the discrete density of states in the QD[120];while tunneling from high-energy QD states through thin triangular barriers typically occurs on picosecond timescales[121], [122].This indicates that the life time of a high energy

state electron is 10 times longer than the tunneling time, and the non-radiative recombination can be effectively suppressed by the discrete energy states of the QD. Like a symmetrical setting, electrons also need a barrier at least 25 meV high to prevent it from back flowing to the QD, and the second intentional PES is introduced. This conduction band gradient of the InAlBiAs layer will also provide a built-in potential to attract the electron to the recombination region, recombine with the previous hole, and emit a high energy photon (process 5).

5.5 **Materials Parameters in Designing the New Upconverter**

The upconversion nanostructure depicted in Figure 5.10 can effectively suppress both radiative and non-radiative recombinations with a PES of only 25 meV for both conduction and valence band. This nanostructure is not subject to any specific material, and any material could work as long as it can satisfy this band diagram. Our approach is to implement an InAs QD and an InAlBiAs graded layer. InAs QD is the most conventional QD grown by Stranski-Krastanov (SK) method, which is also referred as layer-plus-island growth mode. The SK mode involves a two-step process: 1) deposit a several monolayer-thick film until it is beyond the critical thickness; 2) the layer will separate into isolated islands due to the strain between the film and the substrate. This growth technique is relatively mature and the energy states of the QD can be controlled by the size. InAlBiAs belongs to this new group of materials-dilute bismuthides. As we mentioned before, incorporating a small amount of bismuth into conventional III-V semiconductors (GaAs, InGaAs, InAlAs) will cause VBAC that raises the valence band[42], [53], [61] without significantly affecting the conduction band of the matrix material. Therefore, we can tune the conduction band and valence

band positions independently by adjusting the ratio between the group III and group V elements respectively.

To specify the detailed material requirements, we need to set up the experimental measurement system. Figure 5.11 include the experimental constraints as well as the detailed parameters for each optical transition. As shown in Figure 5.11, we plan to use a 1064 nm (1.17 eV) source for band gap E1(transition 1) and a 1550 nm (0.80 eV) source for band gap E2 (transition 3). These wavelengths correspond to very common commercially available optical sources and have approximately the right energy ratio to utilize the solar spectrum. Once we set down the optical pumps, along with the constraints we mentioned as Equation 5.3-5.5, we can discuss the acceptable range for each transition. Energy of transition 1 must be greater than transition 3 (0.8 eV) so that the only optical pump that can generate electron-hole pairs will be 1064 nm source. Meanwhile, energy of transition 5 must be greater than transition 1 (1.17 eV) in order to prevent absorption of the re-emitted photons in the recombination zone. These constraints guarantee that each optical source selectively excites a transition. To guarantee that both conduction band and valence band can provide a barrier layer high enough to prevent the back flow of electrons and holes from the recombination region, the sum of the excitation energies for transitions 1 and 3 should be 100 meV higher than that of transition 5 in total, which allows a 50 meV offset for conduction and valence band separately. This offset creates a PES equal to 2 kT at room temperature at each band edge, which should be sufficient to suppress phonon-mediated recombination and maximize UQE. To sum up, the left edge of the InAlBiAs barrier height should be between 1.6 and 1.8 eV while has zero valence

band offset with the InAs QD, and the right edge of the InAlBiAs barrier height should be between 1.3 and 1.55 eV.

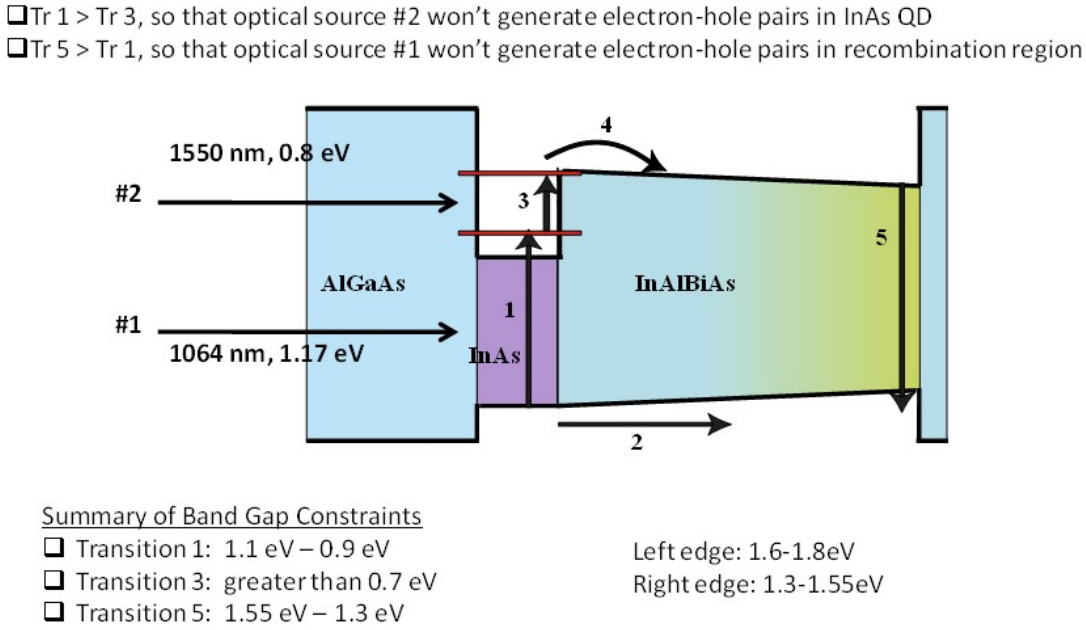

Figure 5.11 Constraints of the band gaps in the new upconverter.

In Section 3.2, we have described in detail how to predict the band gap of InGaBiAs from a VBAC model. We could have followed the routine to calculate the band gap of InAlBiAs as a function of the composition if there were experimental results of InAlBiAs compounds. However, there have not been any reported experimental results for this material. Therefore, in order to predict the band gap of InAlBiAs, we adopt the same VBAC model we used for InGaBiAs, change the matrix energy and the impurity energy level, and borrow the interaction strength from the InGaBiAs results. Calculating the band gap of InAlBiAs is much more complicated than that of InGaBiAs because InAlAs has direct band gap ($32\% \leq In\% \leq 100\%$) and indirect band gap ($0\% \leq In\% < 32\%$) over the whole concentration region. But this

method is the best we can use for now, and further refinement will be added once experimental data are available.

Figure 5.12 shows the band gap of InAlBiAs in the direct band gap range as a function of Bi concentration, and Figure 5.13 shows the composition in the indirect band gap range. Meanwhile, the valence band position of the InAlBiAs quaternary alloys with the compositions shown in Figure 5.12 and Figure 5.13 is equal to that of the InAs QD. As we required, the left edge of the InAlBiAs barrier height should be between 1.6 and 1.8 eV. Comparing Figure 5.12 and 5.13, we can see that only InAlBiAs with composition in the indirect band gap range satisfy this confinement.

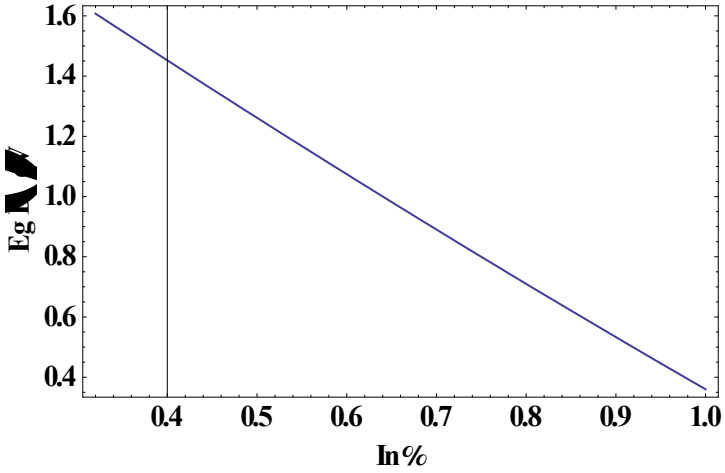

Figure 5.12 Band gap of InAlBiAs as a function of In concentration in the direct band gap range when it has zero valence band offset with the InAs QD.

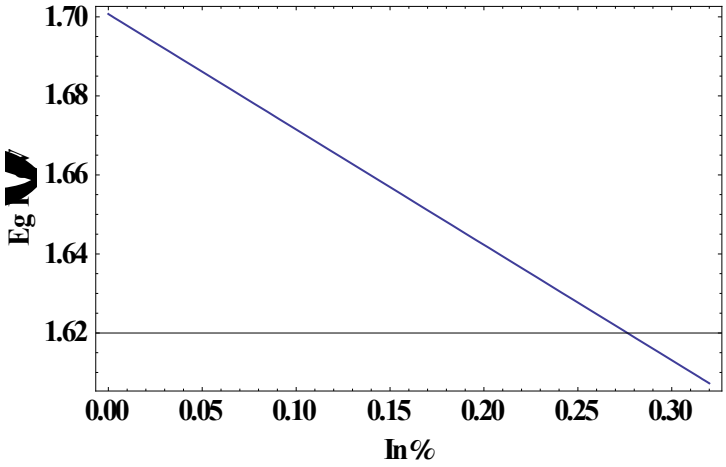

Figure 5.13 Band gap of InAlBiAs as a function of In concentration in the indirect band gap range when it has zero valence band offset with the InAs QD.

Therefore, the composition of this quaternary alloy could be calculated. Figure 5.14 shows the indium concentration as a function of bismuth concentration when InAlBiAs have zero valence band offset with the InAs QD. Meanwhile, the band gap of InAlBiAs is in the indirect band gap range.

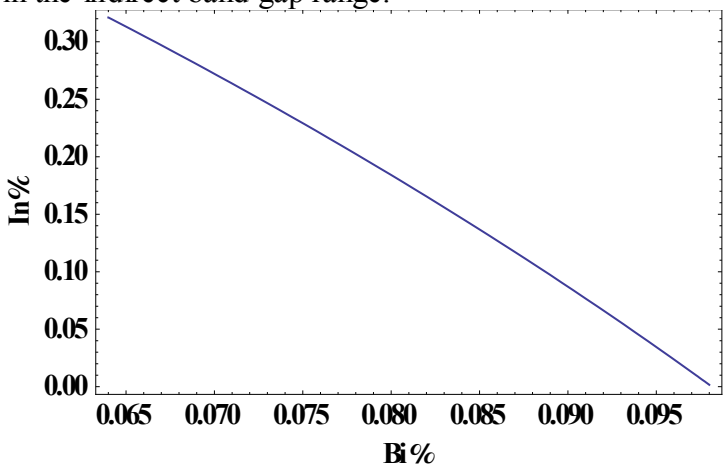

Figure 5.14 In concentration as a function of Bi concentration for InAlBiAs when it has zero valence band offset with the InAs QD. This composition resides in the indirect band gap range due to the bang gap requirements from Equation 5.3-5.5.

Similarly, we first calculated the direct band gap and indirect band gap of InAlBiAs with the confinement that the valence band is 50 meV higher than that of InAs QD. Recall that we require that right edge of InAlBiAs to be between 1.3-1.55 eV, the direct band gap InAlBiAs satisfies the restrains. The results are given in Figure 5.15.

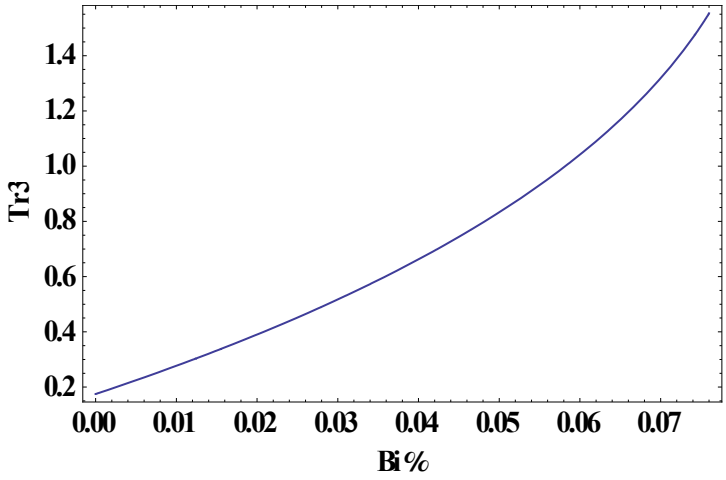

Figure 5.15 Band gap of InAlBiAs as a function of bismuth concentration with the constraints of the right edge of the barrier layer. This composition resides in the direct band gap range.

Thus, the composition of the right edge of InAlBiAs barrier layer is given in Figure 5.16. It is given in the form that the bismuth concentration as a function of indium concentration.

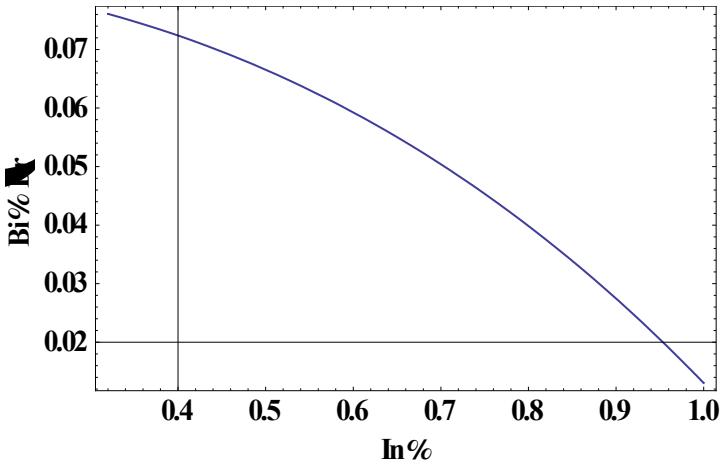

Figure 5.16 The composition of the right edge of the InAlBiAs barrier layer

Finally, to make sure that the left edge of the InAlBiAs barrier height is at least 50 meV higher than the right edge, we plot the energy difference, which is calculated by using the band gap of the left barrier to minus that of the right barrier and 50 meV, as a function of the bismuth concentration. The results are shown in Figure 5.17, where we assume that the bismuth concentration is constant through the whole barrier, and the only thing varies is the In concentration.

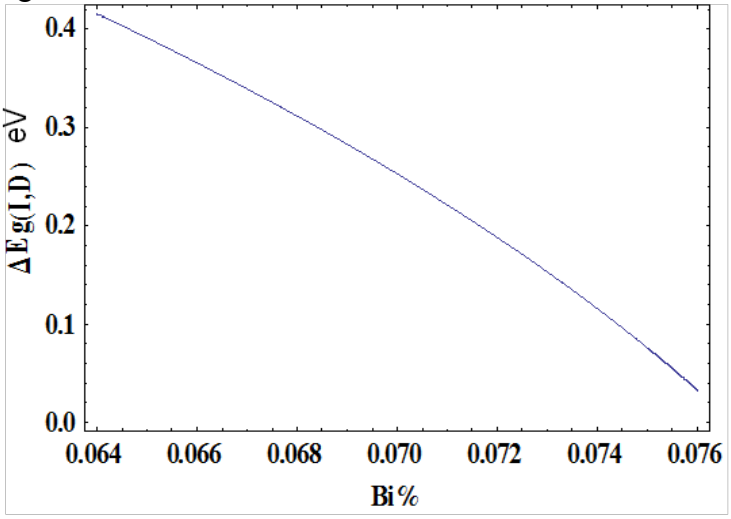

Figure 5.17 The extra energy difference between the left edge, right edge and a PES of 100meV as a function of bismuth concentration.

Combining Figure 5.12, 5.13 and 5.17, we can get the composition range that satisfies the requirements for the left edge of the InAlBiAs barrier layer, which means the height of the left barrier should be between 1.6-1.8 eV, the valence band position is equal to that of the InAs QD, and the valence band and conduction band are 50 meV higher than the corresponding bands of the right edge of InAlBiAs. The results are indicated by the red line in the contour plot of the band gap of InAlBiAs as shown in Figure 5.18. Values range from $In_{0.27}Al_{0.73}Bi_{0.07}As_{0.93}$ to $In_{0.23}Al_{0.77}Bi_{0.075}As_{0.925}$.

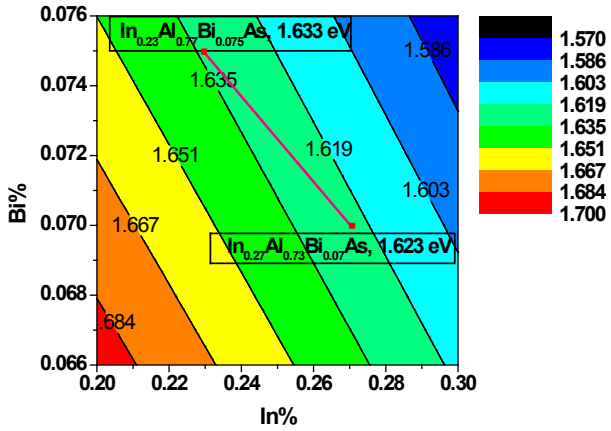

Figure 5.18 The acceptable composition range (red line) of the left edge of the InAlBiAs barrier layer in a contour band gap plot [117].

The red line in Figure 5.19 shows the range of compositions appropriate for the recombination zone, with values between $In_{0.44}Al_{0.56}Bi_{0.07}As_{0.93}$ and $In_{0.35}Al_{0.65}Bi_{0.075}As_{0.925}$.

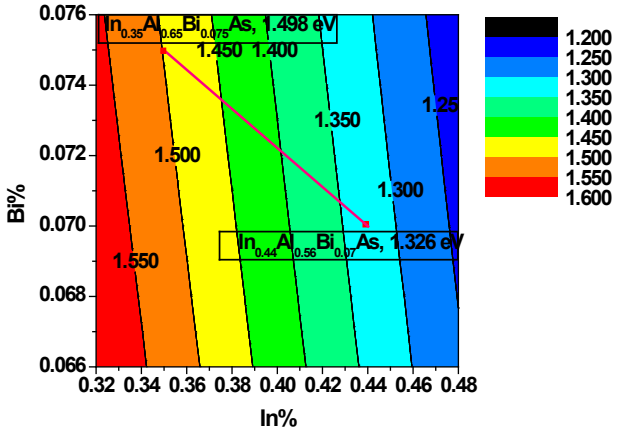

Figure 5.19 The acceptable composition range (red line) of the right edge of the InAlBiAs barrier layer in a contour band gap plot [117].

Conveniently, the left edge happen to fall in indirect band gap range of InAlBiAs, which will further hinder the electron-hole recombination at this region; while the right edge of InAlBiAs barrier has a direct band gap which is beneficial for electron-hole recombination. This is a happy coincidence.

5.6 **Summary**

We have shown that an upconversion solar cell could theoretically achieve an efficiency of 60%, which is a great improvement compared to a peak efficiency of 33% for single junction solar cells. But this significant improvement depends heavily on an efficient upconversion process. We have demonstrated that there is the PES and the UQE are competing with each other, and a high UQE is more important in terms of high solar cell efficiency than a small PES. A new design for a nanostructured upconverter is proposed to suppress both radiative and nonradiative recombinations, which are the two main limiting factors in achieving high upconversion efficiency.

This design is expected to allow a PES of only 50 meV to reach high UQE. The new nanostructured upconverter is realized by implementing an InAs QD and InAlBiAs graded barrier layer. The feasibility of this design is demonstrated by calculating specific compositions of InAlBiAs alloys that realize the required band gaps and alignments. This model is not limited to any specific material and will inspire new materials for single junction solar cells.

Chapter 6

CONCLUSIONS AND FUTURE DIRECTION

In the previous chapters, we have discussed the growth conditions, composition and morphology characterization, strain and relaxation study, optical, and electrical properties of dilute bismuthides. We have also proposed the possible applications of dilute bismuthides in mid-IR optoelectronics, infrared transparent contact materials and photovoltaics. Indeed, this is just the tip of an iceberg, and there is a large amount of treasures waiting for us to explore. In this chapter, I will point out some future directions and draw a conclusion on dilute bismuthides. In Section 6.1, I will describe the motivation for high bismuth concentration films. Section 6.2 will list some feasible methods to achieve high bismuth concentration. Section 6.3 will discuss some future directions in understanding band structures of dilute bismuthides. Section 6.4 will introduce a new application in temperature-insensitive band gap materials. Finally, Section 6.5 will draw a conclusion on dilute bismuthides.

6.1 Motivation for High Bismuth Concentration Films

Previously, we have shown the application of InGaBiAs in mid-IR optoelectronics and produced InGaBiAs films with the longest wavelength up to 2.7 μm. Pushing the cut-off wavelength into the long wavelength range will require high percentage of bismuth to incorporate. This increase of bismuth concentration will not only produce films with smaller band gaps, but also make the fundamental band gap smaller than Δ_{SO}, which can eliminate the CHSH Auger process.

It is predicted that when the bismuth concentration is large enough, the spin orbit splitting energy Δ_{SO} will outweigh the fundamental band gap, and the CHSH Auger process and intervalence band absorption (IVBA) will be suppressed. This is especially important for mid-IR laser application since CHSH and IVBA have been demonstrated to lead to high threshold current [16]. Researchers have calculated the fundamental band gap and the spin orbit splitting energy Δ_{SO} as a function of bismuth concentration for GaBiAs/GaAs and InGaBiAs/InP. The results are given in Figure 6.1.

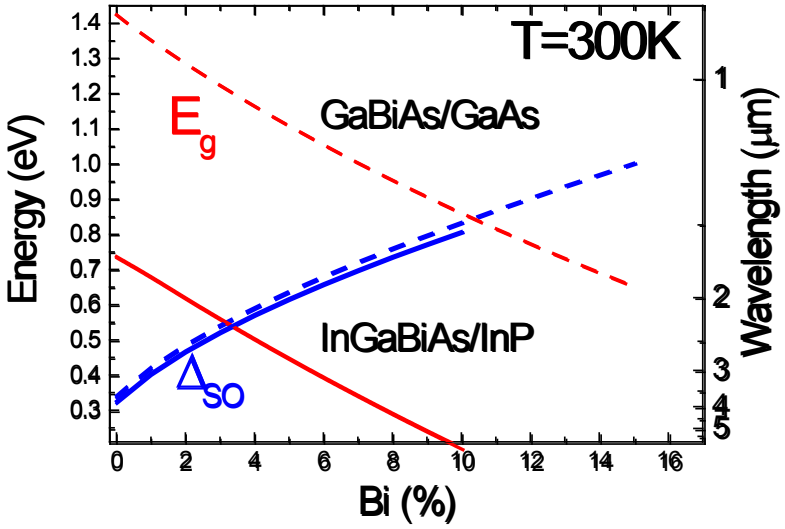

Figure 6.1 Comparison of the fundamental band gap Eg and the spin-orbit splitting energy $\Delta_{SO}$of GaBiAs/GaAs and InGaBiAs/InP as a function of bismuth concentration [123].

From Figure 6.1, we can see that the bismuth concentration required to achieve $\Delta_{so}>E_g$ for InGaBiAs/InP is much less than for GaBiAs/GaAs. This is another advantage of InGaBiAs/InP over GaBiAs/GaAs system considering the increase of

bismuth concentration is difficult. Figure 6.2 shows the theoretical predictions as well as the experimental measurements of the fundamental band gap E_g and the spin orbit splitting Δ_{so}'s dependence on bismuth concentration. The theory and experiment agree very well and the flipping of Δ_{so} and E_g is achieved in one sample with a bismuth concentration of 5%. The fundamental band gap of the 5% bismuth sample is off the prediction a lot, and this could be due to the effect from the strain. The model will be refined once more experimental data are available.

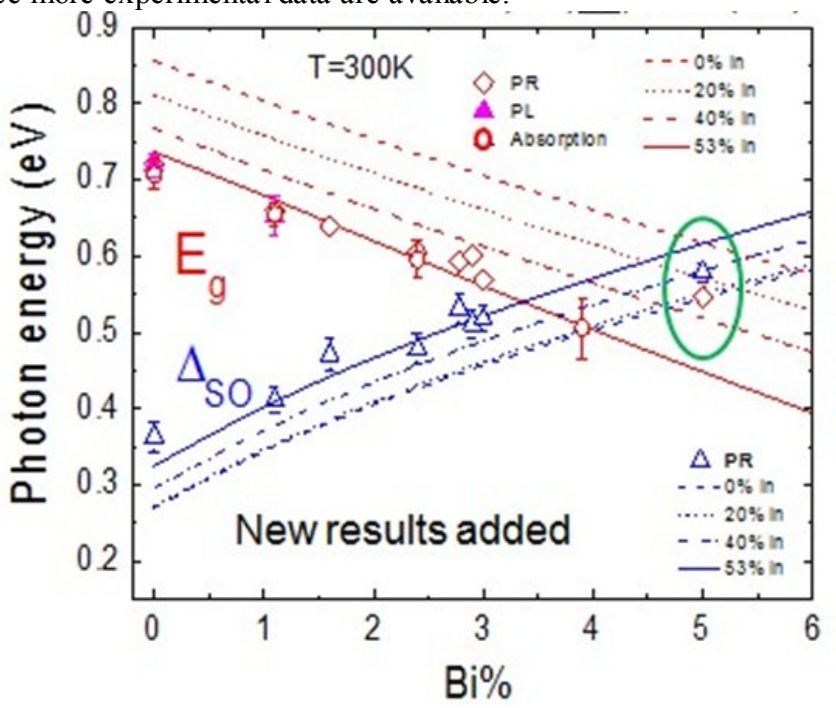

Figure 6.2 Experimental measurements and theoretical prediction of the fundamental band gap Eg and Δ_{SO} of InGaBiAs/InP as a function of bismuth concentration [123].

6.2 **Feasible Methods to Achieve High Bismuth Concentration**

In Section 2.1, we have discussed two ways to increase the bismuth concentration: lowering the growth temperature and increasing the bismuth flux.

However, there is a plateau of bismuth concentration when we keep decreasing the growth temperature, and Bi droplets start to appear on the surface if we keep increasing the bismuth flux. There is still some room in pushing in these two directions since the highest bismuth concentration ever incorporated is 21.5% for GaBiAs on GaAs [124]. But other than keep refining the growth skills, another possible method to increase the bismuth concentration is to introduce bismuth growth interruption, a similar method adopted in nitride growths.

The idea to introduce bismuth growth interruption originates from the growth of InGaN with high indium concentration. It is reported that high indium concentration InGaN compounds are difficult to produce due to the spinodal decomposition, indium surface segregation, and thermal decomposition [125]. Therefore, high indium content InGaN requires a low growth temperature and a special growth technique called metal modulated epitaxy (MME). MME is to introduce the Group III elements incorporating interruption by opening and closing Group III shutters periodically to achieve high Group III concentration. The Group III flux needs to be extremely high, and Group V is meanwhile kept at a constant flux all the time. It is believed that the periodic modulation of the incorporated Group III fluxes allows for complete consumption of excess metal on the surface, preventing droplets or phase segregation from persisting throughout the growth. This explanation is confirmed by *in-situ* RHEED oscillation intensity transients associated with different growth modes. By attributing these RHEED oscillation intensity transients to shutter-open-time-dependent features, one can clearly control the growth by opening the Group III shutter to let the adsorption of the first monolayer of excess metal, and close the Group III shutter before a full oscillation happened. This will halt the supply of metal to the surface and allow the

truncation of excess metal accumulation before a full monolayer is formed. After the Group III shutters are closed, the RHEED will show up the oscillation sign again, indicating that the excess metal have all been consumed and a flat surface is formed again.

It is not hard to notice the resemblance between the growth of high indium concentration InGaN alloys and high bismuth content InGaBiAs alloys. They both require to be grown at low temperatures, both have the spinodal growth region, and both show the sign of phase segregation. Therefore, introducing growth interruption for Group V, especially for bismuth, seems to be a feasible way to increase the bismuth concentration when merely increasing bismuth flux will unavoidably produce bismuth droplets. What I proposed here is to utilize very high bismuth flux (higher than the limit of bismuth flux that will produce bismuth droplets) and open and close the Group V shutters periodically while keep the Group III shutters open. This will allow the consumption of extra bismuth and achieve high bismuth content films. The scheme of the growth process is given in Figure 6.3.

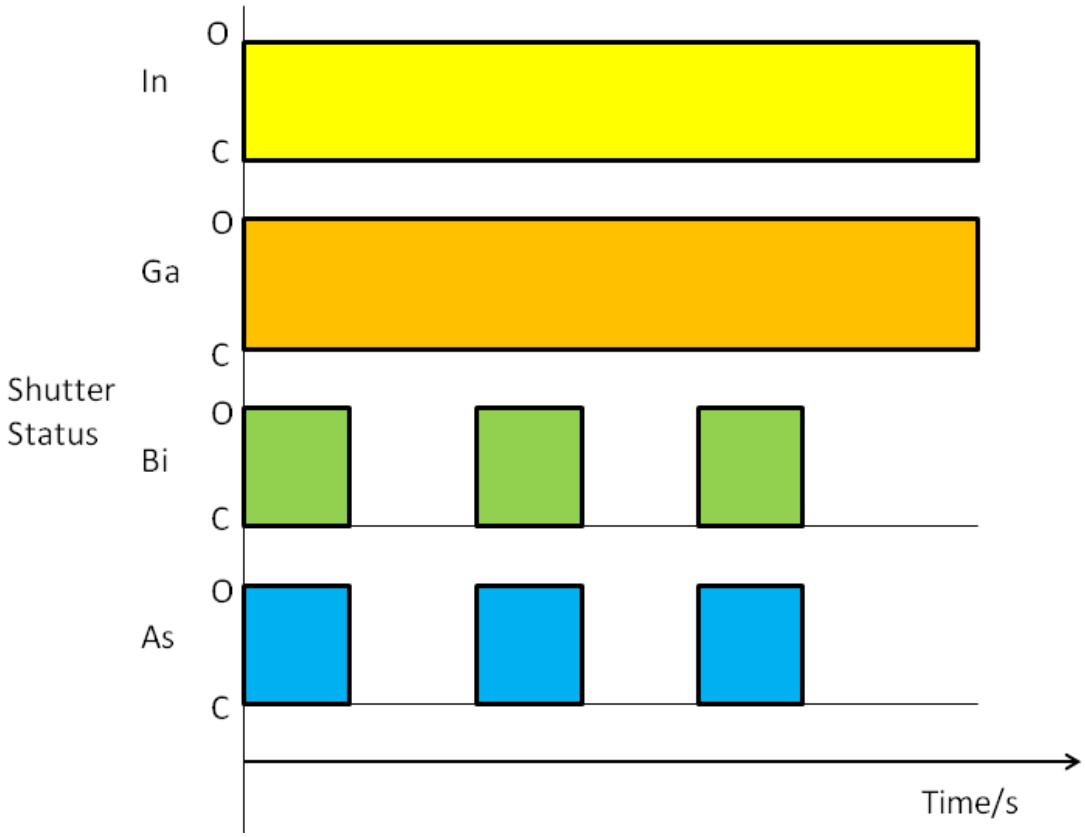

Figure 6.3 Growth process of InGaBiAs using growth interruption technique

6.3 Future Work in Understanding the Physics of Dilute Bismuthides Band Structures

In Section 3.3, we have discussed the change of positions of the conduction band, valence band and split-off spin-orbit band due to the increase of bismuth concentration in dilute bismuthides. Experimental results have confirmed that the conduction band and the split-off spin-orbit band stay still while the valence band moves towards the conduction band when the bismuth concentration increases. But it still remains in mystery that whether there are two separate valence bands and whether the valence band is extended band like or just a localized resonant state.

The splitting of conduction band in dilute nitrides has been reported through photo reflectivity measurements [128]. The derivative characteristic peaks corresponding to the transition of E-, Δ_{so}, and E+ peak are unambiguously observed in GaInNAs with a nitrogen concentration of 1.2% [126]. However, the splitting of valence band in dilute bismuthides is only predicted in theory, but has not been clearly observed in experiment yet [16]. This is either due to the nature of dilute bismuthides, or the relatively low material quality which will require improvement in the growth conditions or new growth methods.

Whether the newly added state is a localized state or an extended state like can be determined by studying the photoluminescence under hydrostatic pressure. A localized state will have a much weaker pressure dependence as compared to the conduction/valence band edge. There has been study of dilute nitrides under hydrostatic pressure [126]. At atmosphere, the N level represents the E- band and resides above the conduction band as you may recall Figure 1.4. But the hydrostatic pressure increase will raise the bottom of the conduction band above the N level, which demonstrates that the N level is not as sensitive as the conduction band and is therefore localized. This band shift will make the character of E- band from extended-like to localized-like, and the E+ band from the localized-like to extended-like. However, to the best of my knowledge, there still lacks the study of dilute bismuthides under hydrostatic pressure. This study will help us to further understand the structure of dilute bismuthides.

6.4 **Application in Temperature-insensitive Band Gap Materials**

Temperature-insensitive band gap materials have great applications in devices that are sensitive to the wavelength variation and require external control to keep the

temperature constant. For example, wavelength-division-multiplexing (WDM) system requires a Peltier cooler to stabilize the device temperature, which not only lacks the portability but also is very expensive.

Normally, the band gap of the semiconductor red shifts with the increased ambient temperature due to the strain caused by the thermal expansion. However, there are some anomalous materials having a positive gap coefficient dependence on temperature, which means that the band gap of the material will blue shift with the increase of the environmental temperature. Such materials include PbS, PbSe and PbTe which have an inverse valence band and conduction band[17]. But they are not semimetals due to the two-fold spin degeneracy in both conduction band and valence band [128]. It is proposed that the combination of alloys with positive gap-coefficient and negative gap-coefficient can create compounds that have band gaps insensitive to temperature, which could be realized in HgCdTe/Se and bismuth containing III-V alloys materials system [17].

But there have been no clear experimental results confirming that the band gaps of dilute bismuthides are temperature insensitive. In fact, some of our measurements indicated that the temperature dependence of the band gap of dilute bismuthides showed no difference from the host material InGaAs [61], [128]. Kudrawiec *et. al.* have confirmed that both the fundamental band gap of InGaBiAs and the $E_0 + \Delta_{SO}$ transition red shifts with the increase of the temperature. The amplitude of each transition is around 50-60 meV and 80-90 meV respectively over a temperature variation from 15k to 295k, which is close to the host material over the same temperature range [61]. Similarly, Marko *et. al.* find no clear evidence of the suggested reduction in the temperature dependence of the band gap with increasing Bi

concentration [128]. Either the theoretical prediction is problematic or higher Bi concentration sample is required to observe this trend.

6.5 **Summary**

In this section, we have concluded some current problems in the dilute bismuthides research, possible solutions and future directions. We first stated that high bismuth concentration samples are highly desirable due to the possibility to suppress CHSH Auger recombination. Then one possible growth method to further increase the bismuth concentration is introduced. Next, we described some future directions in better understanding the band structures of dilute bismuthides. Finally, we discussed one possible application for dilute bismuthides in temperature-insensitive band gap materials, but there have been no experimental results to support this propose.

REFERENCES

[1] "http://en.wikipedia.org/wiki/Gallium_arsenide." .

[2] "http://en.wikipedia.org/wiki/Aluminum_arsenide." .

[3] M. F. Chang, *Current trends in heterojunction bipolar transisters*. World Scientific Publishing, 1996

[4] O. Ueda, S. J. Pearton, *Materials and reliability handbook for semiconductor optical and electron devices.* New York, NY :Springer, 2013.

[5] L. Liu, A. R. Alt, H. Benedickter, and C. R. Bolognesi, "Low power consumption millimeter-wave amplifiers using InP HEMT technology," *IEEE MTT-S Int. Microw. Work. Ser. Millim. Wave Integr. Technol.*, 2011.

[6] J. A. Van Vechten and T. K. Bergstresser, "Electronic Structures of Semiconductor Alloys," *Phys. Rev. B*, vol. 1, no. 8, 1970.

[7] K. Alberi, J. Blacksberg, L. D. Bell, S. Nikzad, K. M. Yu, O. D. Dubon, and W. Walukiewicz, "Band anticrossing in highly mismatched Sn_xGe_{1-x} semiconducting alloys," *Phys. Rev. B*, vol. 77, no. 073202, 2008.

[8] I. Vurgaftman and J. R. Meyer, "Band parameters for nitrogen-containing semiconductors," *J. Appl. Phys.*, vol. 94, no. 6, p. 3675, 2003.

[9] J. Wu, W. Walukiewicz, K. M. Yu, J. D. Denlinger, W. Shan, J. W. Ager III, A. Kimura, H. F. Tang, and T. F. and Kuech, "Valence band hybridization in N-rich $GaN_{1-x}As_x$ alloys," *Phys. Rev. B*, vol. 70, no. 115214, 2004.

[10] W. Walukiewicz, W. Shan, K. Yu, J. W. Ager III, E. E. Haller, I. Miotkowski, M. J. Seong, H. Alawadhi, and A. K. Ramdas, "Interaction of localized electronic states with the conduction band: band anticrossing in II-VI semiconductor ternaries," *Phys. Rev. Lett.*, vol. 85, no. 7, 2000.

[11] "http://en.wikipedia.org/wiki/Atomic_radius." .

[12] "http://en.wikipedia.org/wiki/Electronegativity." .

[13] U. Tisch, E. Finkman, and J. Salzman, "The anomalous bandgap bowing in GaAsN," *Appl. Phys. Lett.*, vol. 81, no. 3, 2002.

[14] S. Adachi, *Physical Properties of III-V Semiconductor Compounds*. Wiley, 1992.

[15] B. Foran, N. Presser, Y. Sin, and S. C. Moss, "Thermally Driven Chemical Diffusion and Failure of InGaAs-AlGaAs Strained Single Quantum Well Laser Diodes," *Microsc. Microanal.*, vol. 13, no. S02, 2007.

[16] C. A. Broderick, M. Usman, and S. J. Sweeney, "Band engineering in dilute nitride and bismide semiconductor lasers." *Semicond. Sci. Technol.* vol. 27, no. 094011, 2012

[17] K. Oe, "Proposal on a Temperature-Insensitive Wavelength Semiconductor Laser" *IEICE Trans. Electron*. vol. E79-C, no. 12, 1996

[18] A. Mascarenhas, Y. Zhang, J. Verley, and M. J. Seong, "Overcoming limitations in semiconductor alloy design," *Superlattices and Microstruct.*, vol. 29, no. 6, 2001.

[19] S. Tixier, M. Adamcyk, E. C. Young, J. H. Schmid, and T. Tiedje, "Surfactant enhanced growth of GaNAs and InGaNAs using bismuth," *J. Cryst. Growth*, vol. 251, no. 1–4, 2003.

[20] S. Tixier, M. Adamcyk, T. Tiedje, S. Francoeur, A. Mascarenhas, P. Wei, and F. Schiettekatte, "Molecular beam epitaxy growth of $GaAs_{1-x}Bi_x$," *Appl. Phys. Lett.*, vol. 82, no. 14, 2003.

[21] H.-X. Deng, J. Li, S.-S. Li, H. Peng, J.-B. Xia, L.-W. Wang, and S.-H. Wei, "Band crossing in isovalent semiconductor alloys with large size mismatch: First-principles calculations of the electronic structure of Bi and N incorporated GaAs," *Phys. Rev. B*, vol. 82, no. 19, 2010.

[22] K. Oe and H. Okamoto, "New Semiconductor Alloy $GaAs_{1-x}Bi$ x Grown by Metal Organic Vapor Phase Epitaxy," *Jpn. J. Appl. Phys.*, vol. 37, no. 11, 1998.

[23] S. Tixier, M. Adamcyk, T. Tiedje, S. Francoeur, A. Mascarenhas, P. Wei, and F. Schiettekatte, "Molecular beam epitaxy growth of $GaAs_{1-x}Bi_x$," *Appl. Phys. Lett.*, vol. 82, no. 14, 2003.

[24] M. Yoshimoto, S. Murata, A. Chayahara, Y. Horino, J. Saraie, and K. Oe, "Metastable GaAsBi Alloy Grown by Molecular Beam Epitaxy," *Jpn. J. Appl. Phys.*, vol. 42, no. 10B, 2003.

[25] A. D. Howard, D. C. Chapman, and G. B. Stringfellow, "Effects of surfactants Sb and Bi on the incorporation of zinc and carbon in III/V materials grown by organometallic vapor-phase epitaxy," *J. Appl. Phys.*, vol. 100, no. 4, 2006.

[26] W. Li, T. Jouhti, C. S. Peng, J. Konttinen, P. Laukkanen, E.-M. Pavelescu, M. Dumitrescu, and M. Pessa, "Low-threshold-current 1.32-μm GaInNAs/GaAs single-quantum-well lasers grown by molecular-beam epitaxy," *Appl. Phys. Lett.*, vol. 79, no. 21, 2001.

[27] P. Laukkanen, J. Pakarien, M. Ahola-Tuomi, M. Kuzmin, R.E. Perala, and I. J. Vayrynen "Structural and electronic properties of Bi-adsorbate-stabilized reconstructions on the InP(100) and $GaAs_xN_{1-x}$(100) surfaces," *Phys. Rev. B*, vol. 74, no. 155302, 2006.

[28] T. Tiedje, E. C. Young and A. Mascarenhas, "Growth and Properties of the Dilute Bismide Semiconductor GaAs," *Int. J. Nanotechnol.*, 2008.

[29] M. Henini, J. Ibáñez, M. Schmidbauer, M. Shafi, S. V. Novikov, L. Turyanska, S. I. Molina, D. L. Sales, M. F. Chisholm, and J. Misiewicz, "Molecular beam epitaxy of GaBiAs on (311)B GaAs substrates," *Appl. Phys. Lett.*, vol. 91, no. 25, 2007.

[30] X. Lu, D. A. Beaton, R. B. Lewis, T. Tedje. and M. B. Whitwick. "Effect of molecular beam epitaxy growth conditions on the Bi content of $GaAs_{1-x}Bi_x$.pdf," *Appl. Phys. Lett.*, vol. 92, no. 192110, 2008.

[31] A. G. Norman, R. France and A. J. Ptak, "Atomic ordering and phase separation in MBE $GaAs_{1-x}Bi_x$.pdf," *J. Vac. Sci. Technol. B Microelectron. Nanom. Struct.*, vol. 29, no. 03C121, 2011.

[32] G. Ciatto, E. C. Young, F. Glas, J. Chen, R. A. Mori, and T. Tiedje, "Spatial correlation between Bi atoms in dilute $GaAs_{1-x}Bi_x$: From random distribution to Bi pairing and clustering," *Phys. Rev. B*, vol. 78, no. 035325, 2008.

[33] S. Francoeur, M.-J. Seong, A. Mascarenhas, S. Tixier, M. Adamcyk, and T. Tiedje, "Band gap of $GaAs_{1-x}Bi_x$, $0<x<3.6\%$," *Appl. Phys. Lett.*, vol. 82, no. 22, 2003.

[34] R.E. Nahory, M. A. Pollack, W. D. Johnston Jr, R. L. Barns. "Band gap versus composition and demonstration of Vegard's law for $In_{1-x}Ga_xAs_yP_{1-y}$ lattice matched to InP," *Appl. Phys. Lett.*, vol. 33, no. 7, 1978.

[35] P. Wei, S. Tixier, M. Chicoine, S. Francoeur, A. Mascarenhas, T. Tiedje, and F. Schiettekatte, "Ion beam characterization of $GaAs_{1-x-y}N_xBi_y$ epitaxial layers," *Nucl. Instruments and Methods in Phys. Res. Sect. B,* vol. 219–220, Jun. 2004.

[36] M. Y. W. Huang, K. Oe, G. Feng, "Molecular-beam epitaxy and characteristics of $GaNyAs_{1-x-y}Bi_x$," *J. Appl. Phys.*, vol. 98, no. 053505, 2005.

[37] B. Fluegel, S. Francoeur, A. Mascarenhas, S. Tixier, E. Young, and T. Tiedje, "Giant Spin-Orbit Bowing in $GaAs_{1-x}Bi_x$," *Phys. Rev. Lett.*, vol. 97, no. 6, 2006.

[38] D. G. Cooke, F. A. Hegmann, E. C. Young, and T. Tiedje, "Electron mobility in dilute GaAs bismide and nitride alloys measured by time-resolved terahertz spectroscopy," *Appl. Phys. Lett.*, vol. 89, no. 12, 2006.

[39] G. Feng, M. Yoshimoto, K. Oe, A. Chayahara, and Y. Horino, "New III-V Semiconductor InGaAsBi Alloy Grown by Molecular Beam Epitaxy," *Jpn. J. Appl. Phys.*, vol. 44, no. No. 37, 2005.

[40] G. Feng, K. Oe, and M. Yoshimoto, "Bismuth containing III-V quaternary alloy InGaAsBi grown by MBE," *Phys. Status Solidi*, vol. 203, no. 11, 2006.

[41] G. Feng, K. Oe, and M. Yoshimoto, "Temperature dependence of Bi behavior in MBE growth of InGaAs/InP," *J. Cryst. Growth*, vol. 301–302, Apr. 2007.

[42] Y. Zhong, P. B. Dongmo, J. P. Petropoulos, and J. M. O. Zide, "Effects of molecular beam epitaxy growth conditions on composition and optical properties of $In_xGa_{1-x}Bi_yAs_{1-y}$," *Appl. Phys. Lett.*, vol. 100, no. 11, 2012.

[43] A. Janotti, S. H. Wei, and S. Zhang, "Theoretical study of the effects of isovalent coalloying of Bi and N in GaAs," *Phys. Rev. B*, vol. 65, no. 11, 2002.

[44] "http://prism.mit.edu/xray/Introduction%20to%20HRXRD.pptx." .

[45] W. X. Ni, K. Lyutovich, J. Alami, C. Tengstedt, M. Bauer and E. Kasper, "X-ray reciprocal space mapping studies of strain relaxation in thin SiGe layers (≤100nm) using a low temperature growth step," *J. Cryst. Growth*, vol. 227–228, no. 1–4, 2001.

[46] J. Hornstra, "Determination of the lattice constant of epitaxial layers of III-V compounds," *J. Cryst. Growth*, vol. 44, no. 5, 1978.

[47] M. A. Moram and M. E. Vickers, "X-ray diffraction of III-nitrides," *Reports Prog. Phys.*, vol. 72, no. 3, 2009.

[48] J. W. Matthews and A. E. Blaskeslee, "Defects in epitaxial multilayers," *J. Cryst. Growth*, vol. 27, 1974.

[49] G. Vardar, M. V. Warren, M. Kang, S. Jeon, and R. S. Goldman, presentation at the 28th North American Molecular Beam Epitaxy Conference, San Diego, CA, 2011.

[50] X. Lu, D. A. Beaton, R. B. Lewis, T. Tedje. and M. B. Whitwick. "Effect of molecular beam epitaxy growth conditions on the Bi content of $GaAs_{1-x}Bi_x$.pdf," *Appl. Phys. Lett.*, vol. 92, no. 192110, 2008.

[51] R. N. Kini, L. Bhusal, A. J. Ptak, R. France, and A. Mascarenhas, "Electron Hall mobility in GaAsBi," *J. Appl. Phys.*, vol. 106, no. 043705, 2009.

[52] R. N. Kini, A. J. Ptak, B. Fluegel, R. France, R. Reedy, and A. Mascarenhas, "Effect of Bi alloying on the hole transport in the dilute bismide alloy $GaAs_{1-x}Bi_x$," *Phys. Rev. B*, vol. 83, no. 7, 2011.

[53] J. P. Petropoulos, Y. Zhong, and J. M. O. Zide, "Optical and electrical characterization of InGaBiAs for use as a mid-infrared optoelectronic material," *Appl. Phys. Lett.*, vol. 99, no. 3, 2011.

[54] S. M. Wang, G. Adolfsson, H. Zhao, Y. X. Song, M. Sadeghi, J. Gustavsson, P. Modh, Å. Haglund, P. Westbergh, and A. Larsson, "Growth of dilute nitrides and 1.3 μm edge emitting lasers on GaAs by MBE," *Phys. Status Solidi*, vol. 248, no. 5, 2011.

[55] X. Lu, D. A. Beaton, R. B. Lewis, T. Tiedje, and Y. Zhang, "Composition dependence of photoluminescence of $GaAs_{1-x}Bi_x$ alloys," *Applied Physics Letters*, vol. 95, no. 4. 2009.

[56] C. A. Broderick, M. Usman, and E. P. O'Reilly, "12-band k·p model for dilute bismide alloys of (In)GaAs derived from supercell calculations," *Phys. Status Solidi*, vol. 250, no. 4, Apr. 2013.

[57] V. Swaminathan, *Materials Aspects of GaAs and InP Based Structures*. Prentice Hall, 1991.

[58] K. Alberi, O. D. Dubon, W. Walukiewicz, K. M. Yu, K. Bertulis, and A. Krotkus, "Valence band anticrossing in $GaBi_xAs_{1-x}$," *Appl. Phys. Lett.*, vol. 91, no. 5, 2007.

[59] G. Ciatto, E. C. Young, F. Glas, J. Chen, R. A. Mori, and T. Tiedje, "Spatial correlation between Bi atoms in dilute $GaAs_{1-x}Bi_x$: From random distribution to Bi pairing and clustering," *Phys. Rev. B*, vol. 78, no. 035325, 2008.

[60] G. Ciatto, G. Thomasset, F. Glas, X. Lu, and T. Tiedje, "Formation and vanishing of short range ordering in $GaAs_{1-x}Bi_x$ thin films," *Phys. Rev. B*, vol. 82, no. 201304(R), 2010.

[61] R. Kudrawiec, J. Kopaczek, J. Misiewicz, J. P. Petropoulos, Y. Zhong, and J. M. O. Zide, "Contactless electroreflectance study of E_0 and $E_0 + \Delta_{SO}$ transitions in $In_{0.53}Ga_{0.47}Bi_xAs_{1-x}$ alloys," *Appl. Phys. Lett.*, vol. 99, no. 25, 2011.

[62] K. Alberi, J. Wu, W. Walukiewicz, K. Yu, O. Dubon, S. Watkins, C. Wang, X. Liu, Y. J. Cho, and J. Furdyna, "Valence-band anticrossing in mismatched III-V semiconductor alloys," *Phys. Rev. B*, vol. 75, no. 4, 2007.

[63] R. Kudrawiec, "Application of contactless electroreflectance to III-nitrides," *Phys. Status Solidi*, vol. 247, no. 7, 2010.

[64] "http://en.wikipedia.org/wiki/Electrical_resistivity_and_conductivity." .

[65] and A. B. Gururaj V. Naik, Jongbum Kim, "Oxides and nitrides as alternative plasmonic in the optical range," *Opt. Mater. Express*, vol. 1, no. 6, pp. 1090–1099, Mar. 2011.

[66] G. V. Naik, J. Kim, and A. Boltasseva "Oxides and nitrides as alternative plasmonic in the optical range," *Opt. Mater. Express*, vol. 1, no. 6, 2011.

[67] D. S. Ghosh, L. Martinez, S. Giurgola, P. Vergani, and V. Pruneri, "Widely transparent electrodes based on ultrathin metals.," *Opt. Lett.*, vol. 34, no. 3, pp. 325–7, Feb. 2009.

[68] Z. Wu, Z. Chen, X. Du, J. M. Logan, J. Sippel, M. Nikolou, K. Kamaras, J. R. Reynolds, D. B. Tanner, A. F. Hebard, and A. G. Rinzler, "Transparent, conductive carbon nanotube films.," *Science*, vol. 305, no. 5688, 2004.

[69] L. Hu, D. S. Hecht, and G. Grüner, "Infrared transparent carbon nanotube thin films," *Appl. Phys. Lett.*, vol. 94, no. 8, 2009.

[70] W. Xu, Y. Gong, L. Liu, H. Qin, and Y. Shi, "Can graphene make better HgCdTe infrared detectors?," *Nanoscale Res. Lett.*, vol. 6, no. 1, 2011.

[71] D. S. Ghosh, T. L. Chen, and V. Pruneri, "High figure-of-merit ultrathin metal transparent electrodes incorporating a conductive grid," *Appl. Phys. Lett.*, vol. 96, no. 4, 2010.

[72] D. S. Hecht, L. Hu, and G. Irvin, "Emerging transparent electrodes based on thin films of carbon nanotubes, graphene, and metallic nanostructures.," *Adv. Mater.*, vol. 23, no. 13, pp. 1482–513, Apr. 2011.

[73] D. Zhang, K. Ryu, X. Liu, E. Polikarpov, J. Ly, M. E. Tompson, and C. Zhou, "Transparent, conductive, and flexible carbon nanotube films and their application in organic light-emitting diodes.," *Nano Lett.*, vol. 6, no. 9, 2006.

[74] C. G. Granqvist, "Transparent conductors as solar energy materials: A panoramic review," *Sol. Energy Mater. Sol. Cells*, vol. 91, no. 17, 2007.

[75] D. C. Adams, S. Inampudi, T. Ribaudo, D. Slocum, S. Vangala, N. A. Kuhta, W. D. Goodhue, V. A. Podolskiy, and D. Wasserman, "Funneling Light through a Subwavelength Aperture with Epsilon-Near-Zero Materials," *Phys. Rev. Lett.*, vol. 107, no. 13, 2011.

[76] S. Law, D. C. Adams, A. M. Taylor, and D. Wasserman, "Mid-infrared designer metals.," *Opt. Express*, vol. 20, no. 11, 2012.

[77] J. P. Petropoulos, Y. Zhong, and J. M. O. Zide, "Optical and electrical characterization of InGaBiAs for use as a mid-infrared optoelectronic material," *Appl. Phys. Lett.*, vol. 99, no. 3, p. 031110, 2011.

[78] T. Fujii, T. Inata, K. Ishii, and S. Hiyamizu, "Heavily Si-doped InGaAs lattice-matched to InP grown by MBE," *Electron. Lett.*, vol. 22, no. 4, p. 191, 1986.

[79] P. Dongmo, Y. Zhong, P. Attia, C. Bomberger, R. Cheaito, J. F. Ihlefeld, P. E. Hopkins, and J. Zide, "Enhanced room temperature electronic and thermoelectric properties of the dilute bismuthide InGaBiAs," *J. Appl. Phys.*, vol. 112, no. 9, p. 093710, 2012.

[80] H. Q. Zheng, K. Radahakrishnan, S. F. Yoon, and G. I. Ng, "Electrical and optical properties of Si-doped InP grown by solid source molecular beam epitaxy using a valved phosphorus cracker cell," *J. Appl. Phys.*, vol. 87, no. 11, p. 7988, 2000.

[81] K. Ellmer and R. Mientus, “Carrier transport in polycrystalline ITO and ZnO:Al II: The influence of grain barriers and boundaries,” *Thin Solid Films*, vol. 516, no. 17, pp. 5829–5835, Jul. 2008.

[82] Y. Zhong, P. B. Dongmo, L. Gong, S. Law, B. Chase, D. Wasserman, and J. M. O. Zide, “Degenerately doped InGaBiAs:Si as a highly conductive and transparent contact material in the infrared range,” *Opt. Mater. Express*, vol. 3, no. 8, p. 1197, Jul. 2013.

[83] E. Burstein, “Anomalous optical absorption limit in InSb,” *Phys. Rev.*, vol. 93, no. 3, pp. 2–3, 1954.

[84] T. S. Moss, “The Interpretation of the Properties of Indium Antimonide,” *Proc. Phys. Soc.*, vol. 67, no. 775, 1954.

[85] A. Porch, “Electromagnetic absorption in transparent conducting films,” *J. Appl. Phys.*, vol. 95, no. 9, p. 4734, 2004.

[86] G. Haacke, “New figure of merit for transparent conductors,” *J. Appl. Phys.*, vol. 47, no. 9, p. 4086, 1976.

[87] E. Yablonovitch and G. D. Cody, “Intensity enhancement in textured optical sheets for solar cells,” *IEEE Trans. Electron Devices*, vol. 29, no. 2, pp. 300–305, Feb. 1982.

[88] H. W. Deckman, C. B. Roxlo, and E. Yablonovitch, “Maximum statistical increase of optical absorption in textured semiconductor films.,” *Opt. Lett.*, vol. 8, no. 9, pp. 491–3, Sep. 1983.

[89] H. A. Atwater and A. Polman, “Plasmonics for improved photovoltaic devices.,” *Nat. Mater.*, vol. 9, no. 3, pp. 205–13, Mar. 2010.

[90] S. Pillai, K. R. Catchpole, T. Trupke, and M. A. Green, “Surface plasmon enhanced silicon solar cells,” *J. Appl. Phys.*, vol. 101, no. 9, p. 093105, 2007.

[91] V. E. Ferry, L. a Sweatlock, D. Pacifici, and H. A. Atwater, “Plasmonic nanostructure design for efficient light coupling into solar cells.,” *Nano Lett.*, vol. 8, no. 12, pp. 4391–7, Dec. 2008.

[92] R. A. Pala, J. White, E. Barnard, J. Liu, and M. L. Brongersma, “Design of Plasmonic Thin-Film Solar Cells with Broadband Absorption Enhancements,” *Adv. Mater.*, vol. 21, no. 34, pp. 3504–3509, Sep. 2009.

[93] W. Shockley and H. J. Queisser, "Detailed Balance Limit of Efficiency of p-n Junction Solar Cells," *J. Appl. Phys.*, vol. 32, no. 3, p. 510, 1961.

[94] J. F. Geisz, D. J. Friedman, J. S. Ward, A. Duda, W. J. Olavarria, T. E. Moriarty, J. T. Kiehl, M. J. Romero, A. G. Norman, and K. M. Jones, "40.8% Efficient Inverted Triple-Junction Solar Cell With Two Independently Metamorphic Junctions," *Appl. Phys. Lett.*, vol. 93, no. 12, p. 123505, 2008.

[95] W. Guter, J. Schöne, S. P. Philipps, M. Steiner, G. Siefer, A. Wekkeli, E. Welser, E. Oliva, A. W. Bett, and F. Dimroth, "Current-matched triple-junction solar cell reaching 41.1% conversion efficiency under concentrated sunlight," *Appl. Phys. Lett.*, vol. 94, no. 22, p. 223504, 2009.

[96] T. Trupke, M. A. Green, and P. Würfel, "Improving solar cell efficiencies by down-conversion of high-energy photons," *J. Appl. Phys.*, vol. 92, no. 3, p. 1668, 2002.

[97] R. Schaller and V. Klimov, "High Efficiency Carrier Multiplication in PbSe Nanocrystals: Implications for Solar Energy Conversion," *Phys. Rev. Lett.*, vol. 92, no. 18, p. 186601, May 2004.

[98] J. L. Miller, "Multiple exciton generation enhances a working solar cell," *Phys. Today*, vol. 65, no. 2, p. 17, 2012.

[99] A. Luque, A. Martí, and C. Stanley, "Understanding intermediate-band solar cells," *Nat. Photonics*, vol. 6, no. 3, pp. 146–152, Feb. 2012.

[100] A. Luque and A. Martí, "The intermediate band solar cell: progress toward the realization of an attractive concept.," *Adv. Mater.*, vol. 22, no. 2, pp. 160–74, Jan. 2010.

[101] A. Luque, A. Martí, C. Stanley, N. López, L. Cuadra, D. Zhou, J. L. Pearson, and A. McKee, "General equivalent circuit for intermediate band devices: Potentials, currents and electroluminescence," *J. Appl. Phys.*, vol. 96, no. 1, p. 903, 2004.

[102] N. López, L. A. Reichertz, K. M. Yu, K. Campman, and W. Walukiewicz, "Engineering the Electronic Band Structure for Multiband Solar Cells," *Phys. Rev. Lett.*, vol. 106, no. 2, p. 028701, Jan. 2011.

[103] M. J. Keevers and M. A. Green, "Efficiency improvements of silicon solar cells by the impurity photovoltaic effect," *J. Appl. Phys.*, vol. 75, no. 8, p. 4022, 1994.

[104] W. M. Reid, T. Driscoll, and M. F. Doty, "Forming delocalized intermediate states with realistic quantum dots," *J. Appl. Phys.*, vol. 111, no. 5, p. 056102, 2012.

[105] A. C. Atre and J. A. Dionne, "Realistic upconverter-enhanced solar cells with non-ideal absorption and recombination efficiencies," *J. Appl. Phys.*, vol. 110, no. 3, p. 034505, 2011.

[106] J. Boyer, L. A. Cuccia, and J. A. Capobianco, "Synthesis of Colloidal Upconverting Monodisperse Nanocrystals," *Nano Lett.*, vol. 7, no. 3, pp. 847–852, 2007.

[107] S. Fischer, J. C. Goldschmidt, P. Löper, G. H. Bauer, R. Brüggemann, K. Krämer, D. Biner, M. Hermle, and S. W. Glunz, "Enhancement of silicon solar cell efficiency by upconversion: Optical and electrical characterization," *J. Appl. Phys.*, vol. 108, no. 4, p. 044912, 2010.

[108] S. Heer, K. Kompe, H. U. Gudel, and M. Haase, "Highly Efficient Multicolour Upconversion Emission in Transparent Colloids of Lanthanide-Doped $NaYF_4$ Nanocrystals," *Adv. Mater.*, vol. 16, no. 23–24, 2004.

[109] Z. Li, Y. Zhang, and S. Jiang, "Multicolor Core/Shell-Structured Upconversion Fluorescent Nanoparticles," *Adv. Mater.*, vol. 20, no. 24, pp. 4765–4769, Dec. 2008.

[110] D. M. Tex and I. Kamiya, "Upconversion of infrared photons to visible luminescence using InAs-based quantum structures," *Phys. Rev. B*, vol. 83, no. 8, p. 081309, Feb. 2011.

[111] X. Wang, W. Yu, J. Zhang, J. Aldana, X. Peng, and M. Xiao, "Photoluminescence upconversion in colloidal CdTe quantum dots," *Phys. Rev. B*, vol. 68, no. 12, p. 125318, Sep. 2003.

[112] C. M. Jaworski, B. Wiendlocha, V. Jovovic, and J. P. Heremans, "Combining alloy scattering of phonons and resonant electronic levels to reach a high thermoelectric figure of merit in PbTeSe and PbTeS alloys," *Energy Environ. Sci.*, vol. 4, no. 10, p. 4155, 2011.

[113] Y. Y. Cheng, T. Khoury, R. G. C. R. Clady, M. J. Y. Tayebjee, N. J. Ekins-Daukes, M. J. Crossley, and T. W. Schmidt, "On the efficiency limit of triplet-triplet annihilation for photochemical upconversion.," *Phys. Chem. Chem. Phys.*, vol. 12, no. 1, pp. 66–71, Jan. 2010.

[114] T. N. Singh-Rachford and F. N. Castellano, "Photon upconversion based on sensitized triplet–triplet annihilation," *Coord. Chem. Rev.*, vol. 254, no. 21–22, pp. 2560–2573, Nov. 2010.

[115] A. Shalav, B. S. Richards, and M. A. Green, "Luminescent layers for enhanced silicon solar cell performance: Up-conversion," *Sol. Energy Mater. Sol. Cells*, vol. 91, no. 9, pp. 829–842, May 2007.

[116] J. F. Suyver, A. Aebischer, D. Biner, P. Gerner, J. Grimm, S. Heer, K. W. Krämer, C. Reinhard, and H. U. Güdel, "Novel materials doped with trivalent lanthanides and transition metal ions showing near-infrared to visible photon upconversion," *Opt. Mater. (Amst).*, vol. 27, no. 6, pp. 1111–1130, Mar. 2005.

[117] Y. Zhong, D. Sellers, M. F. Doty, and J. M. O. Zide, "Novel Nanostructures for Efficient Photon Upconversion and High-efficiency Photovoltaics," *Submitt. to Adv. Mater.*, 2013.

[118] "http://sjbyrnes.com/sq.pdf,".

[119] T. Trupke, M. A. Green, and P. Würfel, "Improving solar cell efficiencies by up-conversion of sub-band-gap light," *J. Appl. Phys.*, vol. 92, no. 7, p. 4117, 2002.

[120] R. Heitz, H. Born, F. Guffarth, O. Stier, A. Schliwa, A. Hoffmann, and D. Bimberg, "Existence of a phonon bottleneck for excitons in quantum dots," *Phys. Rev. B*, vol. 64, no. 24, p. 241305, Nov. 2001.

[121] D. B. Malins, A. Gomez-Iglesias, S. J. White, W. Sibbett, A. Miller, and E. U. Rafailov, "Ultrafast electroabsorption dynamics in an InAs quantum dot saturable absorber at 1.3 μm," *Appl. Phys. Lett.*, vol. 89, no. 17, 2006.

[122] T. N. Leite and H. P. de Oliveira, "Tunneling Processes in a Triangular Multibarrier Semiconductor Heterostructure," *IEEE Trans. Electron Devices*, vol. 58, no. 3, pp. 716–719, Mar. 2011.

[123] T. J. C. Hosea, presentation at "4th international workshop on bismuth-containing semiconductors."

[124] R. Lewis, presentation at "2nd international bismuth-containing materials workshop."

[125] M. W. Moseley, "M. Moseley PhD Dissertation," 2013.

[126] W. Shan, W. Walukiewicz, and J. W. A. III, "Band Anticrossing in GaInNAs Alloys," *Phys. Rev. Lett.*, 1999.

[127] W. Shan, W. Walukiewicz, J. W. Ager, E. E. Haller, J. F. Geisz, D. J. Friedman, J. M. Olson, and S. R. Kurtz, "Effect of nitrogen on the band structure of GaInNAs alloys," *J. Appl. Phys.*, vol. 86, no. 4, 1999.

[128] J. R. Dixon, and R. F. Bis, "Band inversion and the electrical properties of $Pb_xSn_{1-x}Te$," vol. 1075, 1966.

[129] I. P. Marko, Z. Batool, K. Hild, S. R. Jin, N. Hossain, T. J. C. Hosea, J. P. Petropoulos, Y. Zhong, P. B. Dongmo, J. M. O. Zide, and S. J. Sweeney, "Temperature and Bi-concentration dependence of the bandgap and spin-orbit splitting in InGaBiAs/InP semiconductors for mid-infrared applications," *Appl. Phys. Lett.*, vol. 101, no. 22, p. 221108, 2012.

Appendix A

PERMISSION LETTER FROM AIP PUBLISHING LLC

Dear Dr. Zhong:

Thank you for requesting permission to reproduce material from AIP Publishing LLC publications.

Material to be reproduced:

R. N. Kini, L. Bhusal, A. J. Ptak, R. France, and A. Mascarenhas, "Electron Hall mobility in GaAsBi," *J. Appl. Phys.*, vol. 106, no. 4, 2009.

X. Lu, D. A. Beaton, R. B. Lewis, T. Tiedje, and M. B. Whitwick, "Effect of molecular beam epitaxy growth conditions on the Bi content of $GaAs_{1-x}Bi_x$," *Appl. Phys. Lett.*, vol. 92, no. 19, 2008.

Y. Zhong, P. B. Dongmo, J. P. Petropoulos, and J. M. O. Zide, "Effects of molecular beam epitaxy growth conditions on composition and optical properties of $In_xGa_{1-x}Bi_yAs_{1-y}$," *Appl. Phys. Lett.*, vol. 100, no. 11, 2012.

J. P. Petropoulos, Y. Zhong, and J. M. O. Zide, "Optical and electrical characterization of InGaBiAs for use as a mid-infrared optoelectronic material," *Appl. Phys. Lett.*, vol.

99, no. 3, 2011.

R. Kudrawiec, J. Kopaczek, J. Misiewicz, J. P. Petropoulos, Y. Zhong, and J. M. O. Zide, "Contactless electroreflectance study of E_0 and $E_0 + \Delta_{SO}$ transitions in $In_{0.53}Ga_{0.47}Bi_xAs1-x$ alloys," *Appl. Phys. Lett.*, vol. 99, no. 25, 2011.

P. Dongmo, Y. Zhong, P. Attia, C. Bomberger, R. Cheaito, J. F. Ihlefeld, P. E. Hopkins, and J. Zide, "Enhanced room temperature electronic and thermoelectric properties of the dilute bismuthide InGaBiAs," *J. Appl. Phys.*, vol. 112, no. 9, 2012.

For use in the following manner:

Reproduced in your dissertation.

Permission is granted subject to these conditions:

1. AIP Publishing LLC grants you non-exclusive world rights in all languages and media. This permission extends to all subsequent and future editions of the new work.

2. The following copyright notice must appear with the material (please fill in the information indicated by capital letters):

"Reproduced with permission from [FULL CITATION]. Copyright [PUBLICATION YEAR], AIP Publishing LLC."

When reusing a full article, the copyright notice must be printed on the first page of the reprinted article or book chapter. When reusing figures, photographs, covers, or tables, the notice may appear in the caption, in a footnote, or in the reference list.

In cases where the new publication is licensed under a Creative Commons license, the full copyright notice as stated above must appear with the reproduced material.

3. If the material is published in electronic format, we ask that a link be created pointing back to the abstract of the article on the journal website. This can be accomplished through the use of the article's DOI.

4. This permission does not apply to any materials credited to sources other than the copyright holder.

5. If you have not already done so, please attempt to obtain permission from at least one of the authors. The authors' contact information can usually be obtained from the article.

Please let us know if you have any questions.

Sincerely,

Susann Brailey

Manager, Rights and Permissions

AIP Publishing LLC

Suite 1NO1

2 Huntington Quadrangle

Melville, NY 11747-4502

Phone: 1-516-576-2268

Fax: 1-516-576-2450

Email: sbrailey@aip.org

Appendix B

PERMISSION LETTER FROM OSA

Dear Dr. Zhong,

Thank you for contacting The Optical Society.

Since you are the author of the paper from which you wish to republish material, OSA considers your requested use of its copyrighted materials to be permissible within the author rights granted in the Copyright Transfer Agreement submitted by the requester on acceptance for publication of his/her manuscript. It is requested that a complete citation of the original material be included in any publication. This permission assumes that the material was not reproduced from another source when published in the original publication.

Please let me know if you have any questions.

Best,
Hannah Bembia
December 20, 2013
Authorized Agent, The Optical Society